UNIVERSITÄT DUISBURG ESSEN

Open-Minded

Mono- and bimetallic faceted noble metal nanoparticles:

Synthesis and characterization

DISSERTATION

Zur Erlangung des akademischen Grades eines

Doktors der Naturwissenschaften

- Dr. rer. nat. -

vorgelegt von

M.Sc. Aikaterini Karatzia

geboren in Athen, Griechenland

Fakultät für Chemie der Universität Duisburg-Essen

Anorganische Chemie

2023

DOI: 10.17185/duepublico/81247
URN: urn:nbn:de:hbz:465-20231130-075911-5

As you set out for Ithaka
hope the voyage is a long one,
full of adventure, full of discovery.
Laistrygonians and Cyclops,
angry Poseidon - don't be afraid of them:
you'll never find things like that on your way
as long as you keep your thoughts raised high,
as long as a rare excitement
stirs your spirit and your body.

Ithaka, K. Kavafis

Σα βγεις στον πηγαιμό για την Ιθάκη,
να εύχεσαι νάναι μακρύς ο δρόμος,
γεμάτος περιπέτειες, γεμάτος γνώσεις.
Τους Λαιστρυγόνας και τους Κύκλωπας,
τον θυμωμένο Ποσειδώνα μη φοβάσαι,
τέτοια στον δρόμο σου ποτέ σου δεν θα βρεις,
αν μέν' η σκέψις σου υψηλή, αν εκλεκτή
συγκίνησις το πνεύμα και το σώμα σου αγγίζει.

Ιθάκη, Κ. Καβάφης

Die vorliegende Arbeit wurde im Zeitraum von November 2020 bis August 2023 im Arbeitskreis von Prof. Dr. Matthias Epple am Institut der Anorganischen Chemie der Universität Duisburg-Essen angefertigt.

Gutachter:	Prof. Dr. Matthias Epple
	Prof. Dr. Claudia Weidenthaler
Vorsitzender:	Prof. Dr. Sven Heiles
Tag der Disputation:	10.11.2023

TABLE OF CONTENTS

1. INTRODUCTION

Nanomaterials, with their unique properties arising from the nanoscale dimensions, have revolutionized numerous scientific and technological fields in the last few decades. These materials exhibit distinct physical, chemical, and biological behaviors compared to their bulk counterparts, making them highly desirable for a wide range of applications. Among the most intriguing nanomaterials are metal nanoparticles, which possess exceptional attributes owing to their small size and large surface area.[1-3] By precisely engineering materials at the atomic and molecular levels, researchers have been able to tailor their properties to meet specific needs.

Metal nanoparticles, particularly those composed of noble metals such as gold, silver, and platinum, have gathered significant attention due to their fascinating properties and promising applications. Noble metal nanoparticles exhibit remarkable optical phenomena, including localized surface plasmon resonance (LSPR), which arises from the collective oscillation of conduction electrons at the nanoparticle surface. This exceptional optical behavior has paved the way for numerous sensing, imaging, and medical diagnostics applications.[4-9] Silver nanoparticles have exhibited outstanding antibacterial properties due to their unique interaction with bacterial cell membranes and the oxidative release of silver anions.[10, 11] The antibacterial performance of their structures can be improved through bimetallic formation with noble metals like gold, palladium, and platinum, which accelerate ion release kinetics.[11, 12]

Regarding their thermal properties, they often have lower melting points, and altered thermal expansion behavior.[13-17] Their specific heat capacity may be lower, and their thermal conductivity can be either enhanced or reduced depending on size and shape.[14, 18] Nanoparticles are known for their efficient heat dissipation capabilities[19-21] and can possess unique photothermal properties.[22, 23] These thermal characteristics affect diverse applications in nanotechnology, electronics, and biomedical engineering fields.

In addition to their optical and thermal properties, noble metal nanoparticles possess exceptional catalytic activity, making them valuable in homogeneous and heterogeneous catalysis, as they can be recycled and reused after proper treatment.[24-27] Typical metallic catalysts are the platinum metals, such as platinum, palladium,

iridium, ruthenium, and rhodium. Their high surface-to-volume ratio allows for efficient adsorption and interaction with reactants, facilitating chemical reactions with enhanced rates and selectivity. For instance, gold nanoparticles have demonstrated outstanding catalytic performance in various reactions, such as carbon monoxide oxidation and selective hydrogenation.[25, 28-30] Except for the automobile pollutants, palladium nanoparticles catalyze several reactions such as Suzuki, Heck, and Stille coupling.[31-34] Precise control over the size and shape of noble metal nanoparticles is also crucial for tailoring their properties and optimizing their catalytic performance.[35, 36] Nanoparticles with well-defined structures offer higher selectivity.[37] Faceted nanoparticles, such as cubes, cuboids, wires, octahedra, and tetrahedra, have gathered significant interest due to their distinct properties. The presence of different facets on a single nanoparticle introduces anisotropic behavior, altering their electronic structure and catalytic activity. The surfaces of those nanostructures are enclosed by a mix of low-index facets such as (100), (110), and (111) in different ratios.[38] For instance, silver nanocubes enclosed by (100) facets showed higher catalytic activity in the styrene oxidation reaction than truncated triangular silver nanoplates and quasi-spherical silver nanoparticles enclosed by (111) facets.[39] Furthermore, platinum-catalyzed hydrogenation of benzene with single-crystal nanocubes gave only one product, whereas the same reaction catalyzed by cuboctahedral platinum nanoparticles with also (100) facets gave two.[40] On the other hand, the high-index facets provide a higher density of active sites compared to the low-index facets, resulting in enhanced catalytic performance.[41-43] However, the synthesis of such metal nanostructures, such as gold star- or snowflake-shaped,[44, 45] and noble metal nanoflowers[46], in large amounts and high yields remains challenging due to their high surface energy. The distinct catalytic properties of noble metal nanoparticles have led to their applications in environmental remediation, energy conversion, and pharmaceutical industries.[47, 48]

In addition to controlling the size and shape, bimetallic nanoparticles have emerged as a promising alternative for tailoring the properties of noble metal nanoparticles. The controlled combination of two different metal species allows for synergistic effects, where the unique properties of each metal can be combined to achieve enhanced catalytic activity, improved stability, and novel biomedical applications.[49-52] For instance, platinum-based bimetallic nanoparticles have demonstrated superior catalytic activity in the oxygen reduction reaction (ORR) compared to pure platinum

nanoparticles.[53, 54] However, the need for bimetallic nanoparticles shows also economic aspects. The chemical industry suffers from high synthetic costs, and the rarity of noble metals makes them expensive.[41] Therefore, alternative synthetic methods should be developed to reduce costs, such as using core-shell structures with cheaper metals in the core and noble metals on the surface. These innovative approaches hold the potential to make noble metal nanoparticles more affordable and accessible for various applications, addressing the urgent need for cost-effective substitutes in the chemical industry and beyond.

The studies presented in this work were conducted in the research group of Prof. Dr. Matthias Epple at the Institute of Inorganic Chemistry, University of Duisburg-Essen, in Essen. The primary objective of this research is to synthesize and characterize faceted mono- and bimetallic nanoparticles of noble metals. The focus lies on achieving well-defined structures through various synthetic approaches and subsequently characterizing these nanoparticles using spectroscopic, colloidal, microscopical, and diffraction techniques. The first part of the research concentrates on synthesizing and thoroughly characterizing monometallic silver and palladium nanoparticles with well-defined structures, such as wires and cubes. The second part of the study focuses on establishing and optimizing reproducible wet-chemical core-shell syntheses of two noble metals. The comprehensive characterization of both monometallic and bimetallic structures includes spectroscopic techniques such as ultraviolet and visible spectroscopy (UV-Vis) and atomic absorption spectroscopy (AAS). Colloid methods such as dynamic light scattering (DLS) and differential centrifugal sedimentation (DSC) are employed further for characterization. Additionally, the composition, morphology, and structure of the nanoparticles are extensively investigated using scanning electron microscopy (SEM), scanning transmission electron microscopy (STEM), transmission electron microscopy (TEM), energy-dispersive X-ray spectroscopy (EDS), and powder X-ray diffraction (PXRD). The third and final part of the research focuses on monometallic silver and bimetallic core-shell nanocubes. The thermal behavior of these two systems is extensively examined *in-situ* using techniques such as SEM, TEM, and PXRD.

2. THEORETICAL BACKGROUND

2.1 Colloids and nanoparticles

The term *colloid* was first introduced by the Scottish chemist Thomas Graham in 1961. His research on the behavior of various substances, such as starch and glue in solutions, revealed that they exhibit properties different from those of typical solutions or suspensions. The word *colloid* derives from the Greek word *kolla (κόλλα)*, which means *glue* or *sticky substance*. A colloidal system, according to IUPAC, "is a state of subdivision, implying that the molecules or polymolecular particles dispersed in a medium have a dimension between 1 nm and 1 μm, at least in one direction, or that in a system discontinuities are found at distances of that".[55] In other words, a colloidal system or dispersion, is a mixture of two substances, one of which, the dispersed phase, is evenly dispersed within another substance, the continuous phase or dispersing medium. The size of the particles in the colloidal size range is usually between 1 nm and 1 μm.[56] Both the dispersed substance and the medium can be in the solid, liquid, or gas phase. Examples of potential colloidal systems are presented in Table 1.

Table 1. Examples of colloidal systems.

Dispersed phase	Dispersing medium	Common name	Examples
liquid	gas	liquid aerosol	spray
liquid	solid	solid emulsion	opal
liquid	liquid	emulsion	milk
gas	liquid	foam	beer foam
gas	solid	solid foam	styrofoam
solid	solid	solid sol	colored gems
solid	liquid	sol	paint
solid	gas	solid aerosol	dust

During the past few decades, there has been considerable attention on colloidal systems in which particles in the nanoscale dimensions are dispersed in liquid media. The prefix *nano* can be traced back to the Greek word *nanos (νάνος)* which means dwarf-like.

According to the International Organization for Standardization (ISO, 2008), a nanoparticle is a nano-object with all its three Cartesian dimensions under 100 nm.[57] Similarly, two- and- three-dimensional nano-objects (i.e., nanodiscs and nanofibers, respectively) were also defined. However, in 2011, the European Union Commission proposed a more technical and broader definition.[58] According to the latter, a nano-object can be classified as a nanoparticle if at least one of its dimensions falls within the 1 to 100 nm range, even if its other dimensions fall outside this range.[59-61]

2.2 Synthesis of nanoparticles

There are two main approaches to synthesizing nanoparticles: top-down and the bottom-up (Fig.1).

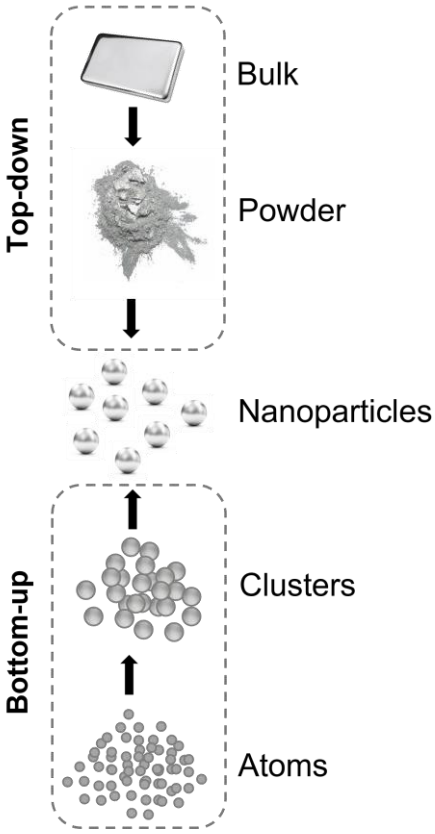

Figure 1. Schematic depiction of bottom-up and top-down syntheses of nanoparticles.

The top-down method involves breaking down bulk materials into nanoparticles using physical or chemical processes. Methods like milling, grinding,[62] and laser ablation[63] are typical physical methods. Yet, chemical processes can also break down bulk materials into smaller particles. An acid or base can dissolve the bulk material into particles. Once the nanoparticles are created, additional chemical reactions can be used to modify their surface properties. On the other hand, the bottom-up method could be considered as a construction method that involves assembling smaller building blocks such as molecules or atoms. Standard bottom-up methods are chemical reduction, sol-gel, hydrothermal, and electrochemical synthesis.[64-66]

Overall, both methods are widely used, but they also have their limitations. The top-down approach is often more straightforward for generating nanoparticles and can lead to high product yields. However, this method has drawbacks, especially when particles with well-defined shapes, sizes, and chemical compositions are required, as the nanoparticles produced have varying sizes and shapes and exhibit broad size distribution. In contrast, bottom-up approaches can be more complicated but offer more control during the synthesis of nanoparticles and narrow size distribution. Nonetheless, they can be more time-consuming, require careful control of the reaction conditions, and provide comparably small yields. As a result, scaling up for larger nanoparticle production poses a significant challenge.[66-68]

The bottom-up synthesis of the nanoparticles is a crystallization process. The mechanism of nanoparticle growth was first proposed by Viktor LaMer in 1950. LaMer's model distinguishes between three phases, as shown in (Fig. 2). During the first phase, ions are reduced to form atoms (I). As the reduction continues, the concentration of the formed atoms increases. Once the concentration exceeds a critical value (C_{max}), the nucleation of the atoms begins (II). At this stage, the formed nuclei are growing rapidly to form small clusters while the concentration decreases until it reaches a minimum value (C_{min}). In the third and final phase (III), no new nuclei are formed, and the nanocrystals continue to grow by absorbing the remaining atoms in the solution until a saturation concentration, c_s, is reached.[69, 70]

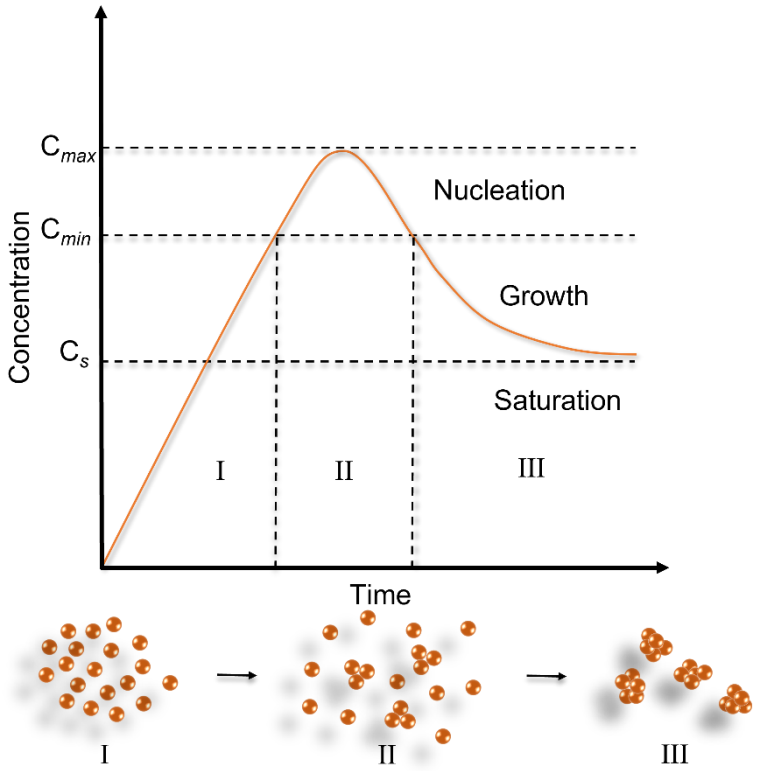

Figure 2. Schematic representation of the concentration of LaMer's model for nanoparticle growth and crystallization.

Several parameters can modify the crystallization process, impacting the particles' size and shape. To obtain, for example, a desired shape, the structure of the nuclei must be accordingly controlled either thermodynamically or kinetically. Thermodynamically controlled reactions lead to the production of the most energetically stable products. Kinetic nucleation control occurs through the precursor compound's decomposition or reduction rate. This can be achieved, for example, by choosing a suitable reducing agent.[71] Strong reducing agents, like sodium borohydride ($NaBH_4$), enhance the velocity of the nucleation and lead to a higher number of nuclei than weaker reducing agents, such as ascorbic acid, whose addition results in a lower number of nuclei. Another parameter for the kinetic control of the nucleation is the concentration of the precursor[72] used and several combinations of different parameters. Depending on the combination the behavior of the system changes, which can also have an impact on the dispersity of the system.

Due to their high surface-to-volume ratio, the produced nanoparticles are thermodynamically unstable. Consequently, colloidal systems tend to minimize their

surface by forming larger structures (agglomerates). The mathematical equation that describes the relation between free enthalpy and surface tension of a colloidal system is the following:

$$dG = \gamma dA_G \quad (1)$$

G free enthalpy,

γ surface tension,

A_G particle surface

According to equation (1), free enthalpy (*G*) increases or decreases proportionally to the created particle surface (A_G). Over time it is common for particles to build up and grow in size over time. When different sizes of particles coexist in a colloidal solution, the smaller particles may dissolve in favor of the larger ones through a process called Ostwald ripening, resulting in larger structures.[73] Stabilizing methods are necessary to prevent Ostwald ripening and maintain the particles' desired shape and size.

2.3 Stabilization of nanoparticles

Colloids are thermodynamically unstable, and every system tends to reach a more stable state.[74] This process is called aging in dispersions and can be described as a natural, spontaneous, and slow process. The stability of colloidal dispersion can be described with the DLVO theory.[75] This theory was named after its creators, Derjaguin, Landau, Verwey, and Overbeek. Stability derives from the interaction between attractive and repulsive forces. In this case, the van der Waals forces are the attractive and electrostatic forces the repulsive ones. If the attractive forces between the particles overcome the repulsive forces, the particles will come closer and form aggregates. On the other hand, if the repulsive forces are greater than the attractive ones, the particles will remain dispersed, and the system is stable (Fig. 3).[76]

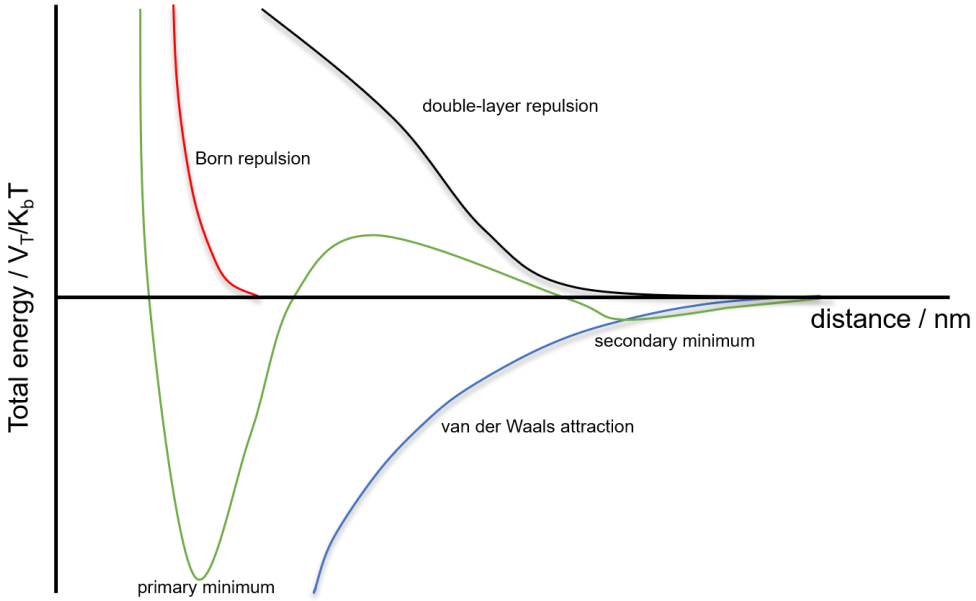

Figure 3. Interaction forces between particles in colloidal systems.

Steric stabilization (Fig. 4) involves functionalization of the surface of the particles with suitable uncharged ligands-polymers, such as poly (N-vinylpyrrolidone) (PVP) and polyvinyl alcohol (PVA) (Fig. 6).

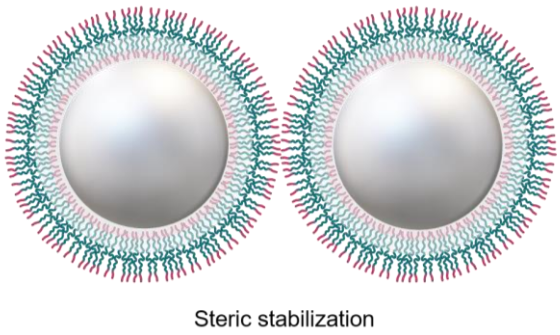

Figure 4. Schematic drawing of steric stabilization of nanoparticles.

Electrostatic stabilization can be achieved by adding charged molecules such as trisodium citrate (Fig. 6) or sodium ascorbate to balance the attraction with the repulsion forces between the charged particles. Counterions are usually present in the dispersion medium. They can be adsorbed on the particles' surface, forming an almost immobile layer (Stern layer) which is, in turn, surrounded by a mobile diffuse layer of ions. As a result, they form an electric double layer (Fig.5).

The charge of the particles can be quantified using the zeta potential (ζ-potential) and thus provide information about the stability of the colloid. A colloidal system is deemed stable when its ζ-potential values are either over +30 mV or below -30 mV.[77]

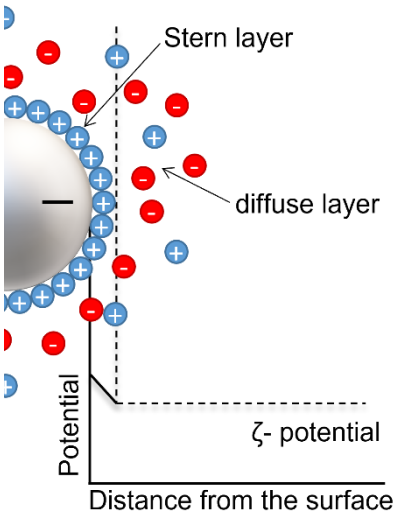

Figure 5. Schematic representation of an electrostatically stabilized nanoparticle and the corresponding electric double layer.

The third method is a combination of the two previous, which can be realized by the addition of charged polymers such as sodium polystyrene sulfonate (PSS) or charged peptides such as glutathione (GSH) (Fig. 6).[78]

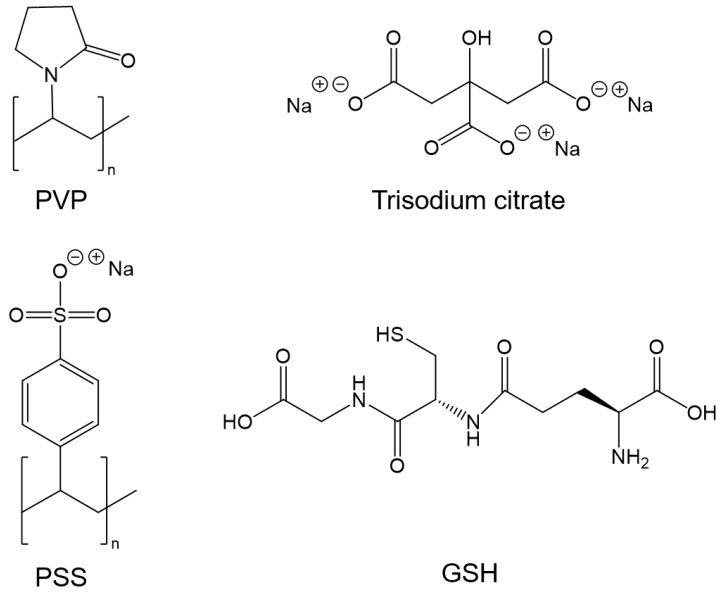

Figure 6. Examples of ligands used for steric (PVP), electrostatic (trisodium citrate), and electrosteric (PSS, GSH) stabilization of nanoparticles.

2.4 Metallic nanoparticles

2.4.1 Shape-controlled synthesis of metallic nanoparticles

Besides chemical composition, size, and surface functionalization, their shape is another important factor that can influence nanoparticles' physical, chemical, and biological properties. For example, it was shown that specific shapes could enhance catalytic activities[79, 80] or exhibit improved cellular uptake compared to other shapes.[81] However, synthesizing nanoparticles with specific shapes can be extremely challenging, as many parameter combinations should be carefully tuned. Even slight variations during the synthesis can result in significant changes, making it difficult to achieve reproducible results. Various synthetic strategies have been developed by many scientific groups to generate different shapes and sizes of noble metal nanoparticles, such as nanocubes, nanowires, nanoplates. Xia and coworkers could be considered pioneers in this field, with over 60 publications on the shape-controlled synthesis of noble metal nanoparticles.[82-86]

To overcome such challenges, researchers have proposed various synthetic methods and routes. Among these, the polyol method is popular for generating form-controlled metallic nanoparticles. In this method, the polyols act both as solvents and reductants. Different polyols, such as ethylene glycol (EG) and propylene glycol (PG), have obtained nanoparticles with different shapes and sizes. Their high boiling point, in combination with their reduction potentials, are the main factors on which the selection of the suitable polyol for each synthetic route depends.[87, 88] Another approach is the template-assisted method, wherein preformed nanoparticles with the desired size and shape are employed, as sacrificial templates. These templates act as scaffolds and play a crucial role in determining the final morphology of nanoparticles.[89, 90] Additionally, seed-mediated growth, a widely known approach, uses pre-synthesized particles as seeds to initiate the growth of larger nanoparticles with a desired shape.[91]

Besides the available synthetic methods, choosing a suitable capping agent, such as PVP or CTAB, plays an essential role in forming nanoparticles with specific shapes and sizes. These polymers not only prevent agglomeration of the colloidal system but also can influence the crystallization process.[92]

Crystals are three-dimensional structures whose atoms are arranged in a highly ordered manner. They are characterized by a repetitive and periodic arrangement of

their smallest unit, the unit cell. When aiming for shape-control synthesis, thermodynamic and kinetic factors must be carefully controlled during the crystallization process.[93, 94] Generally, as previously mentioned, a colloidal system constantly strives to reduce its free surface energy to become thermodynamically stable. The evaluation of the facet stability at the nanoscale still raises arguments, contrary to the bulk crystals that can be measured. However, the relative stability of the facets could be assessed based on the bonding interactions and the surface packing efficiency. The facet stability relies on the average number and strength of bonds formed between neighboring atoms. In the case of a face-centered cubic (fcc) metal nanocrystal, such as gold or silver, the (111) facets are typically considered the most stable, followed by (100) and (110) facets. Equation 2 demonstrates how the free surface energy per area (γ) of the fcc lattice increases.[95, 96]

$$\gamma_{111} < \gamma_{100} < \gamma_{110} \quad (2)$$

Indeed, kinetic control is also required in synthetic routes that generate nanoparticles with specific shapes. The presence of ligands attached to the surface of metal nanocrystals plays a crucial role in their kinetic growth. Extensive studies have focused on various ligands that selectively block specific facets, influencing the shape of the nanoparticles.[69, 97-101] These ligands play a crucial role in directing the growth of the nanocrystals, allowing the formation of desired shapes by controlling the rates of crystal growth on different facets. The development and understanding of ligand-assisted kinetic control have significantly upgraded the field of shape-controlled synthesis of nanoparticles.

2.4.2 Bimetallic nanoparticles

The synthesis of bimetallic nanoparticles can be achieved through various methods, such as chemical reduction, co-reduction, seed-and-growth, galvanic replacement, and thermal decomposition. These methods allow control over the nanoparticles' size, shape, composition, and structure, which can, in turn, influence their properties. The specific properties of bimetallic nanoparticles depend on factors such as the choice of metals, their relative ratio, and the arrangement of the two metals within the nanoparticle structure.

Bimetallic nanoparticles have diverse structures ranging from mixed alloys, alloys with an intermetallic compound, Janus, core-shell, multi-core shell, to multiple small cores coated by single-shell material. (Fig. 7)

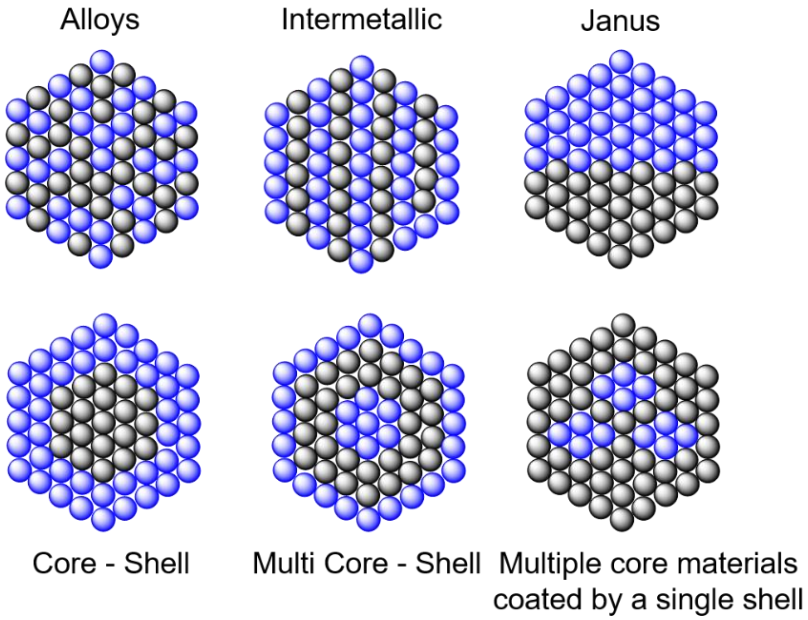

Figure 7. Types of possible bimetallic structures.

Alloyed nanoparticles are usually produced through simultaneous reduction (co-reduction) of two metal precursors.[52, 102] When there is a significant difference in atomic size between the two components, it can lead to the creation of intermetallic alloyed structures. Conversely, mixed alloys can be produced when the nuclear sizes are similar.[103] Various synthetic strategies have already been developed to generate Janus nanoparticles, which exhibit distinct regions of different materials. These strategies can be broadly categorized into three large groups: masking, self-assembly,

and phase separation technique. Masking involves the selective coating of specific regions of the nanoparticles, followed by the deposition of another material on the exposed areas. Self-assembly takes advantage of the intrinsic properties of the nanoparticles to form Janus structures on their own, and phase separation techniques rely on the preferential affinity of different components to separate and create distinct regions within the particles. [104, 105] In the case of core-shell particles, a common synthesis method is the seed-and-growth approach, which involves a two-step process. Monometallic nanoparticles, called “seeds,” are synthesized in the first step. These seeds serve as a template for the second step, where another precursor is reduced and crystalizes on the surface of the seed, forming a shell around it and resulting in core-shell structures.[50, 52, 106, 107] Creating core-shell bimetallic nanoparticles can be a complex task due to the need for precise control of various parameters, including pH, temperature, precursor concentration, and rate of precursor addition. These factors must be carefully controlled to produce the desired bimetallic systems successfully.

The biggest challenge for the generation of core-shell particles is controlling the galvanic replacement reaction that usually takes place between two metals due to their different standard potential.

2.4.3 Galvanic replacement

A galvanic replacement reaction, also known as galvanic displacement or redox replacement reaction, refers to a chemical reaction in which one metal displaces another from its compound. This reaction occurs due to the difference in reactivity or reduction potential between two metals.[108] This type of reaction is extensively exploited to generate hollow metallic nanoparticles, which find applications in energy storage, catalysis, and medicine.[109, 110]

In the case of core-shell nanoparticles, when the shell metal is nobler than the core metal, the risk of oxidation for the less noble metal arises. This phenomenon is attributed to the transfer of electrons from the less noble core metal to the nobler metal with the higher standard potential.[111] The suppression of galvanic reaction still occupies many researchers. Several strategies have already been developed, such as the control of pH value, leading to the increase or decrease of the reduction potential

of a certain reducing agent. However, until now, the existing methods cover only specific bimetallic systems.[112-114]

2.4.4 Optical properties of nanoparticles

Metallic nanoparticles exhibit unique optical properties that distinguish them from bulk materials. These properties can be easily measured by UV-Vis spectroscopy. Gold and silver are characteristic examples of metallic materials with distinctive optical properties. Macroscopic gold exhibits a lustrous yellow appearance, while colloidal gold takes on a deep red color. In contrast, bulk silver appears as metallic gray, but silver nanoparticles can display a variety of colors, including yellow, orange, green, or gray, which are strongly influenced by their specific morphology, size, [115] and structure.[116] These distinct optical characteristics arise from the selective oscillation of free electrons, known as surface plasmons, which occur when metal nanoparticles interact with light, resulting in a phenomenon called surface plasmon resonance (SPR). The collective motion of conduction band electrons in response to the electric field of incident light, driven by Coulombic interactions with the nucleus, gives rise to the surface plasmons.[105, 117, 118] Surface plasmons are excited when the diameter of the observed particle is significantly smaller than the wavelength of the incident light.

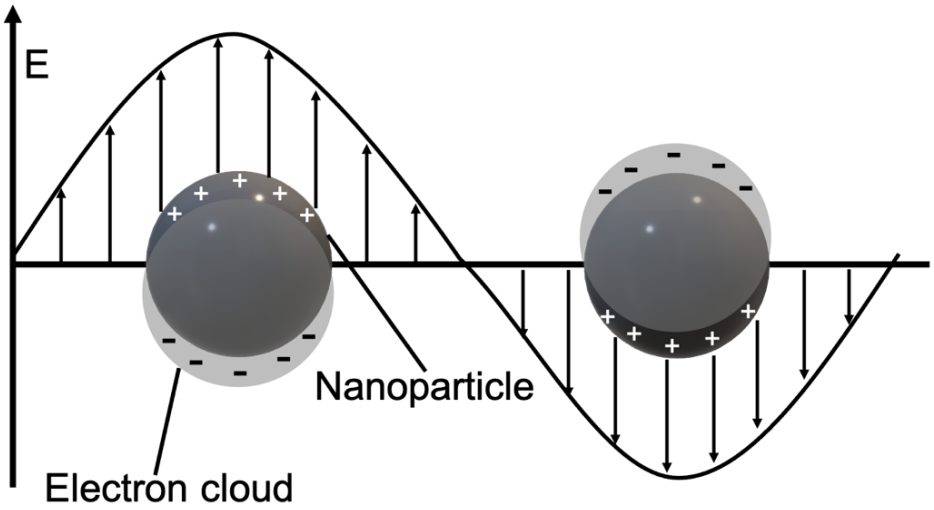

Figure 8. Schematic representation of the localized surface plasmon resonance of spherical nanoparticles due to collective oscillation of free electrons with incident light.

The specific features of surface plasmon resonance, including peak position and intensity, depend on various factors such as particle size, morphology, and interparticle distances. According to Mie's theory, spherical nanoparticles should exhibit one LSPR peak, whereas anisotropic structures should exhibit more peaks, depending on their shape.[116] For instance, silver nanowires and nanorods exhibit distinctive multiple peaks in their UV-Vis spectra, attributed to the oscillation of electrons along both the transversal and longitudinal surfaces. [119] In contrast, spherical nanoparticles typically display a single plasmon resonance peak. [120]

3. METHODS

3.1 Spectroscopical methods

3.1.1 Ultraviolet-visible spectroscopy (UV-Vis)

Ultraviolet-visible spectroscopy is a technique that involves irradiating a sample with light in the ultraviolet (UV, 200-380 nm) and visible (Vis, 380-800 nm) regions of the electromagnetic spectrum. This method relies on the interaction between light and the molecules' electrons in the sample. When light passes through the sample, specific wavelengths are absorbed by the molecules, while others are transmitted or scattered.[121] The intensity of light absorbed by the sample is directly related to its concentration and the path length that the light travels through the sample. This relationship is described by the *Beer-Lambert Law*, which is expressed by the following mathematical equation (3):

$$A = \log\left(\frac{I_0}{I}\right) = \varepsilon\, c\, d \qquad (3)$$

A absorbance,

I_0 incident light intensity,

I transmitted light intensity,

ε extinction coefficient,

c sample concentration,

d light path length

Depending on the application, UV-Vis spectroscopy can be used for qualitative and quantitative analysis. In quantitative analysis, the concentration of a substance in a sample can be determined using equation 3 by measuring its absorbance at specific ultraviolet and visible wavelengths. The qualitative analysis focuses on observing the absorbance patterns and identifying specific compounds or functional groups based on their characteristic absorption spectra. In this work, UV-Vis spectroscopy was used

for qualitative analysis. Some metal nanoparticle structures, such as gold and silver nanoparticles with a size above 5 nm, exhibit surface plasmon resonance (SPR). In this case, the surface plasmons are excited by the absorption of electromagnetic waves, leading to characteristic absorption bands in the UV-Vis spectrum. The shape of the plasmon absorption band and the maximum position can indicate shape, particle size, specific surface processes, and even the dispersion of the sample.[92, 121-123]

3.1.2 Atomic absorption spectroscopy (AAS)

Atomic absorption spectroscopy (AAS) is an analytical technique used for the qualitative and quantitative detection of specific elements in a sample. This method relies on light absorption by free ground-state atoms in the gaseous phase. Typically, the sample is in liquid form, obtained through dissolution or digestion methods. It is then introduced into an atomizer, a flame, a graphite furnace, or inductively coupled plasma (ICP), where it undergoes vaporization to form free atoms followed by thermal excitation. A suitable light source, such as a hollow cathode lamp, emits light at a specific wavelength corresponding to the absorption line of the element to be analyzed. The emitted light beam passes through the atomized sample, causing the ground-state atoms to absorb light at characteristic wavelengths unique for each element. The extent of the absorption is directly proportional to the concentration of the element in the sample, as described by the *Beer-Lambert Law* (eq. 3).[124] A calibration curve is established beforehand to determine the element's concentration in the sample. The curve is constructed by analyzing different concentrations of standard solutions with known analyte concentrations.

All atomic absorption spectroscopy measurements in this work were conducted by Beate Römer and Robin Meya in the Laboratory of Microanalysis at the University Duisburg-Essen. A Thermo Electron M-Series instrument (Thermo Fischer Scientific) was used.

- Silver nanoparticle sample preparation:

A total of 20 µL of silver nanoparticle dispersion was mixed with 80 µL nitric acid 65% and then diluted with ultra-pure water to a final volume of 5 mL.

- Silver-gold nanoparticle sample preparation:

Two samples of 60 µL each of bimetallic nanoparticle dispersion were prepared. A sample was mixed with 140 µL nitric acid 65% for silver determination. The other sample was mixed with 140 µL *aqua regia* for gold determination. They were then diluted with ultra-pure water to a final volume of 5 mL.

- Palladium nanoparticle sample preparation:

A total of 10 µL of palladium nanoparticles dispersion was mixed with 390 µL nitric acid 65% and then diluted with ultra-pure water to a final volume of 5 mL.

- Palladium-platinum nanoparticle sample preparation:

A total of 20 µL of Palladium-platinum nanoparticles dispersion was mixed with 180 µL *aqua regia* and then diluted with ultra-pure water to a final volume of 5 mL.

Detection limits: silver 0.05 mg L^{-1}, gold 1.00 mg L^{-1}, palladium 1.2 mg L^{-1}, platinum 24.0 mg L^{-1}.

3.2 Colloid-chemical methods

3.2.1 Dynamic light scattering (DLS) and ζ-Potential

Dynamic light scattering (DLS) is a technique to determine the size distribution of particles or molecules in a solution providing valuable information about the dispersity of the sample. The underlying principle of DLS involves analyzing the fluctuations in the intensity of the laser light, which is scattered by the particles in the dispersion. Typically, during a DLS analysis, a monochromatic laser beam is directed through a sample containing particles—nevertheless, the particles in a dispersion exhibit random motion due to Brownian motion. As a result, the intensity of the scattered light continuously changes and is collected at a 173° angle and directed toward a detector. The intensity fluctuations are measured and analyzed using an autocorrelation function, which correlates the time at which the intensity fluctuations occur, enabling the determination of particle diffusion.[125, 126] If the temperature and the viscosity of the dispersant are known, the hydrodynamic diameter of the particles can be calculated using the Stokes-Einstein equation (4):[127]

$$R_H = \frac{k_B T}{6\pi\,\eta\,D} \tag{4}$$

R_H hydrodynamic diameter,
k_B Boltzmann constant,
T temperature of the medium,
η viscosity of the dispersant,
D diffusion coefficient

The hydrodynamic diameter involves the size of the particles along with ions, fluid molecules, and stabilizing/capping agents. Consequently, the average particle size obtained by dynamic light scattering analysis is usually overestimated.

In addition to providing average particle size, this technique enables the determination of the colloidal system's polydispersity index (PDI). The PDI quantifies the degree of particle size distribution in the colloidal system. A PDI value ≤ 0.3 indicates a monodisperse particle distribution, suggesting a system with uniform particle sizes. The PDI value is calculated by the dynamic light scattering software using the full width at half maximum (FWHM) and Gaussian peak fitting (x_c) based on equation 5:

$$PDI = \left(\frac{FWHM}{x_c}\right)^2 \tag{5}$$

Another function of this instrument is the measurement of the ζ-potential of the colloidal system. ζ-potential is a measure of electrostatic charge on the surface of particles or colloidal dispersions suspended in a medium. It provides valuable information about the stability of the particles in solution. Nanoparticles with ζ-potential values greater than ±30 mV are considered stable in the colloidal dispersion, as the repulsive electrostatic forces between particles prevent agglomeration, as discussed in Chapter 2.3. On the other hand, values lower than ±25 mV may result in agglomeration of the nanoparticles due to the attractive van der Waals interactions.[128]

However, dynamic light scattering has certain limitations that should be considered. It is most suitable for particles under 1 µm, as its accuracy decreases for larger particles. Interpreting data obtained from samples with a broad size distribution can be challenging since the software assumes a monodisperse sample. Moreover, the average particle size can be overestimated when particles form agglomerates or aggregates. In the case of highly concentrated samples, multiple scattering can occur, leading to distorted measurements.[125, 129, 130] Finally, as the *Stokes-Einstein* (eq. 4) indicates, this method assumes spherical particles, making the technique less accurate when dealing with particles of different shapes, such as anisotropic particles (e.g., rods).

3.2.2 Differential centrifugal sedimentation (DCS)

Differential centrifugal sedimentation is another technique used to determine the particle size distribution of colloidal systems based on sedimentation behavior under centrifugal force. In this technique, the sample to be analyzed is injected in a rotating transparent rotor filled with a mixture of gradient sucrose solutions (Fig.9). As the rotor spins, the particles in the suspension experience a sedimentation force dependent on their size and density. Larger and denser particles sediment more rapidly, while smaller and lighter particles sediment more slowly.

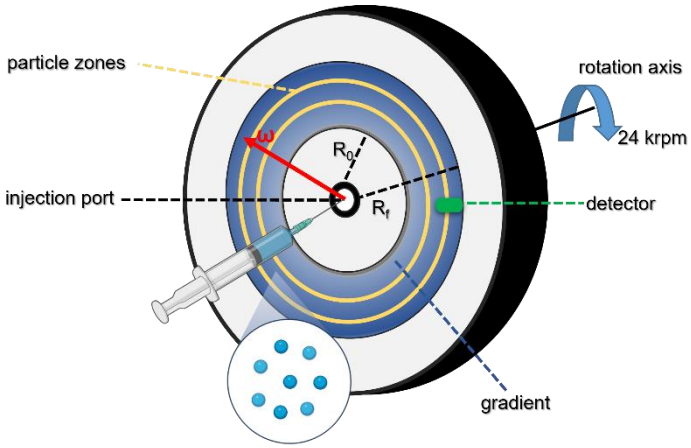

Figure 9. Schematic representation of a spinning rotor of a differential centrifugal sedimentation instrument.

During the DCS analysis, a laser beam is directed through the sample and scattered by the particles in the solution. The scattered light is collected on the detector, which records the velocity of the sedimentation of the particles as a function of time. Before injecting the sample, a calibration standard consisting of particles with known size is measured. The particle diameter is then determined using the Stokes equation (eq. 6).[131]

$$D = \sqrt{\frac{18\,\eta\,\ln\frac{R_f}{R_0}}{(\rho_p - \rho_f)\,\omega^2\,t}} \tag{6}$$

D particle diameter,

η viscosity,

R_f outer disc radius,

R_0 inner disc radius,

ρ_p particle density,

ρ_f fluid density,

ω angular velocity,

t sedimentation time

One of the drawbacks of this method, especially for nanoparticle characterization, is the tendency to underestimate particle size. This relies primarily on the fact that the software uses the density of the particle core (eq. 6) for the diameter calculation. However, nanoparticles often have a polymeric shell around them, which has a different density than the core. Consequently, the given density does not reflect the actual density of the nanoparticle, leading to an underestimation of the size.[125, 132]

3.3 Electron Microscopy

3.3.1 Scanning electron microscopy (SEM)

Scanning electron microscopy (SEM) is a powerful imaging technique to investigate diverse samples' surface morphology and structure at high magnification and resolution. It offers detailed information about the topography, composition, and elemental analysis of a wide range of materials. In scanning electron microscopy, a focused electron beam (primary electrons, PE) is directed on the sample's surface. The sample, placed in vacuum, is then scanned. The interactions between the electron beam and the sample generate secondary electrons (SE), backscattered electrons (BSE), and X-rays. (Fig. 10)

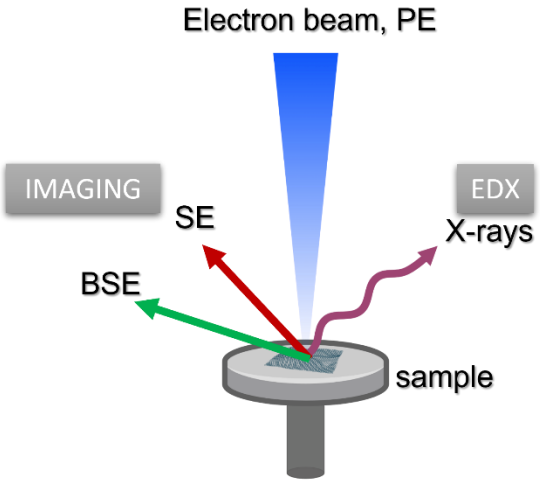

Figure 10. Schematic representation of the detected signal types in SEM.

Secondary electrons are low-energy electrons (typically less than 5 eV) produced through inelastic scattering of the primary electrons. They carry valuable information about the sample's topography and morphology. When secondary electrons are detected, areas of the sample farther from the detector appear darker. In contrast, regions closer to the detector and with higher emissions of secondary electrons appear brighter. This contrast allows the visualization of surface features and topological variations. On the other hand, backscattered electrons are produced by the elastic scattering of the primary electrons, revealing details related to atomic composition and density variations in the sample. Denser and heavier elements tend to scatter more electrons, appearing lighter, while lighter elements scatter fewer electrons and appear darker. [125, 133, 134] To ensure proper imaging and analysis in scanning electron

microscopy, it is necessary for the samples to have sufficient conductivity. If a sample is not inherently conductive, sputtering with a conductive metal, such as gold or palladium, is employed.

In this work, all to-be-examined samples are metallic nanoparticles. Thus, no sputtering was required. Before each measurement, 10 µL of a nanoparticle dispersion was drop-cast on a silicon wafer, fixed on an aluminum sample holder with carbon tape, and let dry.

All scanning electron and transmission microscopy measurements and energy dispersive spectroscopy, as well as the *in-situ* scanning electron microscopy experiments, were carried out by Dr. Kateryna Loza at University Duisburg-Essen. SEM and STEM measurements were performed with an Apreo S LoVac instrument, equipped with a micro-heating stage and coupled with energy-dispersive X-ray spectroscopy (UltraDry EDS detector) from ThermoFischer Scientific.

3.3.2 High-resolution transmission electron microscopy (HRTEM)

Transmission electron microscopy is one more powerful imaging technique that allows high-resolution visualization and analysis of the internal structure of the samples. While sharing some principles with scanning electron microscopy, a transmission electron microscope operates by passing an electron beam through the sample and collects the transmitted electrons to form an image. It provides high-resolution images, enabling a detailed examination of the sample's internal features and allows for the visualization of atomic arrangement.

Scanning transmission microscopy (STEM), on the other hand, combines the principles of TEM with SEM. In STEM, the electron beam is focused into a fine probe and scanned across the sample, similar to SEM. The transmitted electrons are collected to form an image, but unlike TEM, the image is formed by scanning the probe rather than by directly transmitting the beam through the sample.

The most common imaging mode is called bright-field imaging. In this mode, electrons passing through the sample interact with a fluorescent screen or detector, generating an image. Bright regions in the image correspond to areas where fewer electrons were transmitted, indicating denser or thicker parts in the sample. Another mode is the high-angle annular dark field (HAADF), which enables high-resolution and

contrast-enhanced images of the atomic structure and composition of the sample. Contrast derives from the atomic number (Z) of the elements present in the sample, allowing for enhanced visualization of different elements. Transmission electron microscopy is not limited to imaging; it also enables high-resolution diffraction analysis. Electron diffraction patterns are generated when the electron beam interacts with the crystalline structure of the sample. These patterns contain information about the crystal lattice arrangement allowing for the determination of crystallographic properties, such as crystal orientation, lattice spacing, and defects.[135]

A crucial factor in transmission electron microscopy is the thickness of the sample. Specimens to be examined should have a thickness of less than 100 nm.[134] This limitation ensures that the electrons can sufficiently penetrate the sample and provide meaningful information during imaging.

Unlike SEM, for STEM and TEM measurements, 10-20 µL of the sample was drop-cast on a copper grid, coated with an ultra-thin amorphous carbon film, and dried in air at ambient conditions.

All transmission electron microscopy measurements, energy-dispersive spectroscopy, and the *in-situ* transmission electron microscopy experiments were carried out by Dr. Kateryna Loza in the Ernst-Ruska-Zentrum of the Research Center Jülich. TEM was performed with a FEI Titan microscope, equipped with a Cs-Probe corrector (CEOS company), operating at 300 kV at 10^{-5} Pa. [136] *In-situ* heating TEM was carried out with a TEM heating sample holder (Wildfire, DENS Solutions Company). Finally, EDS was performed with a Hitachi HF5000 microscope, equipped with a Cs-Probe detector (Hitachi) coupled with an EDS unit (Oxford Instruments Aztec Energy TEM Advanced EDX System Ultrim TLE) operating at 200 kV at 10^{-5} Pa.

3.3.3 Energy-dispersive X-ray spectroscopy (EDS)

Energy dispersive X-ray spectroscopy (EDX or EDS) is an analytical technique used in electron microscopy to identify and quantify the elemental composition of materials. It provides valuable information about the chemical composition, distribution of elements, and elemental mapping within a given sample. It is typically performed in conjunction with scanning or scanning transmission electron microscopy. During the analysis, an electron beam interacts with the sample, ionizing inner shell electrons from atoms within the material. This ionization process creates vacancies in the electron shells, filled by outer shell electrons, releasing characteristic X-rays (Fig. 11).

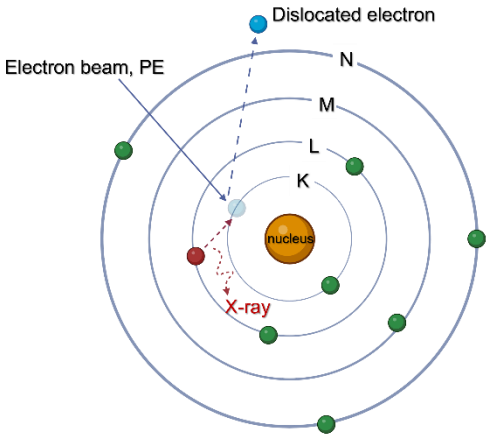

Figure 11. Generation of characteristic X-rays after the primary electron interactions in an atom.

The emitted X-rays are collected by an energy-dispersive detector, which measures their energy and intensity. Each element has different characteristic X-ray energies corresponding to its atomic structure. The elements present can be identified by analyzing the energy spectrum of the collected X-rays. The intensity of the X-ray peaks is proportional to the concentration of the corresponding elements.

Energy-dispersive X-ray spectroscopy can also be used for elemental mapping. Scanning the electron beam across the sample and collecting X-ray spectra at different locations can generate the spatial distribution of maps of different elements within the sample.[137] These elemental maps provide visual representations of how various elements are distributed within the sample, offering valuable information about the sample's composition and heterogeneity.

3.4 X-ray powder diffraction (PXRD)

X-ray powder diffraction is used to determine the crystallographic structure and phase purity of crystalline materials. By analyzing the resulting diffraction pattern, valuable information about the arrangement of atoms within a material's crystal lattice can be extracted, including the dimensions of the unit cell, crystal symmetry, and the positions of the particles. During the measurement, a beam of X-rays is directed onto a powder sample. X-rays are utilized because their wavelength is on the same scale as the interatomic spacing in crystals. As the X-ray interacts with several atomic layers within the sample, both constructive and destructive interference can occur. When the diffraction angle of the incident X-ray beam satisfies *Bragg's law* (eq. 7), constructive interference takes place, resulting in a sharp diffraction signal. If this is not the case, in other angles occurs, destructive interference, leading to diminished or no observable diffraction.

$$n\,\lambda = 2\,d\,\sin\vartheta \tag{7}$$

n positive integer

λ X-ray wavelength

d lattice plane distance

ϑ *Bragg* angle

The width of the obtained signal in a diffraction pattern allows calculating the crystallite size D using the *Scherrer* equation (eq. 8)[138] and the microstrain with the Stokes-Wilson equation (eq. 9).

$$D = \frac{K\,\lambda}{\beta\,\cos\vartheta} \tag{8}$$

$$\varepsilon = \frac{\beta}{4\,\tan\vartheta} \tag{9}$$

K Scherrer factor

λ X-ray beam wavelength

β full width at half maximum (FWHM) of a reflex

ϑ Bragg angle

ε microstrain

In the case of a cubic system, e.g., silver fcc phase, the lattice parameter *a* can be calculated by the following equation (eq.10)

$$a = \frac{\lambda}{2\,\sin\vartheta}\sqrt{h^2 + k^2 + l^2} \tag{10}$$

All the X-ray measurements, *in-situ* experiments, and the Rietveld refinement were carried out by Dr. Oleg Prymak, Department of X-ray Diffraction at the University of Duisburg-Essen. The PXRD measurements were performed with a Bruker D8 Advance instrument in Bragg Brentano geometry mode with Cu Kα radiation (λ = 1.54 Å; 40 kV, 40 mA) with a silicon single crystal sample holder to minimize background scattering. *In-situ* XRD was carried out on a Panalytical Empyrean instrument in Bragg-Brentano mode with Cu Kα radiation (40 kV, 40 mA), equipped with a high-temperature chamber HTK 16 (Anton Paar).

3.5 Thermogravimetric Analysis (TGA)

Thermogravimetric analysis (TGA) is a thermal analysis technique used to study the changes in the mass of a sample as a function of temperature or time. It provides information about materials' thermal stability, composition, and decomposition kinetics. During a typical thermogravimetric experiment, a certain amount of a sample is heated in a controlled environment, and its mass is continuously monitored. As the temperature increases, various physical and chemical phenomena can occur, including vaporization, sublimation, desorption, decomposition, and oxidation. The resulting thermogram shows characteristic features such as mass loss or gain steps, plateaus, or continuous changes, providing insights into the thermal behavior and composition of the sample. [139-141]

A Netzsch STA 449 F3 instrument was used in the experiments conducted for this work. The samples were heated with a rate of 5 K min^{-1} up to 1273 K in a dynamic oxygen atmosphere.

4. EXPERIMENTAL SECTION

4.1 Software / Databases

Table 2. Software and databases used.

Program/database	Purpose	Developer
Bio render	Scientific image and illustration	BioRender
ChemDraw	Structural representations	PerkinElmer
Chemix	Drawing lab diagrams	Chemix International Bv
EndNote X20	Citation management	Clarivate
ImageJ	Image processing	National Institutes of Health
Microsoft Office	Text processing, graphic design, data calculation	Microsoft
Origin Pro 2022	Graphing and data analysis	OriginLab corporation
Photoshop	Image editing	Adobe Inc.

4.2 Devices

Table 3. Devices used.

Devices	Producer and device model
Analytical disc centrifuge	CPS Instruments, DC 24000
Atomic absorption spectroscopy	Thermo fischer scientific ThermoElectron, M-Series
Centrifuge	Eppendorf, Centrifuge 5430
Dynamic light scattering	Malvern Zetasizer, Nano ZS ZEN 3600
Energy dispersive X-ray spectrometer	Thermo Fischer Scientific, UltraDry EDS
Lyophilizer	Christ, Alpha 2-4 LSCplus
Scanning electron microscope	ThermoFischer scientific, Apreo S LoVac
Syringe pump	KD Scientific, KDS100 legacy syringe pump
Thermobalance	Netzsch, STA 449 F3
Transmission electron microscope	CEOS, FEI Titan 80-300
Transmission electron microscope	Hitachi HF5000
Ultraviolet – visible spectrometer	Thermo Scientific, Genesis 50
Ultracentrifuge	Thermo fischer scientific, Sorwall WX Ultra Series
Ultrasonic bath	Elma, Elmasonic S10
Vortex	Scientific Industries, Vortex-Genie 2

X-ray powder diffractometer	Bruker, D8 Advanced (Bragg-Brentano geometry)
X-ray powder diffractometer (*in-situ* experiments)	PANalytical Empyrean (Debye-Scherrer geometry and high-temperature X-ray diffraction in Bragg-Brentano geometry)

4.3 Chemicals

Table 4. Chemicals used.

Chemical	Producer	Purity
Acetone	Fisher Chemicals	≥99.8%
Diethylene glycol	Sigma-Aldrich	99%
Ethylene glycol anhydrous	Sigma-Aldrich	99.8%
Hydrochloric acid 37%	VWR Chemicals	p.a.
Iron chloride anhydrous	Karl Roth	≥98.5%
Lanthanum hexaboride	NIST	
Nitric acid 65%	Fisher Chemicals	p.a.
Platinic acid	Sigma-Aldrich	
Poly(N-vinylpyrrolidone) (M_w = 40,000 g mol^{-1})	Sigma-Aldrich	
Poly(N-vinylpyrrolidone) (M_w = 55,000 g mol^{-1})	Sigma-Aldrich	
Poly(N-vinylpyrrolidone) (M_w = 29,000 g mol^{-1})	Sigma-Aldrich	
Potassium bromide	Sigma-Aldrich	≥99%
Potassium tetrachloroplatinate	Sigma-Aldrich	≥99%
Silver nitrate	Karl Roth	
Silver foil	Goodfellow	≥99.9%

Sodium chloride	Fisher Chemicals	≥99.5%
Sodium hydroxide	Fisher Chemicals	
Sodium tetrachloropalladate	Sigma-Aldrich	≥99.9%
Tetrachloridoauric acid	Self-prepared by the dissolution of elemental gold	
Trisodium citrate dihydrate	AppliChem	p.a.

4.4 Synthesis of monometallic nanoparticles

4.4.1 Water-based syntheses of monometallic nanoparticles

4.4.1.1 Synthesis of silver nanospheres with glucose

The synthesis of quasi-spherical silver particles obtained from the reduction of silver nitrate with glucose using polyvinylpyrrolidone as a stabilizer is a well-established synthesis[132, 142], first proposed by Wang et. [143]

In a typical synthesis, 2.00 g D-glucose (11.10 mmol) and 1.00 g polyvinylpyrrolidone (9.00 mmol based on the molar mass of the monomer, M_w = 40,000 g mol^{-1}) were dissolved in 40 mL ultra-pure water in a 100 mL one-round neck-bottom flask. The mixture was heated at 90 °C in an oil bath and vigorously stirred for 45 minutes. Next, 500 mg of silver nitrate (2.94 mmol) was dissolved in 1 mL ultrapure water and rapidly added to the synthesis mixture. The reaction mixture was stirred for an additional hour at 90 °C. Upon adding the precursor, the initially transparent mixture gradually changed color from light yellow to orange and finally to vivid opaque green. An ice bath was used to stop the reaction, and the mixture was quickly cooled down to room temperature. The resulting silver nanoparticle dispersion was washed with water and centrifuged with an ultracentrifuge at 30,000 rpm (66,000 *g* for 30 minutes, repeating this process three times. After each centrifugation step, the supernatant fluid was discarded, and the particles were dispersed with ultrasonication. Following the final centrifugation, the particles were collected and dispersed in a small amount of degassed argon-saturated ultra-pure water to prevent possible oxidation of the nanoparticles. The dispersion was then stored at 4 °C.[144]

4.4.1.2 Synthesis of 18 nm palladium nanocubes with ascorbic acid

The synthesis of palladium nanocubes obtained from the reduction of sodium tetrachloropalladate with ascorbic acid, stabilized with polyvinylpyrrolidone was performed based on a protocol developed by Jin *et al.*[145]

To obtain palladium nanocubes, 600 mg potassium bromide (5.00 mmol), 60 mg ascorbic acid (0.35 mmol), and 105 mg PVP (0.90 mmol based on the monomer molar mass, M_w = 55,000 g mol^{-1}) were dissolved in 8 mL ultrapure water and heated up to

80 °C in an oil bath. The mixture remained at 80 °C for 10 minutes, and the reaction vessel was closed with a glass cap. Afterward, 3 mL of a 0.06 M of aqueous sodium tetrachloropalladate solution was quickly added to the reaction solution, which was left at 80 °C under constant stirring for 3 hours. The solution color turned red-brown upon adding the metal precursor, and by the end of the reaction, it was dark brown. The reaction was then stopped by cooling it to room temperature with an ice bath, and the nanocubes were isolated with centrifugation at 14,200 rpm (21,190 *g*) for an hour. After the centrifugation, the supernatant was discarded, the remaining colloid was dispersed in ultra-pure water, and the sample was again introduced into the centrifuge. The same purification process was repeated three more times. The resulting nanoparticles were dispersed in a small amount of degassed argon-saturated ultra-pure water and stored at 4 °C for characterization and further experiments.

4.4.1.3 Synthesis of 45 nm palladium nanocubes with ascorbic acid (seed and growth)

For the synthesis of larger palladium nanocubes with an average size of about 45 nm, 18 nm palladium nanocubes (Chapter 4.4.1.2) were used as seeds for the further growth of the nanostructures.

For the synthesis, 150 mg PVP (1.35 mmol based on the monomer molar mass, M_w = 55,000 g mol^{-1}), 90 mg ascorbic acid (0.51 mmol), 450 mg KBr (3.78 mmol) and, 1.8 mg of the synthesized Pd nanocubes (16.90 µmol) were added to a 50 mL round-bottom flask with 12 mL ultra-pure water. Then the reaction mixture was heated to 40 °C in an oil bath. After 20 minutes, 5 mL of a 0.02 M Na_2PdCl_4 solution was added, and the mixture was left under stirring at 40 °C for 24 hours. An ice bath was used to stop the reaction. Centrifugation was performed at 14,200 rpm (21,190 *g*) for 30 minutes to isolate the nanoparticles. The purification process was repeated three times. After each centrifugation, the supernatant was discarded, and the sample was dispersed in ultra-pure water. In the last step, the isolated nanoparticles were dispersed in argon-saturated ultra-pure water and stored at 4 °C for characterization.

4.4.2 Polyol-based syntheses of monometallic nanoparticles

4.4.2.1 Polyol method

The polyol method or polyol process is a versatile chemical synthesis widely employed for producing metallic nanoparticles. This process involves reducing metal precursors within a polyol solvent under carefully controlled reaction conditions.

In this method, polyols act as solvents, reducing and stabilizing agents. Polyols are organic compounds containing more than two hydroxyls (-OH) groups, such as glycerol, propanediol, ethylene glycol, and its derivatives. The presence of the -OH groups are responsible for the high boiling points and viscosities. As a result, they allow reactions to occur at higher temperatures, up to 328 °C, without using autoclaves. [88] During this reaction, the polyol molecules undergo oxidation, facilitating the reduction of metal salts to ions and subsequently to metal nuclei which then nucleate to form metal nanoparticles. [146] The addition of different capping agents and the careful control of parameters like temperature, time, and concentration of the reagents allow the kinetic control of the synthesis, leading to controlled particle growth with specific shapes and sizes.[52, 88, 147] [148]

$$2\ HOCH_2CH_2OH \rightarrow 2\ CH_3CHO + 2\ H_2O \quad (11)$$

$$2\ Ag^+ + 2\ CH_3CHO \rightarrow CH_3CHO\text{-}OHCCH_3 + 2Ag^0 + 2H^+ \quad (12)$$

Figure 11. Reaction mechanism of the reduction of silver by ethylene glycol in a typical polyol synthesis proposed by Im *et al*. [149]

4.4.2.2 Synthesis of silver nanowires (polyol method)

The synthesis of the silver nanowires was carried out after a well-known protocol developed by Schuette *et al*.[150]

In a 100 mL two-neck round-bottom flask, 334 mg of polyvinylpyrrolidone (3.00 mmol, based on the molar mass of the monomer, M_w = 55,000 g mol^{-1}) was dissolved in 20 mL anhydrous ethylene glycol. The solution mixture was heated under reflux and constant stirring up to 180 °C while one neck of the flask remained open. After 5 minutes, 50 µL of 0.43 M silver nitrate and 50 µL sodium chloride solution (also 0.43 M) were quickly and simultaneously added to the stirring mixture. The solution was left for 25 minutes at 180 °C. In the meantime, the previously transparent solution became light white due to the formation of silver chloride seeds. Next, 10 mL of a 0.12 M silver nitrate solution was added using a syringe pump at a rate of 25 mL h^{-1} to initiate the formation of the silver nanowires. The solution gradually turned milky white and then grey as the reaction progressed. When silver swirls were visible on the solution's surface, the syringe pump was removed, and the remaining silver nitrate solution was added dropwise manually. The reaction mixture was stirred for 15 minutes and then quenched to room temperature with an ice bath.

For the purification process, the final mixture was diluted with 100 mL ultrapure water and centrifuged at 2000 rpm (666 *g*) for 30 minutes. After the first round of centrifugation, the product was washed with 1 mL of concentrated ammonia solution to remove any remaining silver chloride seeds. The purification process was continued two more times under the same centrifugation conditions. Finally, the particles were collected and dispersed in a small amount of degassed argon-saturated ultra-pure water and stored at 4 °C.

4.4.2.3 Synthesis of silver nanocubes (polyol method)

The synthesis of the silver nanocubes was performed based on a modified protocol by Dr. Helmlinger[151] and Dr. Pappert[152], first proposed by Im *et al*.[149]

To synthesize the silver nanocubes, 6 mL ethylene glycol was heated to 160 °C in a 50 mL round-bottom flask. The flask remained open while being constantly stirred for one hour. Then, 30 µL of a 0.1 M aqueous hydrochloric acid solution was added to the heated solution. In the meantime, two 0.1 M solutions were prepared: one silver nitrate

solution (0.47 mmol) and one polyvinylpyrrolidone solution (*Mw*= 55,000 g/mol, 0.72 mmol with respect to the monomer), both in ethylene glycol. Ten minutes after adding the hydrochloric acid solution, the two solutions were mixed thoroughly, and 6 mL of the resulting mixture was quickly added to the reaction mixture. The reaction vessel was tightly closed with a septum and remained under constant stirring at 160 °C for 20 hours. Upon the addition of the metal precursor and the capping agent, the reaction solution from transparent turned to milky-white, indicating the formation of silver chloride seeds. Over time, the color of the reaction turned orange and eventually ochre/yellow/green. The reaction was stopped by quenching to room temperature with an ice bath.

To remove the excess ethylene glycol, the sample was washed once with acetone and centrifuged at 14,200 rpm (21,190 *g*) for 30 minutes. The isolated silver nanocubes were purified by washing them three times with ultra-pure water and repeating the centrifugation step under the same conditions. Before the last centrifugation step, the dispersion was filtered with a syringe cellulose filter with a pore size of 45 µm. Finally, after the last centrifugation step, the resulting particles were dispersed in a small amount of degassed argon-saturated ultra-pure water and stored at 4 °C for subsequent experiments and characterization.

4.5 Synthesis of bimetallic nanoparticles

4.5.1 Synthesis of core-shell silver-gold nanocubes

The generation of core-shell silver-gold nanocubes was based on a protocol proposed by Yang *et al*.[111] that was accordingly optimized. Silver nanocubes obtained from a previously described synthesis were used as seeds. 0.4 mg of silver nanocubes were dispersed in 30 mL ultra-pure water under constant stirring. Then 800 µL of a 0.1 M ascorbic acid solution was added to the dispersion. The pH levels were suitably adjusted to 12 with the required NaOH 1 M solution volume. For the generation of the shell, a 0.06 M tetrachloroauric acid solution was added dropwise to the reaction mixture with a syringe pump with an additional velocity of 0.15 mL min^{-1}. The dispersion color turned from yellow to transparent purple during the metal precursor addition.

The nanoparticles were isolated through centrifugation at 14,200 rpm (21,190 *g*) for 30 minutes. The exact process was repeated three times, and the end product was finally dispersed in a small amount of degassed argon-saturated ultra-pure water and stored at 4 °C for further experiments and characterization.

4.5.2 Synthesis of platinum nanocages

The synthesis of platinum nanocages was carried out according to a modified protocol based on a synthesis of Wojtysiak *et al.*[153]

Silver nanocubes obtained from a previously described synthesis were utilized as sacrificial templates to synthesize platinum nanocages. In a two-neck round-bottom flask, 10 mL of a 1 mM aqueous potassium tetrachloroplatinate solution (0.01 mmol) was refluxed at 100 ºC for one hour. Subsequently, the pH of the solution was adjusted to 2 by adding the appropriate amount of a 2 M hydrochloric acid solution. To initiate the formation of the platinum nanocages, 800 µL of a 38.8 mM aqueous sodium citrate solution was added to the reaction mixture. After 5 minutes, 0.9 mg (0.008 mmol) of silver nanocubes were rapidly introduced into the solution, and the reaction mixture was stirred for an additional hour at 100 ºC.

The solution was subjected to centrifugation at 14,200 rpm (21,190 *g*) for 30 minutes to isolate the platinum nanocages. This centrifugation step was repeated two more

times to ensure efficient separation. The resulting nanocages were washed with 200 µL of 33% ammonia solution to dissolve any residual silver chloride, followed by another round of centrifugation under the same conditions. The final product was washed with 200 µL of concentrated nitric acid to eliminate any remaining silver traces and obtain silver-free platinum nanocages. This step ensured the removal of any silver remnants. The resulting platinum nanocages were dispersed in a small amount of degassed argon-saturated ultra-pure water and stored at 4 °C for characterization.

4.5.3 Synthesis of core-shell palladium-platinum nanocubes

To synthesize palladium-platinum core-shell nanocubes, palladium nanocubes with a mean edge length of 18 nm, obtained from a previously described synthesis, were used as seed particles. In a 50 mL one-neck flask, a solution was prepared by dissolving 100 mg (0.57 mmol) of ascorbic acid, 54 mg (0.45 mmol) of potassium bromide, and 66.6 mg (0.60 mmol, based on the molar mass of the monomer, M_w = 55,000) polyvinylpyrrolidone in 12 mL of ethylene glycol. The mixture was heated up to 110 °C under stirring in an oil bath. Then, 1.7 mg (15.79 mmol) of the aqueous dispersion of palladium nanocubes (18 nm) was added to the reaction mixture. The flask was left open at 110 °C for an hour to evaporate the water content of the palladium colloid. A solution of sodium hexachloroplatinate (IV) hexahydrate in ethylene glycol was prepared to initiate the formation of the platinum shell. 19 mL of the solution (15.37 mmol) were added dropwise to the reaction mixture using a syringe pump at a rate of 4.0 mL h^{-1}. After the complete addition of the platinum precursor, the temperature was increased to 200 °C, and the reaction was allowed to proceed for another hour with the flask closed. To stop the reaction, the reaction vessel was removed from the oil bath and cooled to room temperature in an ice bath.

The final product was isolated by washing the solution with ethanol and centrifuging it at 14,200 rpm (21,190 *g*) for an hour. The supernatant was discarded, and the sample was dispersed in ultra-pure water. This washing and centrifugation process was repeated two more times. The resulting palladium-platinum nanoparticles were then dispersed in a small amount of degassed argon-saturated ultra-pure water and stored at 4 °C for characterization.

4.6 Thermal stability studies

In-situ, electron microscopy (SEM, TEM) and X-ray diffraction heating experiments were carried out on silver and core-shell silver-gold nanoparticles to examine their thermal behavior, stability, and crystallinity at elevated temperatures.

4.6.1 *In-situ* electron microscopy heating studies (SEM, TEM)

In-situ microscopy experiments enable the investigation of phenomena such as phase metal transformations, structural changes, sintering, and diffusion phenomena.

In-situ, scanning electron microscopy (SEM) experiments were performed with an Apreo S LoVac instrument from (ThermoFischer Scientific) equipped with a µ-heating holder. This holder allows rapid and precise heating of samples in a high vacuum up to 1200 °C. In contrast to the classic silica wafers widely used in scanning electron microscopy, a special MEMS (Micro-Electro-Mechanical Systems) chip was used (Fig.11 a). The heating element (Fig. 11b) is made of an electrically conductive material, formed as a meander allowing uniform temperature distribution. In the heated area, transparent windows are formed, which enable the visualization of the sample in the microscope (Fig.11c).

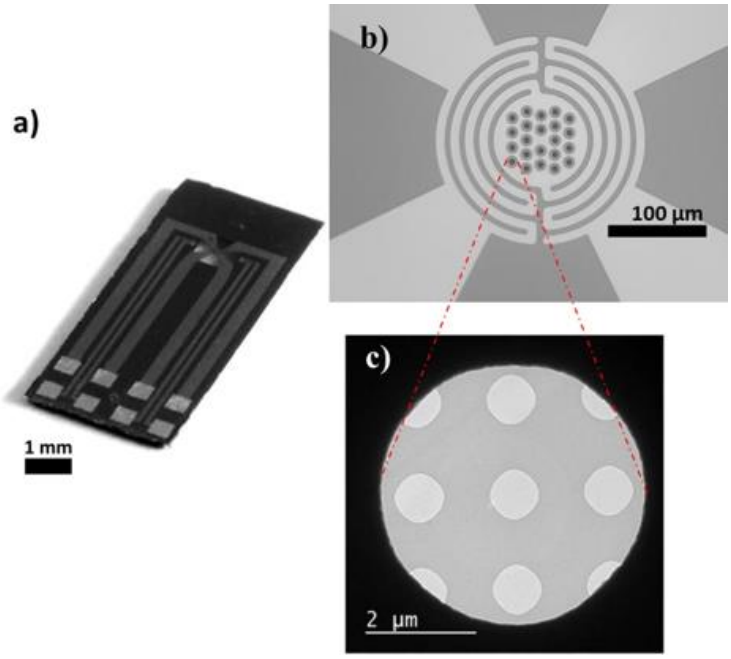

Figure 11. MEMS µ-Heater (a), the heating element (b), and the transparent windows (c). [154]

For this experiment, 10-20 µL of sample dispersion was drop-cast on the chip and gradually heated to 900 °C with a heating rate of 5 K min^{-1} under a pressure of 10^{-4} Pa. SEM images were taken every 1 K to generate at the end a video. Energy dispersive X-ray spectroscopy (EDS) was performed every 200 °C, and an EDS mapping was obtained.

In-situ transmission electron microscopy experiments were carried out with a FEI Titan microscope equipped with a Cs-probe corrector from CEOS Company, operating at 300 kV under a pressure of 10^{-5} Pa. A TEM heating sample holder (Wildfire, DENS Solutions Company, Fig.12) and a carbon-support nano-chip were used. The samples were heated to 900 °C with a heating rate of 5 K min^{-1}. Images were recorded every 5 °C and then combined to generate a video.

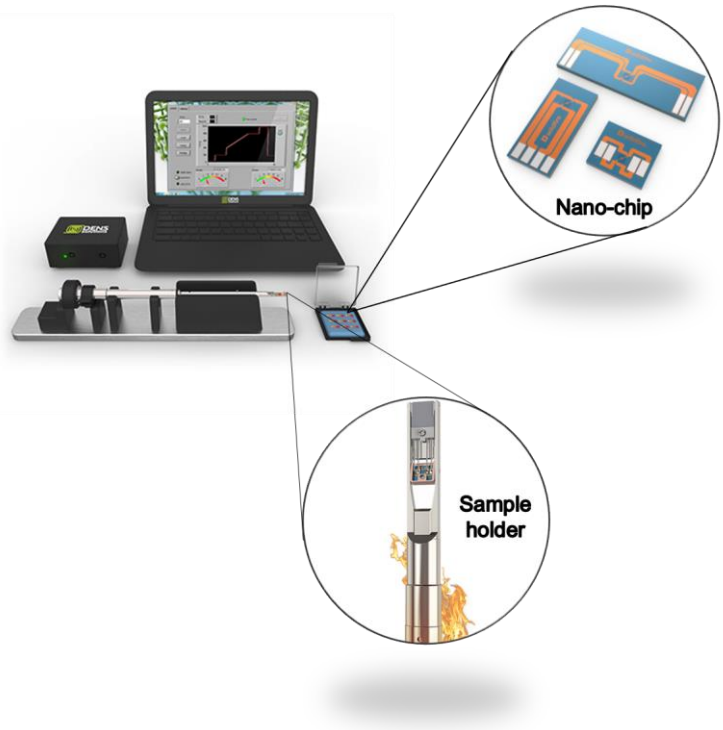

Figure 12. *In-situ* TEM set-up (Wildfire). [155]

4.6.2 *In-situ* powder X-ray diffraction heating studies

In-situ powder X-ray diffraction was performed on silver and silver-gold nanocubes to study the structural and physicochemical properties of the obtained nanoparticles. The experiments were conducted on a Panalytical Empyrean instrument in Bragg-Brentano mode with Cu K_α radiation (40 kV, 40 mA), equipped with a high-temperature chamber HTK 16 (Anton Paar).

For the *in-situ* measurement, the 7-10 syntheses batches were poolled together and freeze-dried after previous characterization with dynamic light scattering and electron microscopy. The obtained powders were mixed with microcrystalline lanthanum hexaboride (LaB_6) as standard reference material and deposited on a tantalum holder. LaB_6 enabled the quantitative analyses of the obtained results. The samples were measured in high vacuum (10^{-3} Pa) starting from room temperature to 800 °C with a heating rate of 5 K min^{-1} (Fig. 13). Once the temperature was achieved, was kept constant for one hour to record one diffractogram.

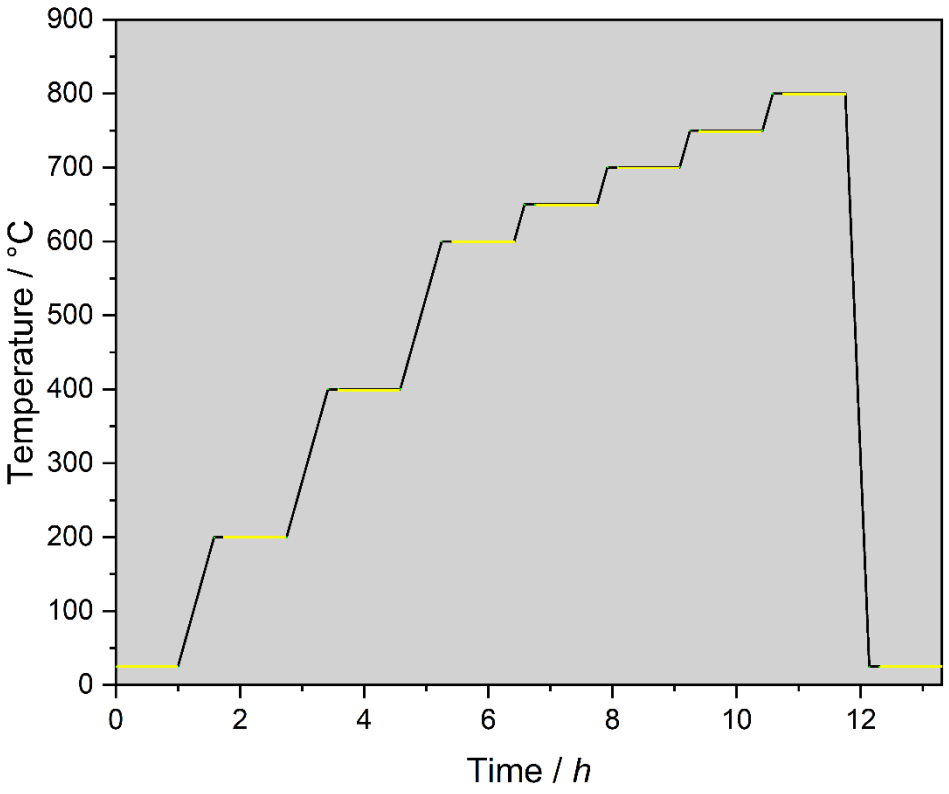

Figure 13. Time-dependent diagram of the heating steps during the *in-situ* XRD experiments. The yellow line indicates the actual measurement time.

5. RESULTS AND DISCUSSION

5.1 Water-based syntheses of monometallic nanoparticles

5.1.1 Characterization of silver nanospheres with glucose

The synthesized silver spherical nanoparticles were characterized by several analytical methods.

Ultraviolet and visible spectroscopy (UV-Vis) is commonly employed to investigate the optical properties of plasmonic nanoparticles such as silver nanoparticles. It is a quick method that can provide indications about the size and morphology of the synthesized nanoparticles. In the case of silver nanospheres, an absorbance maximum typically appears between 400 and 500 nm. This absorbance peak corresponds to the surface plasmon resonance of the nanoparticles. Generally, as the diameter increases, the absorbance peak becomes broader and shifts towards higher wavelengths (red-shift).[156, 157] The following UV-Vis spectrum (Fig. 14) of the synthesized silver nanospheres showed an absorbance maximum at 412 nm, which is usually in the range where silver spherical nanoparticles usually absorb.[158]

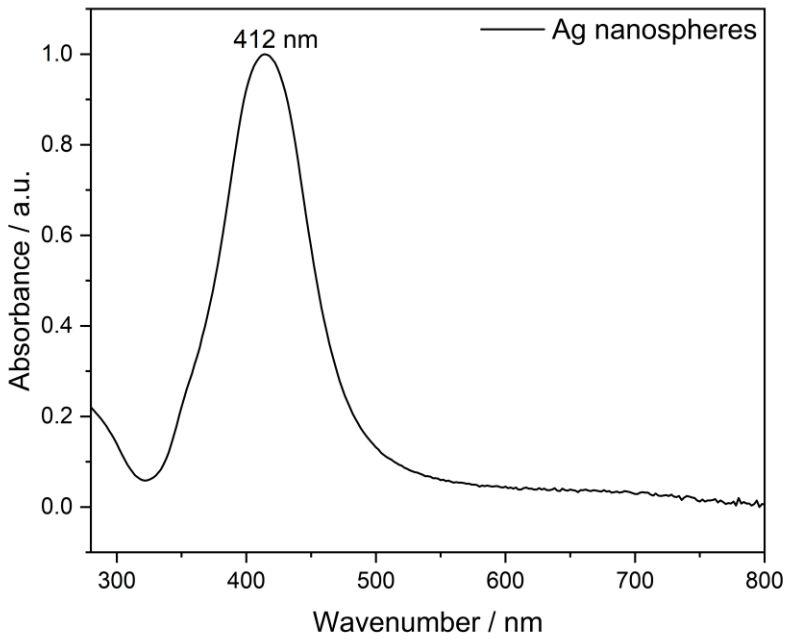

Figure 14. The UV-Vis spectrum of the silver nanospheres obtained from reducing $AgNO_3$ with glucose.

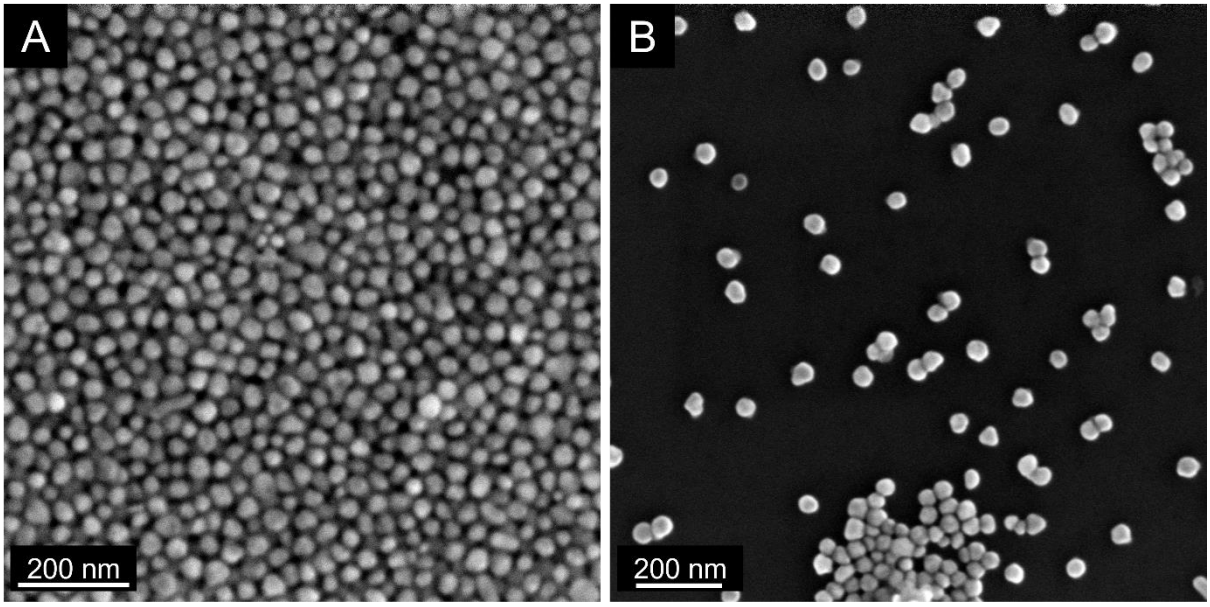

Figure 15. SEM images of silver nanoparticles obtained from the reduction of $AgNO_3$ with glucose.

Figure 15 shows typical scanning electron microscopy (SEM) images recorded with an accelerating voltage of 15 kV at different concentrations. It was evident that the synthesized nanoparticles exhibited a monodispersed and homogeneous distribution without any visible agglomerates. To obtain the average particle size of the metal core, 200 particles were digitally measured. The measurement showed a mean particle size of 33 nm with a standard deviation of ± 3 nm. The polydispersity index (PDI) was found to be 0.1, indicating a relatively narrow size distribution.

Although the nanoparticles are referred to as “spherical”, upon closer examination, they seem deformed. Silver nanoparticles obtained from glucose synthesis have been extensively studied in the literature. The deviation from a perfect spherical morphology can be attributed to their internal structure. Typically, silver nanoparticles grow in five-fold twinned crystalline structures, forming decahedral structures. These structures consist of five single-crystal tetrahedral units sharing a common edge. Each unit is enclosed by (111) facets, with a 70.53° angle, creating gaps closed by defects at the facets' boundaries (Fig.16).[83, 151, 159]

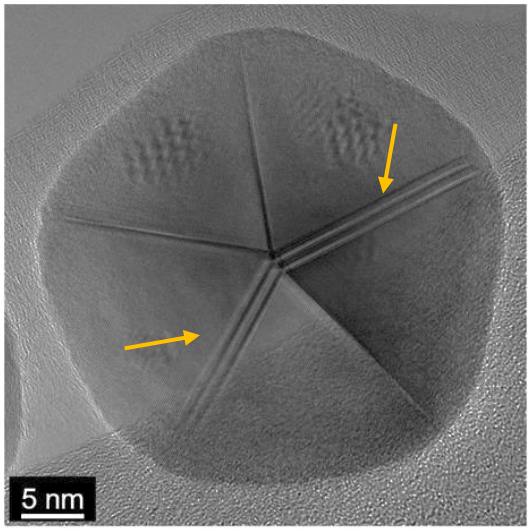

Figure 16. HRTEM image of a single five-fold twinned silver nanoparticle obtained from the glucose synthesis. Defects at the grain boundaries are marked with yellow arrows. The image was adapted from reference.[160]

Dynamic light scattering (DLS) was conducted to determine the size distribution of the silver nanoparticles.

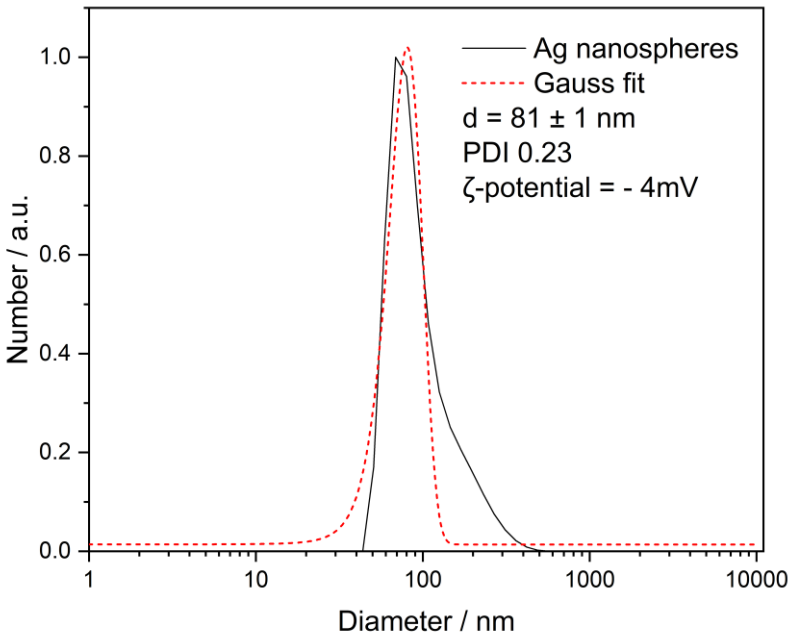

Figure 17. Particle size distribution was determined by DLS measurement of silver nanoparticles obtained from the reduction of $AgNO_3$ with glucose.

DLS measurement exhibited a monomodal size distribution with an average particle size of 81 ± 1 nm. The PDI value of 0.23 indicated that the colloidal system was monodisperse, as the value lay under 0.3, which agreed with what was observed in the SEM images (Fig.15).

To evaluate the colloidal stability of silver nanoparticles, ζ-potential was measured in ultra-pure water. The silver nanoparticles were stabilized with PVP, which is neutrally charged. Therefore, one would expect a value around zero, indicating steric stabilization due to the neutral PVP molecules surrounding the particles. However, it was found that the ζ-potential exhibited a slightly negative value (- 4 mV, pH=8).

The hydrodynamic size of the particles was also measured using differential centrifugal sedimentation (DCS).

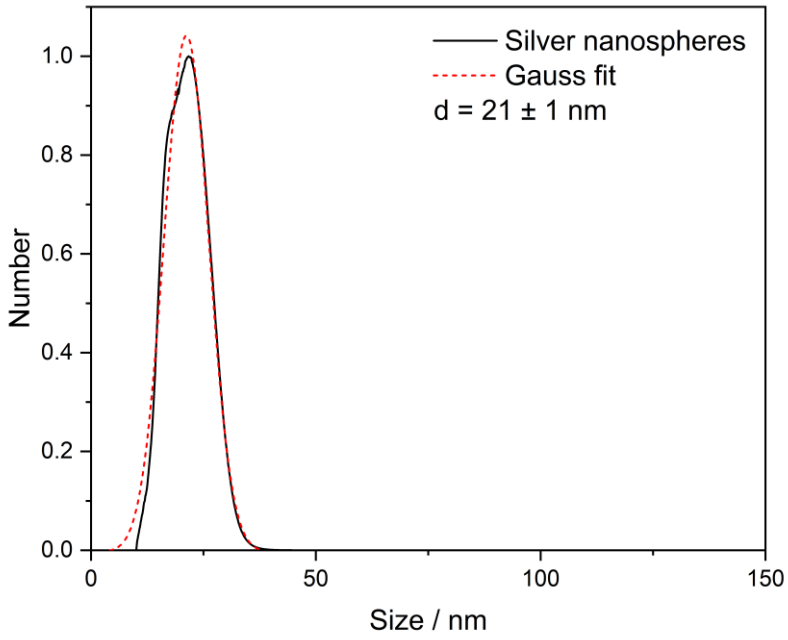

Figure 18. Particle size distribution, determined by DCS measurement of silver nanoparticles obtained from the reduction of $AgNO_3$ with glucose.

The average particle size obtained from DSC was 21 ± 1 nm with a PDI of 0.3, indicating a monodisperse system, which agreed with the PDI provided by DLS measurements.

Table 5. Comparison of particle size distribution, standard deviation, and polydispersity index (PDI) obtained from Gauss-fits for all size-determination methods.

Method	SEM	DLS	DCS
Size / nm	33	81	21
Standard deviation / nm	3	1	1
PDI	0.10	0.23	0.29

Table 5 summarizes the results obtained from the different methods used to determine the size and PDI of the synthesized colloidal system. It is important to note that there is some inconsistency among the measurements obtained by the three methods, which can be attributed to their distinct measurement principles. SEM analysis provided information about the size of the metal core, as the polymer shell surrounding the particles is not visible. DCS employs the metal density to calculate the size of the particles, which differs from the real one leading to smaller values. In contrast, DLS delivers results about the hydrodynamic radius of the particles, leading to an overestimation of the average particle size.[159] Considering the limitations and underlying principles of the size determination methods, it can be concluded that the results obtained from these methods agree.

5.1.2 Characterization of palladium nanocubes

5.1.2.1 Characterization of palladium nanocubes (ca. 18 nm)

The optical properties of the obtained palladium were examined by ultraviolet-visible (UV-Vis) spectroscopy. Similar to silver and gold, palladium nanoparticles also exhibit surface plasmon resonance phenomena.[161, 162] However, the specific location of the plasmon resonance peak in palladium nanoparticles depends on their size and shape, typically falling within the visible to near-infrared region of the electromagnetic spectrum.[163]

Figure 19 shows the UV-Vis spectrum of the palladium nanoparticles, showing a maximum at 238 nm and a small shoulder at approximately 300 nm. The observation of absorption at shorter wavelengths, such as 238 nm, indicated that the palladium nanoparticles were possibly small in size. The additional signal around 300 nm, represented by a small shoulder in the spectrum, suggested the presence of other absorption or scattering phenomena in that region, caused possibly by the morphology.

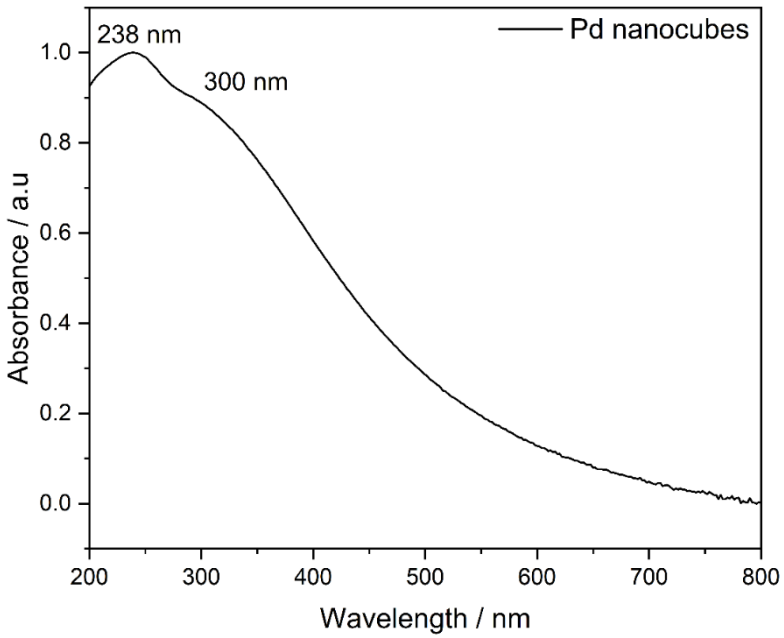

Figure 19. UV-Vis spectrum of the synthesized Pd nanocubes exhibiting two signals at shorter wavelengths.

Figure 20 shows two scanning transmission electron microscopy (STEM) images of the synthesized palladium nanoparticles. Upon initial observation (Fig. 20 A), the sample appeared to be unimodal and monodisperse, lacking any visible agglomerates. However, upon closer examination (Fig. 20 B), it became apparent that the sample consisted of not only nanocubes (aspect ratio 1:1) but also elongated faceted nanostructures with an aspect ratio 1:1.5, specifically cuboids or nanobars. The particles showed almost perfect sharp corners and edges. The composition of the sample was determined to be approximately 70% nanocubes and 30% nanobars. Both structures exhibited a normal size distribution, with the nanocubes having a mean edge length of 18 ± 1 nm and PDI 0.07 and the nanobars having a mean long edge length of 20 ± 1 nm (Fig. 20 C, D) and PDI 0.06.

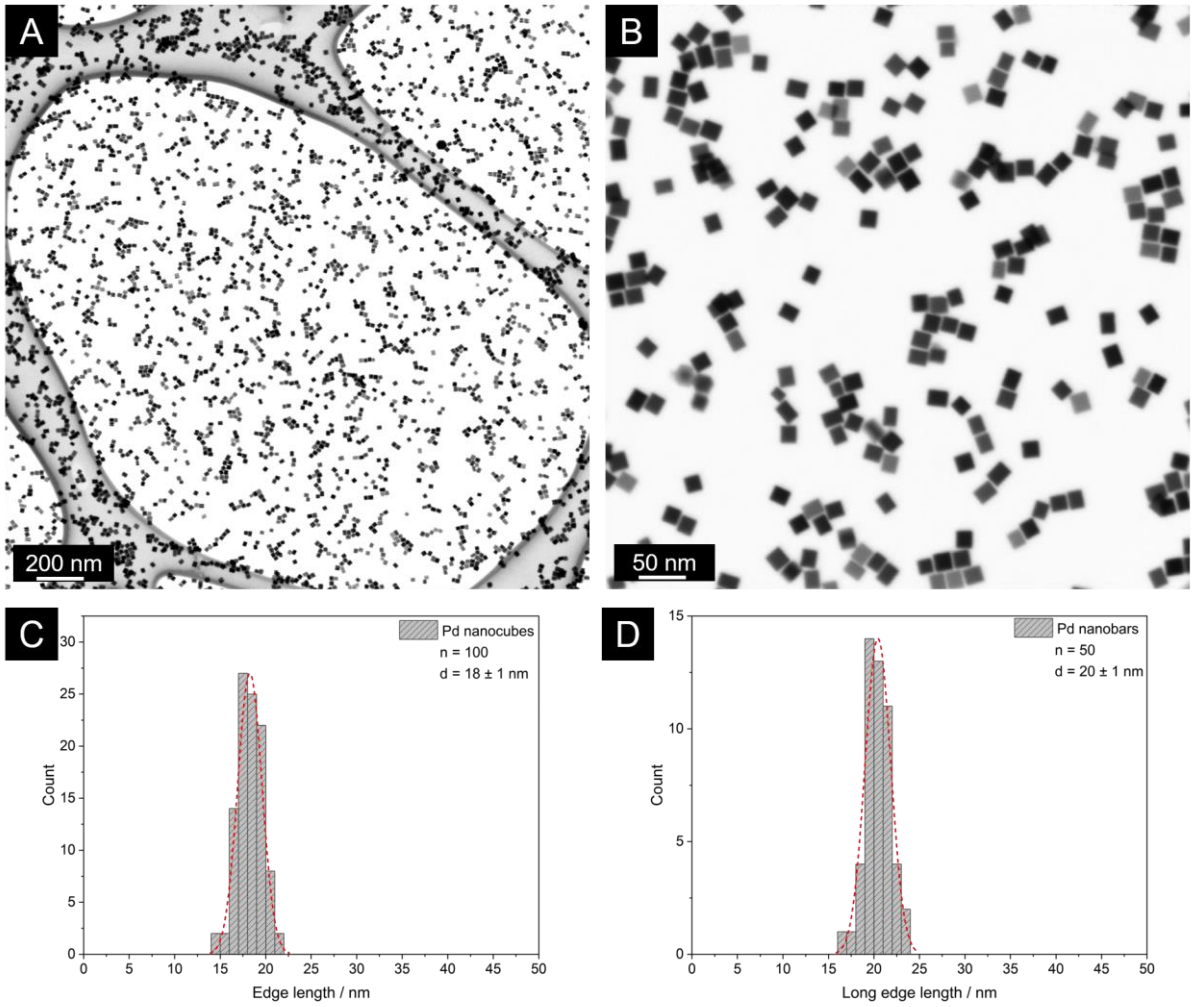

Figure 20. STEM images of the synthesized Pd nanocubes were both recorded with an accelerating voltage of 30 kV and magnifications of 100,000 (A) and 400,000 times(B). STEM size distribution of the nanocubes (C) and cuboids/nanobars (D).

Furthermore, energy dispersive X-ray spectroscopy was performed. In addition to the characteristic signals of palladium, a notable signal attributed to bromide was observed (Fig. 21). Interestingly, even after several washing cycles, the bromide signal was still detected, and remained relatively strong, suggesting that bromide ions were strongly bound to the surface of the palladium nanoparticles. Previous studies have reported that bromide ions can chemisorb on the surface of palladium nanoparticles, especially when present in high concentrations, explaining the persistent presence of bromide in the sample.[164-166]

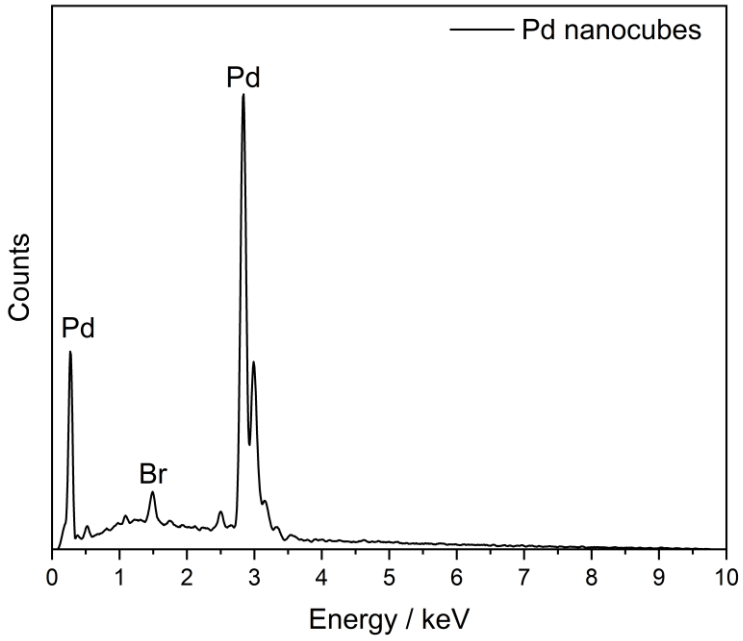

Figure 21. EDS spectrum obtained from the analysis of palladium nanoparticles.

Dynamic light scattering analysis was employed to assess the colloidal stability and size distribution of the synthesized palladium system. Despite the presence of two distinct morphologies within the sample, DLS measurements yielded a monodisperse particle size distribution with an average size of 35 ± 8 nm and a PDI of 0.29 (Fig. 22). This indicated a relatively narrow size distribution, considering that DLS measured the hydrodynamic diameter of the particles. The similarity in morphology and size of the nanoparticles likely contributed to the monomodal distribution observed.

To evaluate the colloidal stability of the dispersion, the ζ-potential was measured. The obtained value of -24 mV (pH=8) indicated a stable colloidal system. The negative ζ-potential could be attributed to the adsorption of Br^- anions onto the surface of the nanoparticles, as the capping agent PVP carries no charge.

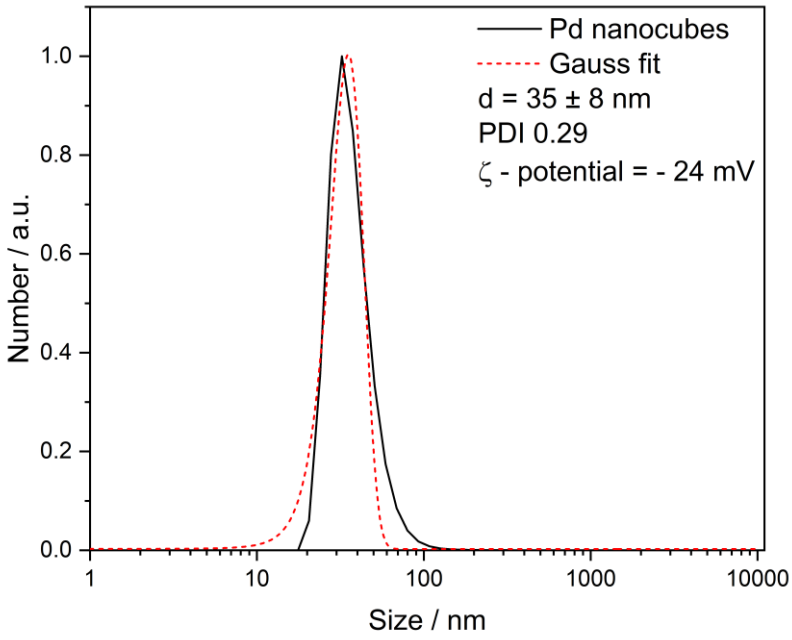

Figure 22. Particle size distribution was determined by DLS measurement of Pd nanoparticles obtained from the reduction of Na_2PdCl_4 with ascorbic acid.

Differential centrifugal sedimentation (DCS) analysis revealed a bimodal size distribution, indicating the presence of two distinct nanoparticle populations within the synthesized palladium system. Considering the knowledge of the two different structures present in the sample, the first peak in the size distribution was attributed to the nanocubes, while the second peak to the cuboids (Fig. 23).

The nanocubes (Peak 1) exhibited an average size of 17 nm with a standard deviation of 1 nm and PDI of 0.05, indicating a relatively narrow and homogeneous size distribution. On the other hand, the cuboids (Peak 2) displayed an average size of 21 nm with a standard deviation of 3 nm and a PDI of 0.14, suggesting a slightly broader size distribution compared to the nanocubes. These measurements obtained from DCS were consistent with the size information obtained from SEM.

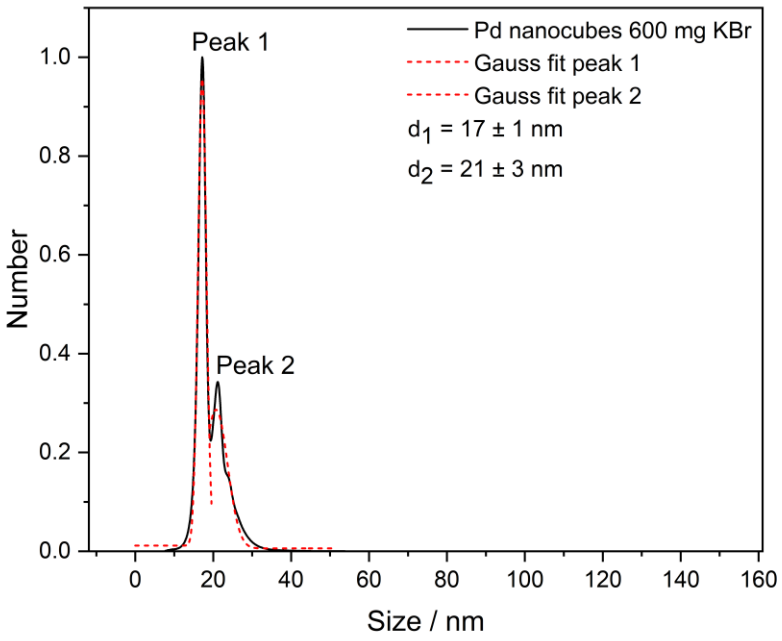

Figure 23. DCS bimodal size distribution obtained from the DCS measurement of Pd nanoparticles obtained from the reduction of Na_2PdCl_4 with ascorbic acid.

Transmission electron microscopy (TEM) images provided a more detailed understanding of the structure of the palladium nanoparticles synthesized. In the TEM image (Fig. 24 A), the presence of two distinct structures, namely cubes and cuboids/nanobars, were clearly visible in the sample. These structures exhibited different shapes and sizes, as discussed earlier.

In the TEM image shown in Figure 24 B, a single cuboid structure is presented. The corners of the cuboid appeared slightly rounded. The arrangement of atoms within the cuboid suggested the formation of a single crystal, with no evident crystal defects observed. This observation indicated a high level of structural integrity within the palladium nanoparticles.

Furthermore, a Fast Fourier Transform (FFT) analysis was performed (Fig. 24 C), which provided additional information about the crystallographic orientation of the nanoparticles. The FFT analysis confirmed the [001] orientation of the nanoparticles, which aligned with the quasi-cubic morphology observed in the TEM images.

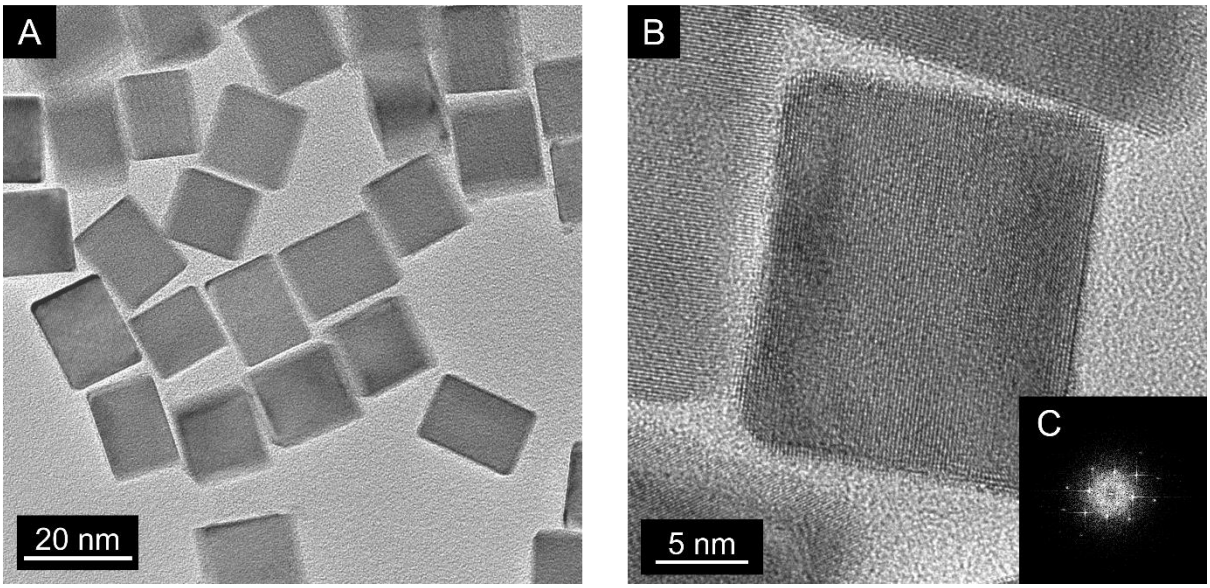

Figure 23. TEM images of Pd nanocubes/cuboids (A), a single cuboid in magnification (B), and the correspondent FFT analysis (C).

Powder X-ray diffraction (XRD) measurements were conducted to investigate the crystallinity and purity of the palladium nanoparticles. The obtained XRD pattern, as shown in Figure 25, displayed characteristic diffraction peaks that correspond to the fcc phase of elemental palladium. These diffraction peaks showed a very good agreement with the patterns for palladium nanoparticles reported in the literature.[167]

Rietveld analysis was performed on the XRD pattern to determine the lattice constant (*a*) of the palladium nanoparticles. The calculated lattice constant was found to be 3.8923 Å, which closely matches the literature value of 3.89019 Å[168] for the fcc phase of palladium.

Additionally, the crystallite size of the palladium nanoparticles was estimated from the XRD data. The calculated crystallite size was found to be 17 ± 1 nm, which was consistent with the particle size obtained from SEM observations. This correspondence further confirmed the monocrystalline nature of the nanoparticles, as observed in the TEM images.

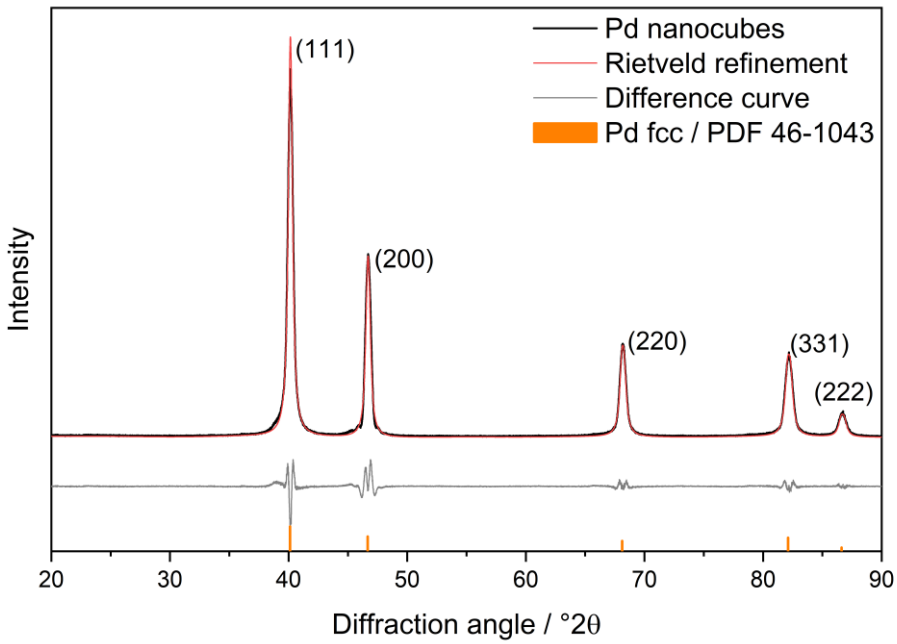

Figure 24. Rietveld-refined diffraction pattern of Pd nanocubes obtained from powder X-ray diffraction. Miller indices are given in parentheses.

Transmission electron microscopy, in combination with X-ray diffraction measurements, confirmed the synthesis of cubical single crystal palladium nanoparticles enclosed by (100) facets.

Table 6. Classification of the experimental reflexes of palladium nanocubes obtained from PXRD, based on the databank ICDD-PDF 43-1043.

Experimental reflex °2θ	Literature reflex °2θ	Lattice plane (hkl)
40.126	40.119	111
46.686	46.659	200
68.124	68.121	220
82.102	82.100	311
86.606	86.619	222

Table 7 summarizes the particle size distribution, standard deviation, and PDI obtained from scanning electron microscopy, dynamic light scattering, and differential centrifugal sedimentation.

Table 7. Comparison of particle size distribution, standard deviation, and polydispersity index (PDI) obtained from Gauss-fits for all size-determination methods.

Method	SEM		DLS	DCS	
	cubes	cuboids		cubes	cuboids
Size / nm	18	20	35	17	21
Standard deviation / nm	1	1	8	1	3
PDI	0.06	0.05	0.23	0.06	0.14

5.1.2.2 Influence of potassium bromide (KBr)

In the previously described synthesis, the addition of KBr served two important purposes. Firstly, the presence of Br^- anions has selectively modified the surface free energies of different facets on the palladium nanoparticles, particularly the (100) facets.[169] This selective chemical adsorption of bromide ions on the (100) facets could influence the growth and formation of nanocubes, which are favored by the strong binding of the capping agent PVP to these facets. By controlling the concentration of bromide, it could be possible to regulate the growth rate of different facets, [170] thereby allowinf control over the size of the nanoparticles. Secondly, bromide ions, in combination with oxygen, play a crucial role in the oxidative etching process (discussed in detail in chapter 5.2.2), which is necessary for the synthesis of well-defined faceted nanoparticles.

To investigate the impact of KBr, varying amounts (600, 450, 300, and 150 mg) were added to the reaction system while keeping all other reaction parameters constant. All samples were fully characterized by UV-Vis, STEM, DCS, and DLS. Several of the results presented below, derive from syntheses that were conducted by Mr. Sven Krämer as part of his bachelor's thesis in our group.

UV-Vis spectroscopy (Fig. 25) showed a consistent blue shift of the LSPR maxima of the Pd nanoparticles accompanied by a gradual weakening of the signals as the amounts of added KBr decreased. The shift of the peaks towards shorter wavelengths and the eventual absence of characteristic peaks suggested the formation of smaller palladium nanoparticles, potentially even smaller than 10nm,[163] as the concentration of the Br^- decreased significantly.

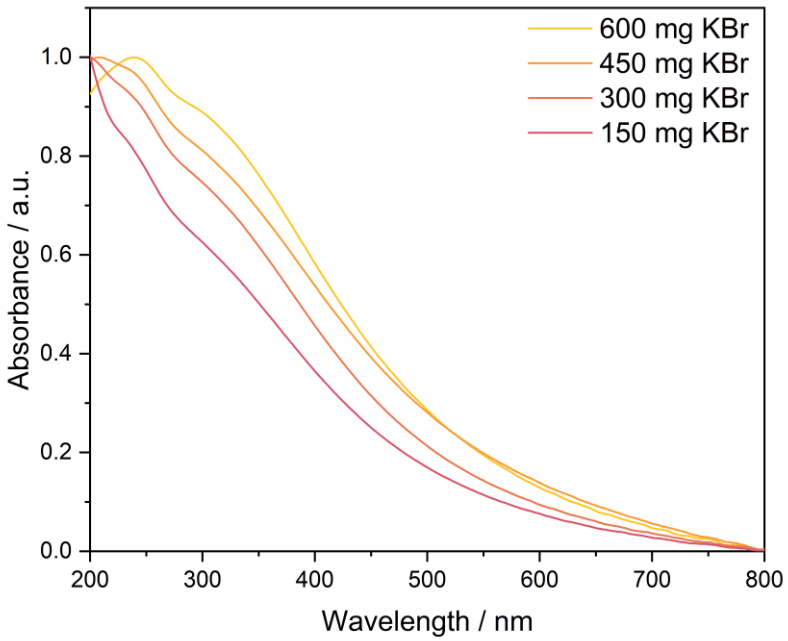

Figure 25. UV-Vis spectra obtained from the syntheses of Pd nanoparticles carried out with different amounts of KBr.

Figure 26 displays scanning transmission electron microscopy (STEM) images of the four different syntheses, along with their corresponding particle size distributions. Despite the variations in size and morphology, both nanocubes and nanobars were still present and distinguishable. However, it was evident that their sizes decreased as the amount of KBr decreased, which aligned with the observations from the UV-Vis spectroscopy analysis.

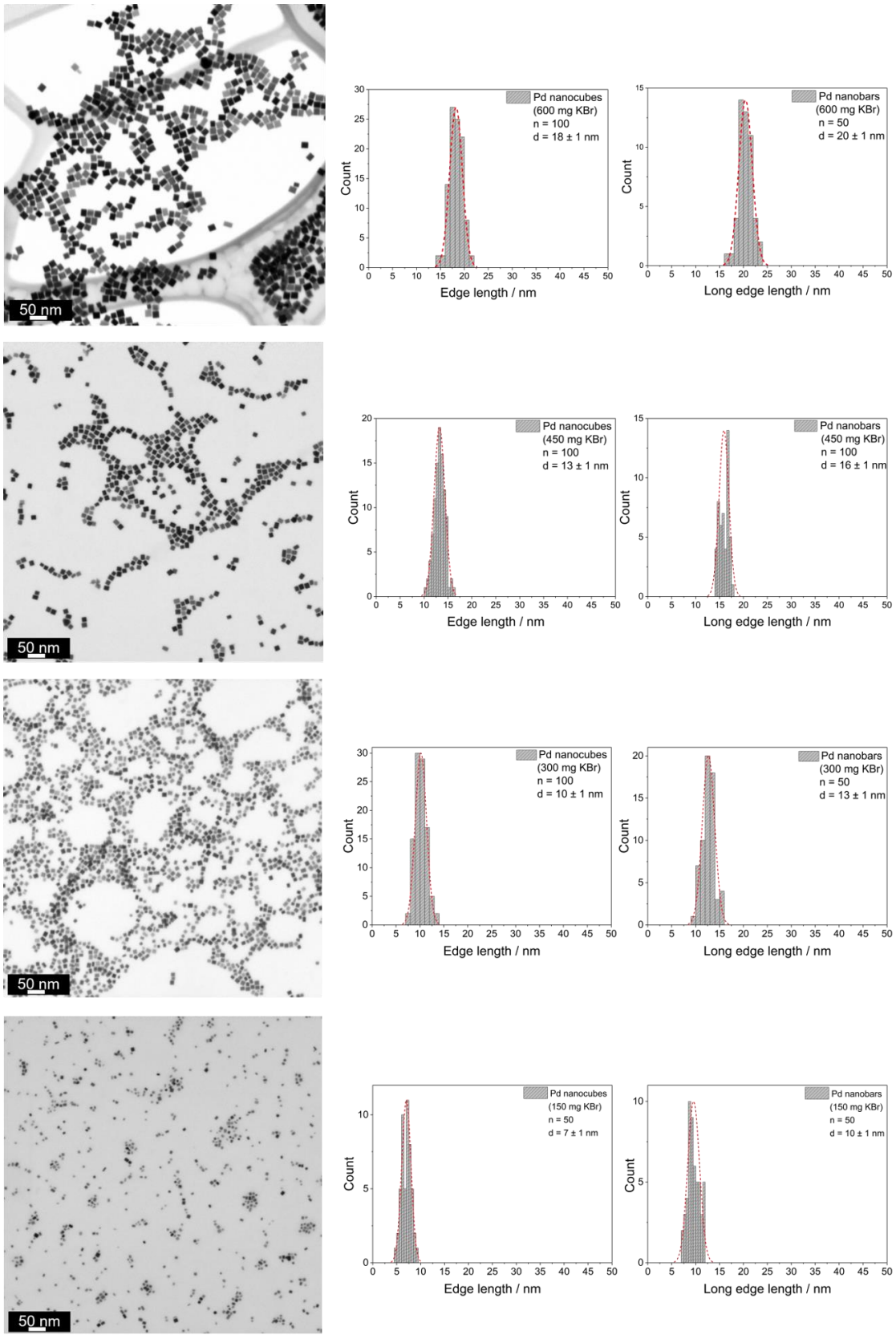

Figure 26. STEM images obtained from the syntheses carried out with different amounts of KBr (from the top: 600, 450, 300, 150 mg). All images were recorded with an acceleration voltage of 30 kV and a magnification of 300,000 times.

The particle size distributions obtained from DCS measurements, as shown in Figure 27 and more detailed in Appendix 9.2.1, also demonstrated a continuous decrease in the size of the Pd nanoparticles with decreasing amounts of KBr. Remarkably, when the particle size reached values below 13 nm, DCS measurements were no longer able to distinguish between the two different structures, resulting in a single peak instead of two distinct peaks, as observed previously. This suggested that at smaller sizes, the differences in morphology became less distinguishable by DCS analysis.

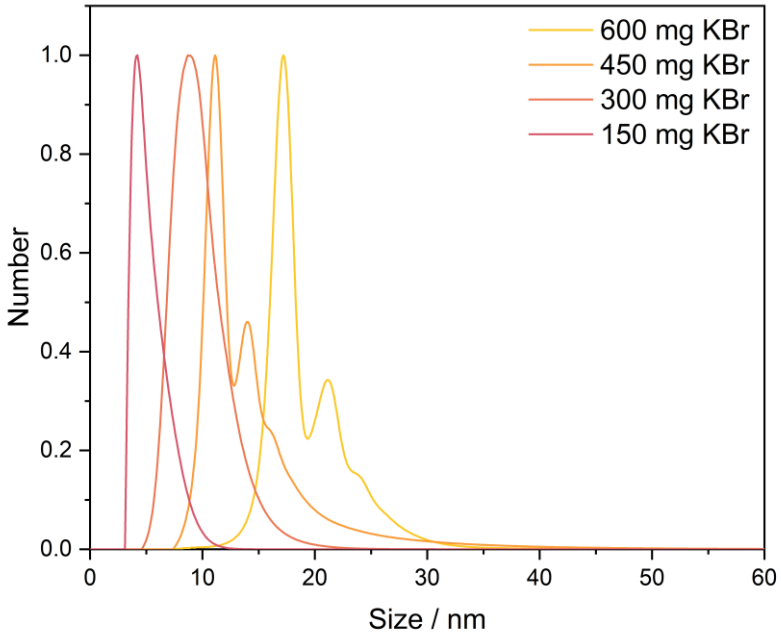

Figure 27. Comparison of DCS measurements of palladium nanoparticles synthesized by varying the amount of KBr.

All particle size distributions obtained from dynamic light scattering analysis displayed a monomodal size distribution, as expected (Appendix 9.2.2). Since the DLS software assumes spherical nanoparticles and measures the hydrodynamic radius,[159] it is typical to observe a single peak and a larger average size of the particles. However, it was notable that the measurements also indicated a decrease in size when a smaller amount of KBr was used in the synthesis (Fig.28), indicating the strong influence of Br^- ions on the particle size, even within the limitations of DLS analysis.

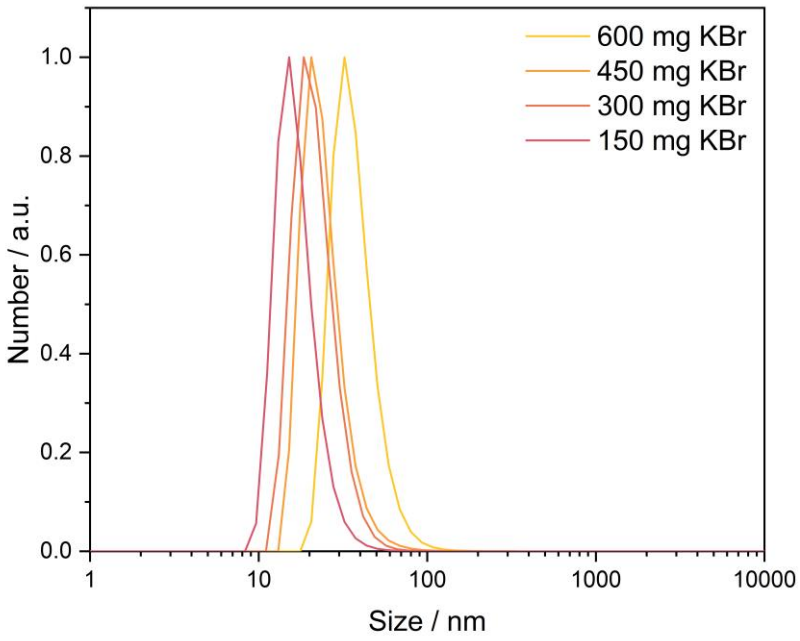

Figure 28. Comparison of DLS measurements of palladium nanoparticles synthesized by varying the amount of KBr.

The ζ-potential measurements, measured in pH=5, showed a decreasing trend (Table 8) as the KBr amount decreased. This decrease in ζ-potential can be attributed to the reduced concentration of Br^- adsorbed on the surface of the nanoparticles. It led to a shift from electrosteric stabilization to steric stabilization. However, this change in the stabilization mechanism did not indicate an unstable colloidal system. Instead, it enhanced the role of the stabilizing agent (PVP) as the bromide concentration varied.

Table 8. Particle size was determined through STEM, DCS, DLS, and ζ-potential (pH=5) of palladium nanoparticles synthesized with different amounts of KBr.

Method	**STEM**		**DCS**		**DLS**	**ζ-potential**
KBr mg	**cubes nm**	**cuboids nm**	**cubes nm**	**cuboids nm**	**nm**	**mV**
600	18 ± 1	20 ± 1	17 ± 1	21 ± 1	35 ± 8	-33
450	13 ± 1	16 ± 1	11 ± 1	14 ± 1	23 ± 5	-12
300	10 ± 1	13 ± 1	9 ± 2		21 ± 5	-12
150	7 ± 1	10 ± 1	5 ± 1		16 ± 4	-7

In summary, the variation of KBr amount in the synthesis of palladium faceted nanoparticles had a direct impact on the size of the nanoparticles while preserving their morphology. Decreasing the amount of KBr resulted in smaller nanoparticles, while the ratio between nanocubes and nanobars/cuboids (70%:30%) remained consistent. This size decrease trend was observed consistently across different measurement techniques, including UV-Vis spectroscopy, STEM imaging (Fig. 28 A), and size distribution analysis using DLS (Fig. 28 C) and DCS (Fig. 28 B).

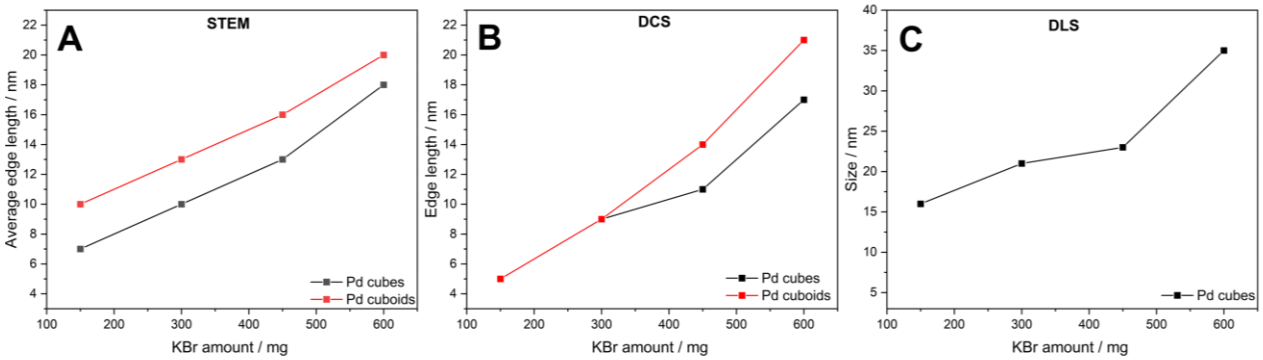

Figure 29. KBr mass-dependent diagram of the palladium average particle size, determined through STEM (A), DCS (B), and DLS (C).

5.1.2.3 Influence of capping agent polyvinylpyrrolidone (PVP)

To explore the influence of different polymer lengths on the size and morphology of Pd nanocubes nanoparticles, two additional variations of the synthesis were carried out using PVP_{40} (M_w = 40,000 g mol^{-1}) and PVP_{29} (M_w = 29,000 g mol^{-1}) alongside the previously used PVP_{55} (M_w = 55,000 g mol^{-1}).

UV-Vis spectroscopy (Fig. 30) showed a light red-shift in the LSPR peaks when PVP with fewer repeat units (PVP_{40} and PVP_{29}) were used compared to the synthesis with PVP_{55}. Interestingly, both polymer lengths showed similar red-shifts, suggesting the formation of larger nanoparticles.

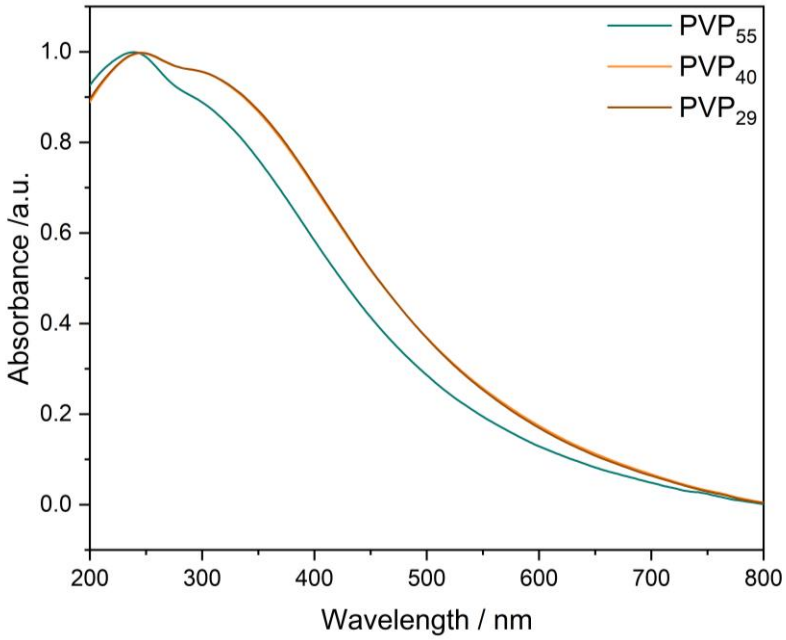

Figure 29. UV-Vis spectra obtained from the syntheses of Pd nanoparticles carried out with different lengths of polymer PVP.

Scanning transmission electron microscopy images (Fig. 32) provided further confirmation of the formation of larger nanoparticles, with the two structures (nanocubes and nanobars/cuboids) remaining consistent and their size increasing. Surprisingly, there was not a significant difference in size between the nanoparticles synthesized with PVP_{40} and PVP_{29}. Moreover, both PVP_{40} and PVP_{29} syntheses exhibited additional larger hexagonal nanoparticles, pyramids, and rods (Fig. 31) with an approximate size of 45 nm. This observation suggested that the oxidative etching process might be incomplete when using PVP_{40} and PVP_{29}, indicating a possible effect between the capping agent PVP_{55} and KBr in the formation of nanocubes and nanobars.

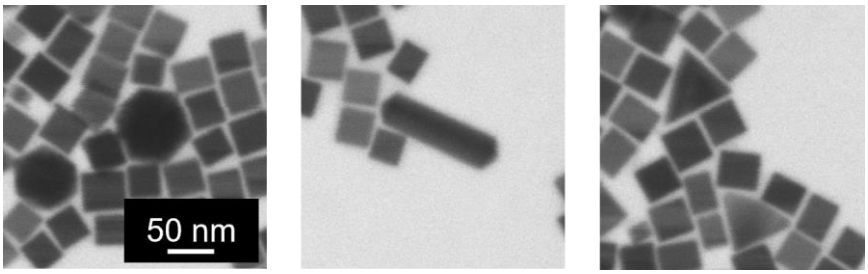

Figure 31. Additional morphologies (hexagons, nanorods, and pyramids) obtained from the synthesis of Pd nanoparticles with different polymeric chains of PVP. For all images, the scale is 50 nm.

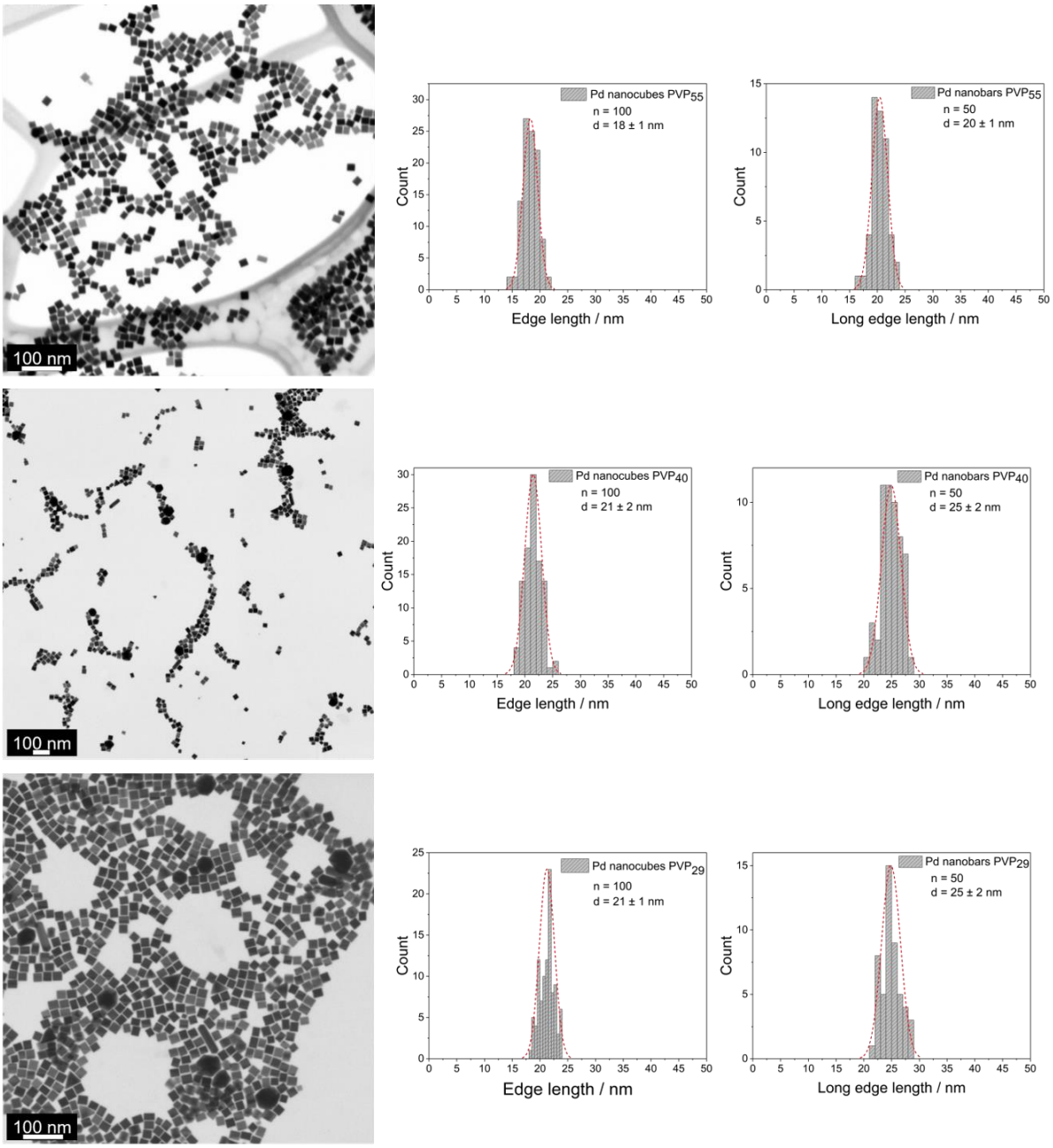

Figure 32. STEM images obtained from the Pd nanoparticle syntheses, carried out with different lengths of PVP (from the top: PVP_{55}, PVP_{40}, PVP_{29}) and the correspondent STEM size distributions for the nanocubes and nanobars. All images were recorded with an acceleration voltage of 30 kV.

The particle size distributions obtained from differential centrifugal sedimentation (Fig. 33) further supported the previous observations, revealing bimodal size distributions with each peak corresponding to the two different structures (nanocubes and nanobars/cuboids). When shorter polymers were used, the nanoparticles exhibited slightly larger sizes (Table 9) compared to the ones obtained with PVP_{55}.

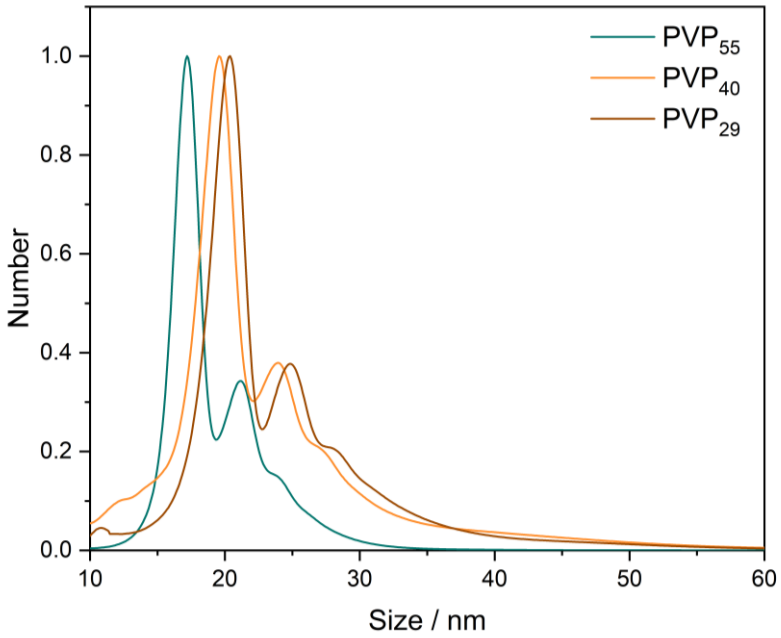

Figure 33. Comparison of DCS measurements of palladium nanoparticles synthesized with different polymeric chains of PVP.

Contrasting the bimodal distribution obtained from DCS, dynamic light scattering measurements (Appendix 9.2.2) consistently provided monomodal particle distributions, as observed before. Despite this difference in the distribution shapes, DLS also demonstrated no significant change in the particle size as the polymer length decreased (Fig. 34).

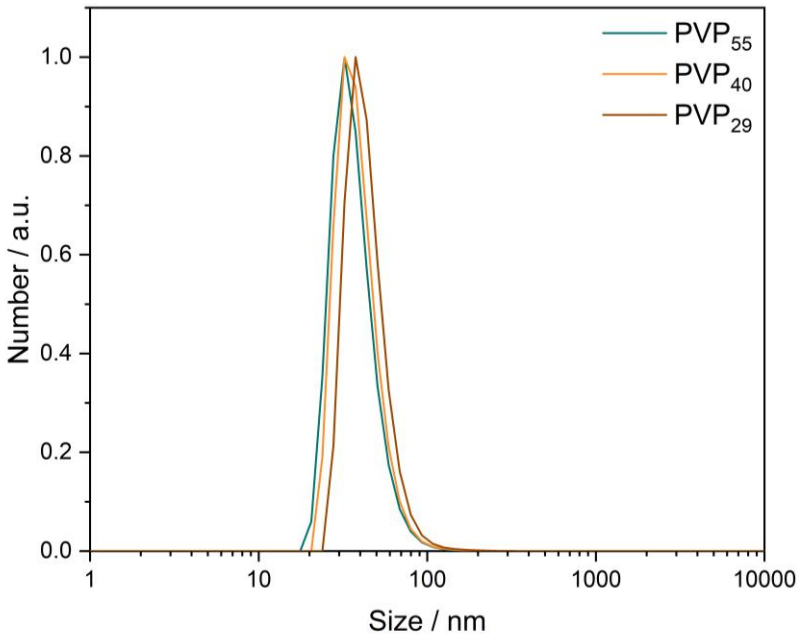

Figure 34. Particle size distributions obtained from the Pd nanocubes syntheses with different lengths of PVP.

The ζ-potential values obtained from each synthesis were consistently similar, as demonstrated in Table 9. These results indicated that the length of the polymeric chain (PVP) did not have an impact on the stabilization of the nanoparticles. The strong negative values, approximately -30 mV, suggested that all synthesized nanoparticles were colloidally stable systems, irrespective of the specific polymer length used in the synthesis.

Table 9. Particle size determined through STEM, DCS, DLS, and ζ-potential of palladium nanoparticles synthesized with different lengths of PVP.

Method	**STEM**		**DCS**		**DLS**	**ζ-potential**
PVP	**cubes nm**	**cuboids nm**	**cubes nm**	**cuboids nm**	**nm**	**mV**
PVP55	18 ± 1	20 ± 1	17 ± 1	21 ± 1	35 ± 8	-33
PVP40	21 ± 2	25 ± 2	19 ± 1	24 ± 1	37 ± 8	-33
PVP29	21 ± 1	25 ± 2	20 ± 1	25 ± 1	42 ± 9	-32

In summary, the use of different PVP variations in the synthesis of palladium nanoparticles did not affect the size of the nanoparticles, but it did impact the polydispersity of the system. Additional morphologies, like hexagons, nanorods, quasi-spherical particles, and pyramids, were also observed when shorter PVP polymers were used.

5.1.3 Characterization of palladium nanocubes (ca. 45 nm)

A seed-and-growth method was employed to generate large palladium nanoparticles with a cubical morphology, utilizing palladium nanoparticles obtained from the previous synthesis as seeds.

The optical properties of the nanoparticles were investigated using UV-Vis spectroscopy. The obtained UV-Vis spectrum (Fig. 35) exhibited a single peak at 360 nm which indicated the formation of nanoparticles with a size of approximately 50 nm.[163] The peak corresponding to the smaller palladium nanoparticles at 238 nm experienced a red-shift as a direct consequence of the enlargement of the nanoparticles, agreeing with similar observations in the literature.[167]

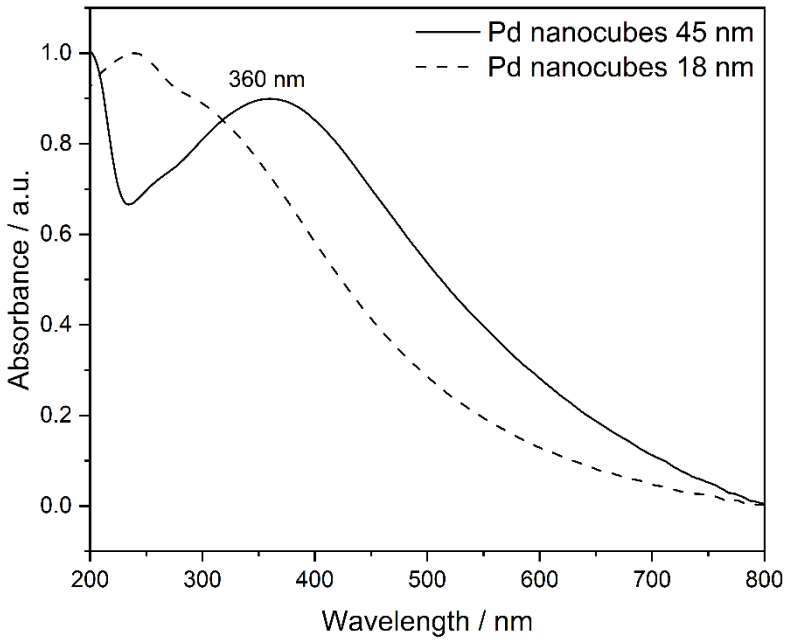

Figure 35. UV-Vis spectra obtained from the seed-and-growth synthesis of Pd nanocubes (45 nm) and 18 nm Pd nanocubes (seeds).

Scanning electron microscopy was employed to visualize the metal core of the palladium nanoparticles. The nanoparticles showed well-defined cubic structures with even surface. No smaller structures or agglomerates were visible, indicating a monodisperse system. The SEM images (Fig. 36 A and B) clearly depict a monodisperse sample consisting of larger palladium nanoparticles. Once again, the

presence of two distinct structures, namely nanocubes and nanocuboids/nanobars (yellow arrows, Fig. 36 B), was evident, maintaining a consistent ratio of 70% to 30%.

Analyzing the SEM size distribution for the nanocubes, it was found that the particles exhibited a mean edge length of 43 ± 3 nm and a low PDI of 0.07 (Fig. 36 C). On the other hand, the nanobars displayed a mean long edge length of 52 ± 4 nm (Fig. 36 D) with a PDI of 0.08.

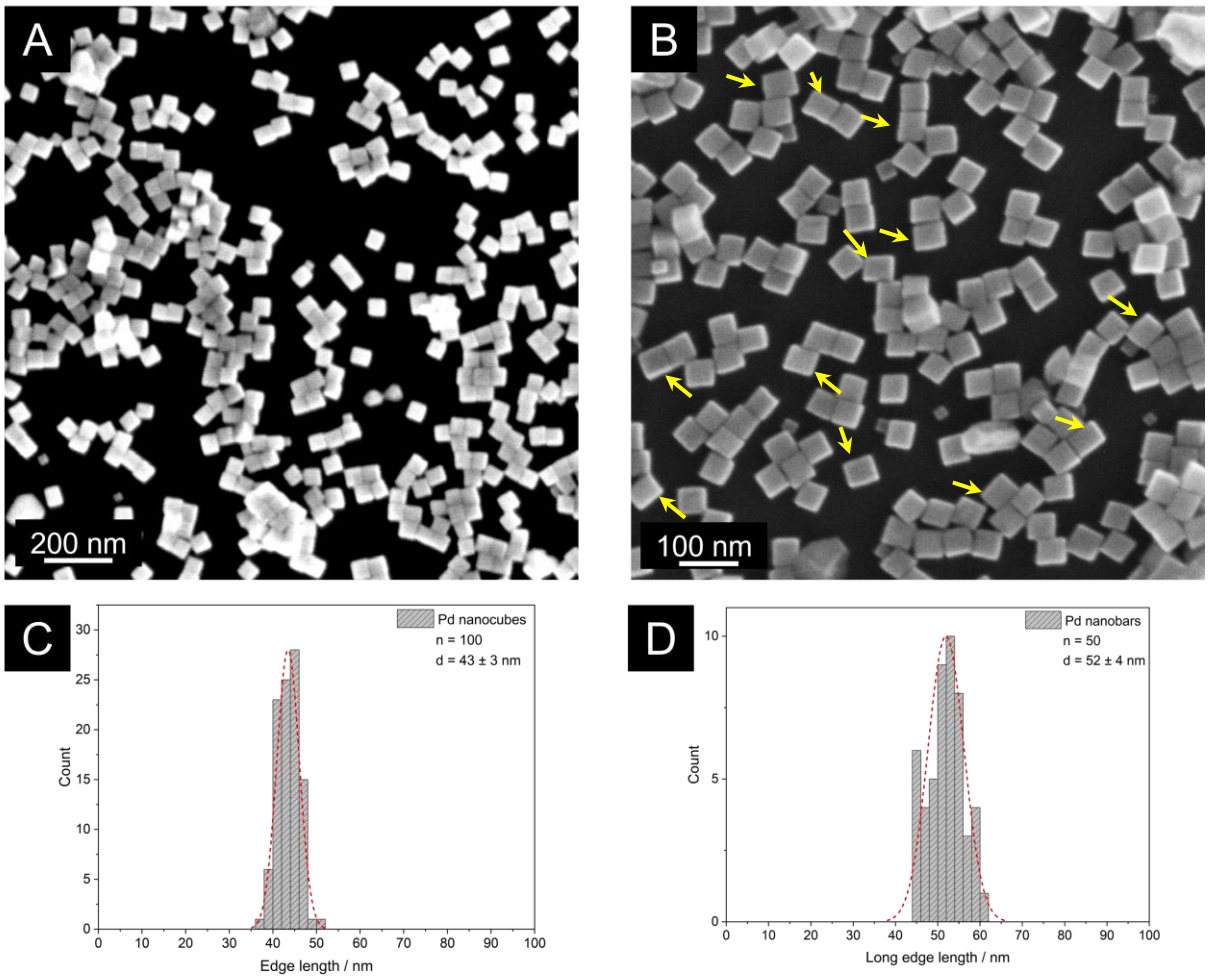

Figure 36. REM images of the synthesized Pd nanocubes both recorded with an accelerating voltage of 5 kV and magnification of 100,000 (A) and 10 kV and magnification of 200,000 times (B). SEM size distribution of the nanocubes (C) and cuboids/nanobars (D).

Dynamic light scattering was utilized to assess the colloidal stability of the nanoparticles. The mean hydrodynamic diameter obtained from DLS analysis revealed a size of 46 nm ± 5 nm (Fig. 37), indicating a monodisperse system without the presence of any agglomerates. The PDI value of 0.2 further confirmed the uniformity of the particle sizes within the dispersion. Furthermore, a negative ζ-potential value of -32 mV was observed, demonstrating the colloidal stability of the nanoparticle dispersion.

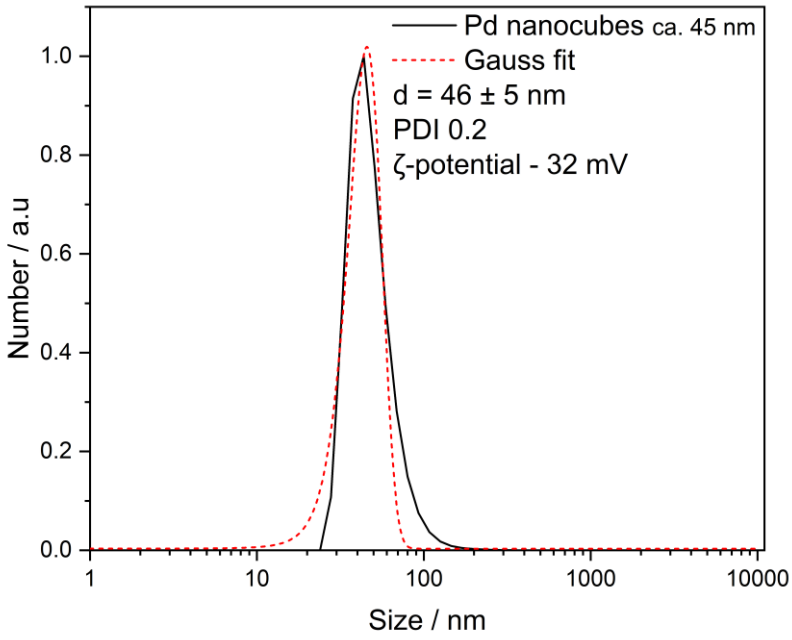

Figure 37. Particle size distribution was determined by DLS of Pd nanoparticles (seed-and-growth) obtained from the reduction of Na_2PdCl_4 with ascorbic acid.

As also observed on smaller Pd nanoparticles, discussed earlier, DCS analysis in this case also revealed a bimodal particle size distribution (Fig. 38). This finding suggests the presence of two distinct sizes of particles within the sample. The stronger peak observed in the DCS analysis can be attributed to the nanocubes, while the second peak corresponds to the cuboids/nanobars.

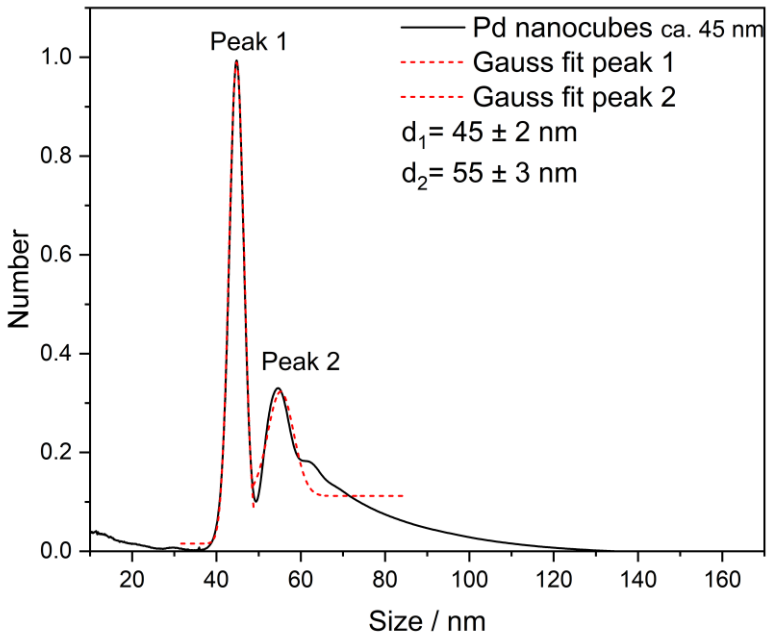

Figure 38. DCS bimodal size distribution obtained from the DCS measurement of Pd nanoparticles (seed-and-growth) obtained from the reduction of Na_2PdCl_4 with ascorbic acid.

Peak 1, associated with the cubes, exhibited an average particle size of 45 ± 2 nm, with a low polydispersity index (PDI) of 0.04. Peak 2, corresponding to the cuboids, displayed an average particle size of 55 ± 2 nm, also with a PDI of 0.04. These results matched the obtained SEM particle size distributions. Table 10 summarizes the values obtained from the methods utilized.

Table 10. Comparison of particle size distribution, standard deviation, and polydispersity index (PDI) obtained from Gauss-fits for all size-determination methods.

Method	**SEM**		**DLS**	**DCS**	
	cubes	**cuboids**		**cubes**	**cuboids**
Size / nm	43	52	46	45	55
Standard deviation / nm	3	4	5	2	3
PDI	0.07	0.08	0.20	0.04	0.05

The transmission electron microscopy images obtained provided further insight into the structure of the generated palladium nanoparticles. As seen in Figure 39 A, TEM confirmed the successful formation of larger palladium nanoparticles, exhibiting an average edge length of approximately 45 nm. Figure 39 B zooms in on a specific region of a particle, revealing the arrangement of palladium atoms within the nanoparticles. No defects or multiple crystallite domains were observed, indicating the preserved single crystalline nature of the initial 18 nm palladium nanoparticles, which were used as seeds.

Fast Fourier Transform analysis (Figure 39 C) demonstrated a high degree of crystallinity and a [001] orientation, providing additional confirmation of the cubical morphology. Although the growth of the palladium nanoparticles was epitaxial, it was not entirely uniform, resulting in nanocubes and nanobars with slightly irregular edges. However, despite this non-uniform growth, the nanoparticles maintained their cubical morphology.

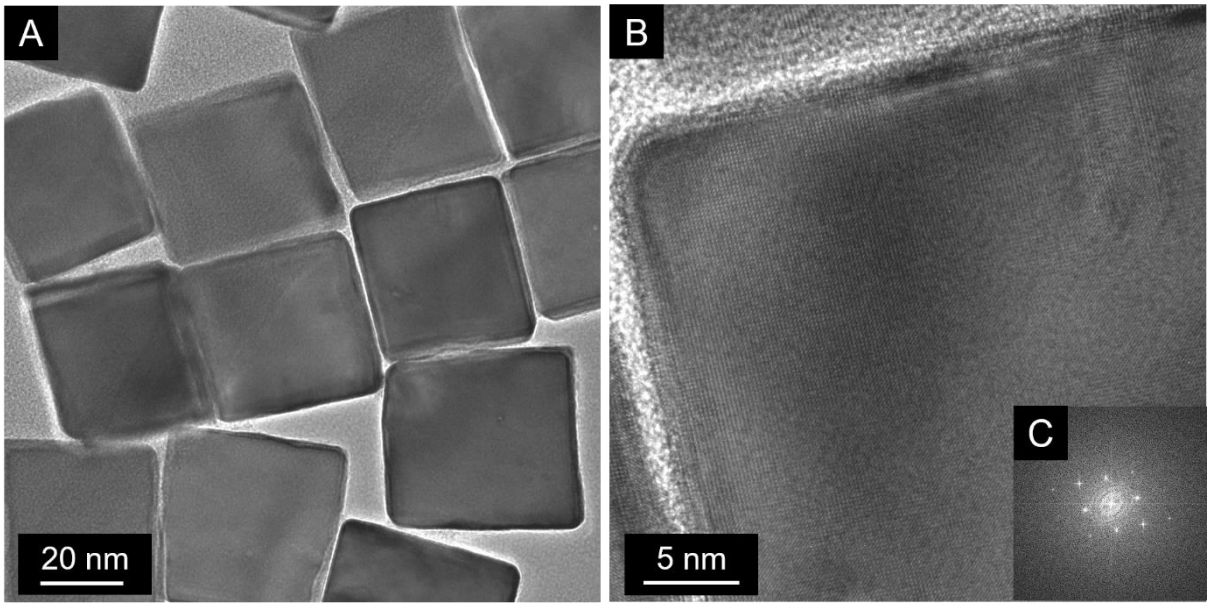

Figure 39. TEM images of Pd nanocubes/cuboids (A), a single nanoparticle in higher magnification (B), and the correspondent FFT analysis.

X-ray diffraction analysis (Fig. 39) provided confirmation of the crystallinity and purity of the larger palladium nanoparticles. The characteristic reflections corresponding to the elemental palladium face-centered cubic (fcc) phase were clearly detected, as detailed in Table 11. Compared to the diffraction pattern obtained for the 18 nm particles, the reflections observed for the larger nanoparticles were narrower and

sharper. This indicated an increase in crystallite size, corresponding to the larger particle size.

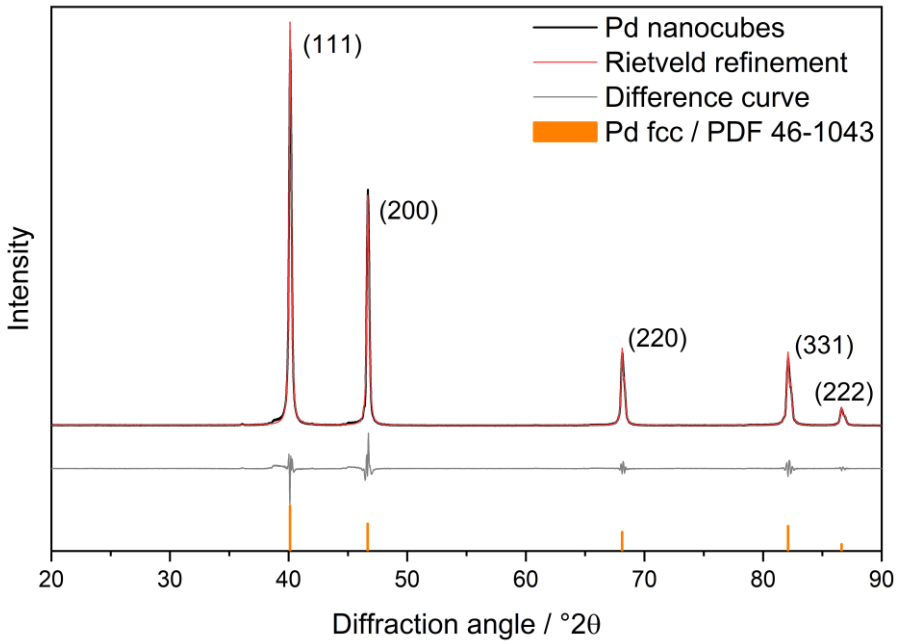

Figure 39. Rietveld-refined diffraction pattern of Pd nanocubes obtained from powder X-ray diffraction.

Rietveld refinement calculations yielded a crystallite size of 44 ± 1 nm, which aligned with the particle size determined from SEM and TEM analyses. This result further supported the notion that each palladium nanoparticle was a single crystal. After all, the seed-mediated growth approach was chosen in order to secure the single-crystalline nature of the larger Pd nanocubes. The lattice constant (*a*) was determined to be 3.8904 Å, which closely matches the theoretical value of 3.89019 Å. This agreement between the experimental and theoretical lattice constants provided additional evidence of the high crystalline quality and structural integrity of the palladium nanoparticles.

Table 11. Classification of the experimental reflexes of palladium nanocubes obtained from PXRD, based on the database ICDD-PDF 43-1043.

Obtained reflex °2θ	Literature reflex °2θ	Lattice plane (hkl)
40.116	40.119	111
46.666	46.659	200
68.134	68.121	220
82.112	82.100	311
86.617	86.619	222

5.1.3.1 Investigation of the growth mechanism of palladium nanocubes (45 nm)

To investigate the growth mechanism and changes in size and morphology during the synthesis of the 45 nm palladium nanocubes/nanobars with the seed-and-growth method, samples were collected every three hours and examined with UV-Vis, DLS, DCS and SEM.

The optical properties of the nanoparticles were examined using UV-Vis spectroscopy. The obtained spectra (Figure 40) revealed a gradual red-shift and broadening of the localized surface plasmon resonance (LSPR) peak at 238 nm, indicating an increase in the size of the nanoparticles over time. This observation suggested the ongoing growth and enlargement of the palladium nanoparticles during the synthesis process.[171, 172] According to the obtained UV-Vis spectra, the most significant red-shift of the LSPR peak occurred during the first 7 hours of the synthesis. After this point, no substantial changes were observed in the maximum position, indicating a relatively stable size of the palladium nanoparticles.

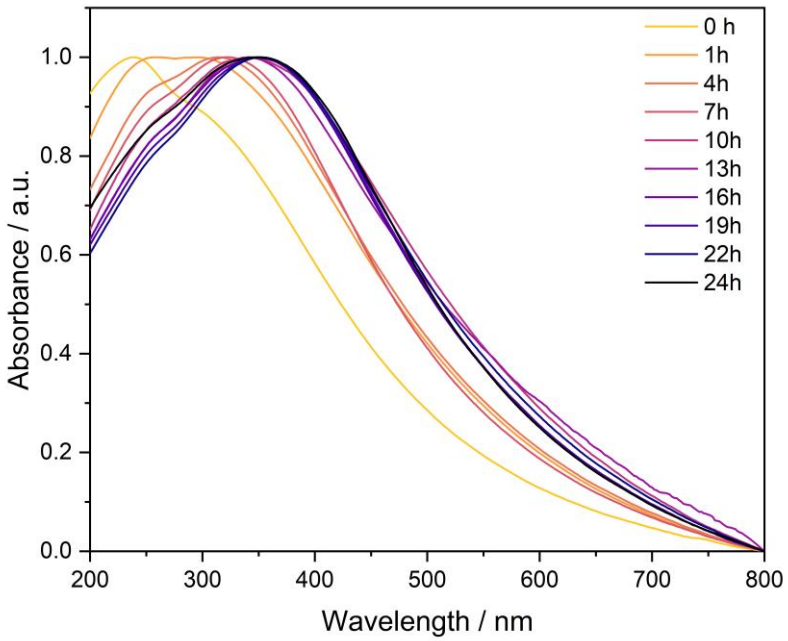

Figure 40. UV-Vis spectra of palladium nanoparticles obtained at different time intervals during the synthesis.

Scanning electron microscopy images were recorded for every sample during the 24 h synthesis (Figure 41). One hour after the initiation of the growth, the nanoparticles increased in size from 17 to 37 nm, but their morphology became irregular, deviating from the initial cubic shape. This deviation can be attributed to a non-uniform deposition of the atoms on the surface of the seeds. As the synthesis progressed, the average size of the particles reached 43 nm ± 3 nm, (4 h) forming cuboctahedral structures, indicating that during the growth procedure, the palladium atoms were not deposited equally on both (100) and (111) facets. Over time, the cuboctahedra transformed back gradually into cubic shapes and with sharper edges and corners. By the end of the reaction, the size of the particles did not change significantly; however, they exhibited well-defined structures with two distinct faceted morphologies, as previously discussed (nanocubes and nanobars).

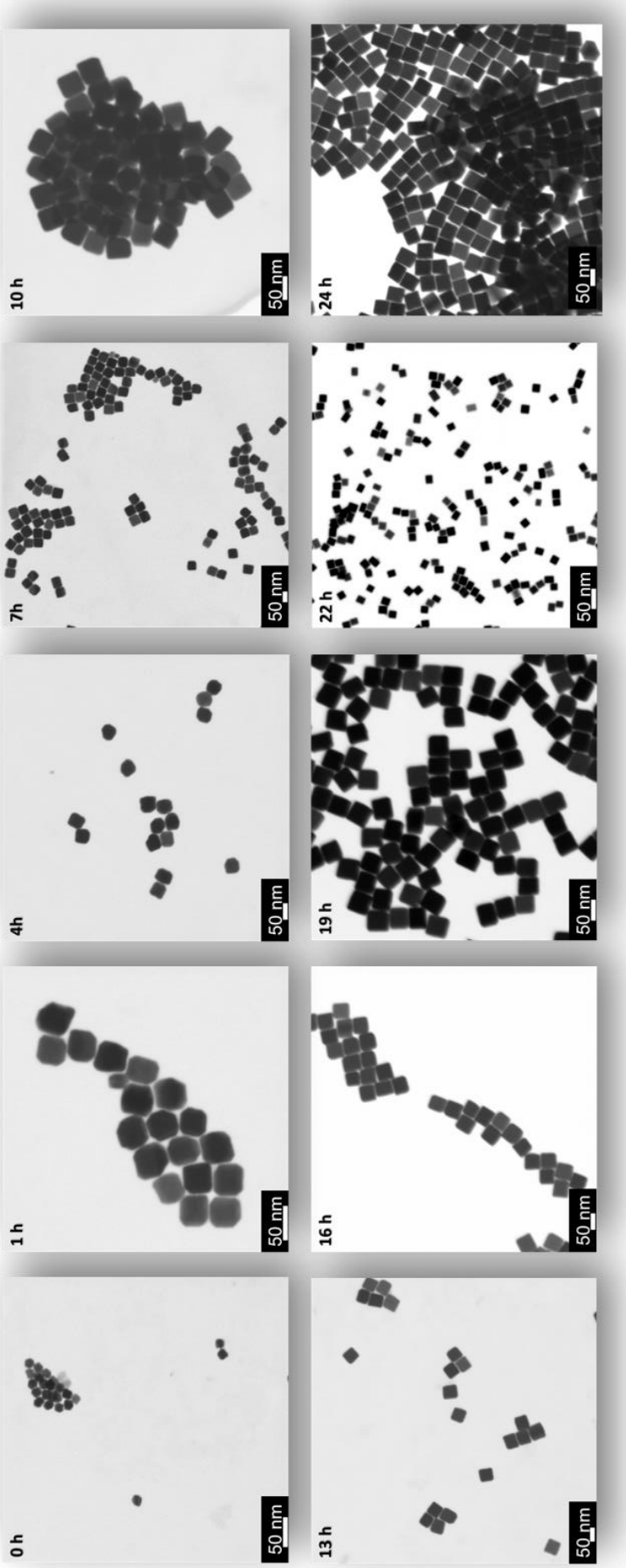

Figure 41. STEM images of samples taken before the reaction, after 1, 4, 7, 10, 13, 16, 19, 22 and 24 hours. All images were recorded with an accelerating voltage of 3 kV in different magnifications.

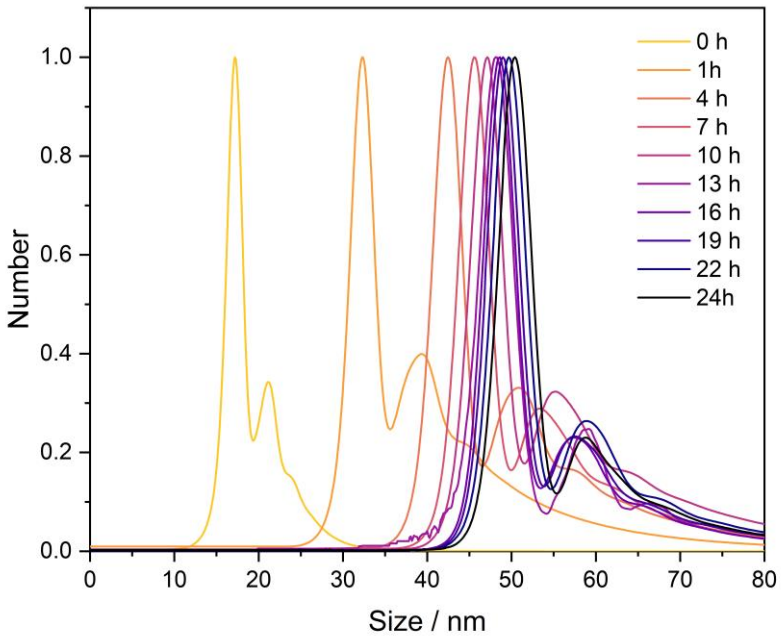

Figure 42. DCS measurements of palladium nanoparticles obtained at different time intervals during the synthesis.

The DSC measurements, as shown in Figure 42, have further supported the earlier findings from UV-Vis and STEM. The particle growth rate can be described as exponential, with a fast deposition of palladium atoms on the palladium seeds within the first 7 hours of synthesis, followed by a significantly slower growth rate in the time period between 7-24 hours. The growth was found to be consistent for both structures, showing a similar increasing trend within the sample, as depicted in Figure 43.

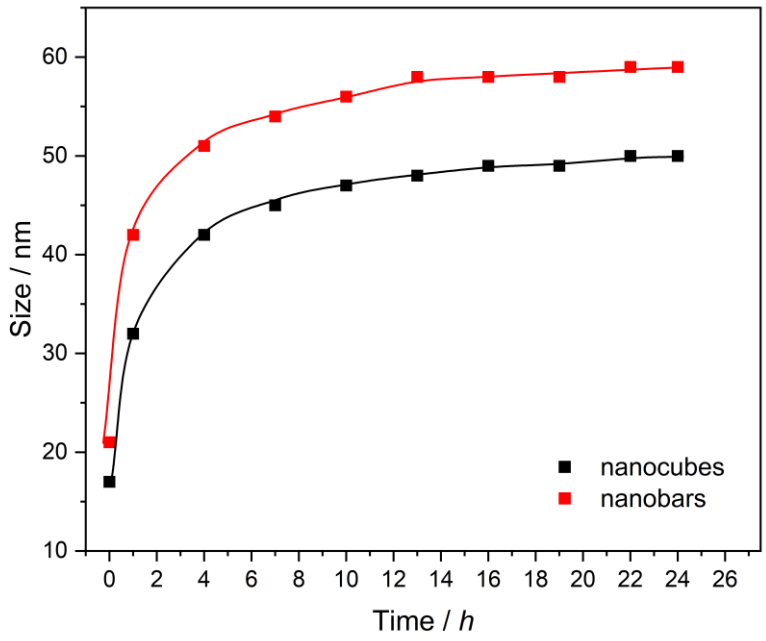

Figure 43. Time-dependent size diagram of palladium nanocubes and nanobars (45 nm). The size at each step was obtained from the corresponding DCS particle size distributions.

In brief, 18 nm palladium nanoparticles were used as seeds to generate larger 45 nm nanoparticles using a seed-and-growth approach. The larger nanoparticles remained monodisperse and single-crystalline, which was confirmed by DLS and XRD measurements. Analysis of samples collected at different time intervals revealed a fast growth rate in the first 7 hours of synthesis, but the deposition of palladium on the seeds was not epitaxial, leading to octahedral structures. The growth rate gradually decreased, and the nanoparticles regained their cubic shape, resulting in the final product after 24 hours.

5.2 Polyol-based syntheses of monometallic nanoparticles

5.2.1 Characterization of silver nanowires

The synthesis of silver nanowires typically involves the reduction of a metal salt in the presence of a stabilizing agent in a suitable solvent, such as water or ethylene glycol. Among the various methods known, such as electrochemical, hard-template, and soft-template methods, the polyol-based synthesis is suitable for producing anisotropic silver nanoparticles, offering more control over particle size and shape while delivering reproducible results with high product yields.[45] The method has proven effective in generating silver nanowires through a seed-and-growth approach, where heterogeneous nucleation occurs in the presence of suitable etching and capping agents that strongly influence the resulting morphology. Several metal nanoparticles have been used in the past as exotic species for nucleation, hence for the growth of silver nanowires, such as platinum nanoparticles, silver nanocubes and silver nanoparticles.[173, 174]

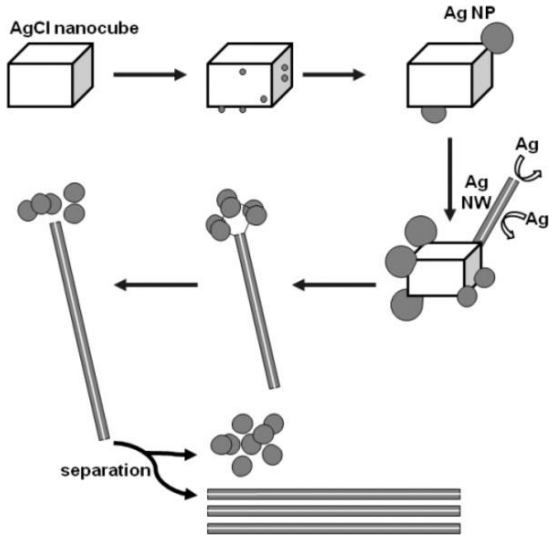

Figure 44. Schematic representation of the heterogeneous nucleation and growth process of silver nanowires. Adapted with permission. [175] Copyright 2014 American Chemical Society.

In this work, silver nanowires were synthesized after Schuette *et al.*[150]. In this method, silver chloride seeds are formed *in-situ* by adding silver nitrate and sodium chloride at the beginning of the synthesis. The slow injection of silver nitrate into the reaction mixture initiates the growth of five-fold twinned silver nanoparticles on the silver chloride particles, gradually growing into nanowires (Fig. 44).

The addition of polyvinylpyrrolidone, with 55,000 repeating units, plays a crucial role in the morphology of the resulting nanoparticles as it leads to the complexation of the (100) facets, allowing the particles to grow only in [110] direction as the silver ions inhibit the (111) facets.

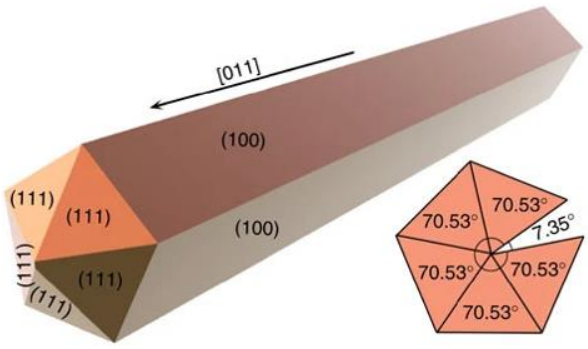

Figure 45. A 3D representation of a silver nanowire with a fivefold symmetry and its crystallographic planes. [176]

Due to their anisotropic morphology, silver nanowires present interesting optical properties. The UV-Vis spectrum showed two maxima at 348 nm and 379 nm, which can be attributed to the two energetically different surface plasmons (Fig. 46). The peak at 348 nm can be attributed to the longitudinal plasma band, i.e., the UV-Vis absorption going along the length direction, while the other at 379 nm to the transverse plasma band, i.e., the UV-Vis absorption going along the width direction.[177] The UV-Vis spectrum obtained from the synthesized nanowires matche´d those in the literature.[175, 177, 178]

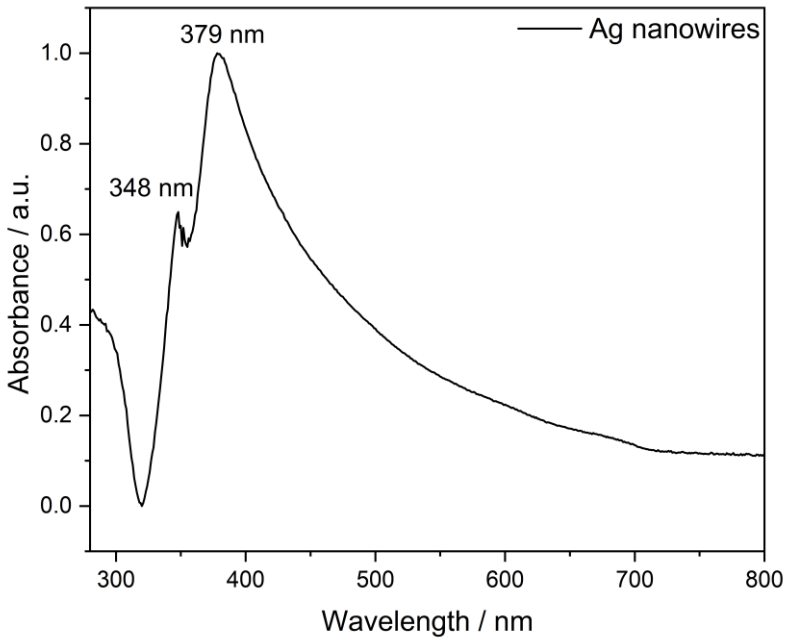

Figure 46. UV-Vis spectrum of the Ag nanowires obtained from the polyol process.

Figure 47 depicts SEM images of the synthesized silver nanowires. Most of them seemed to have a uniform width, with an average value of 74 ± 15 nm. Their length-to-width ratio appeared to be high as they showed a length of 15 µm. However, a few shorter and thicker morphologies, such as rods, could be seen. Furthermore, their previously discussed five-fold symmetry was visible.

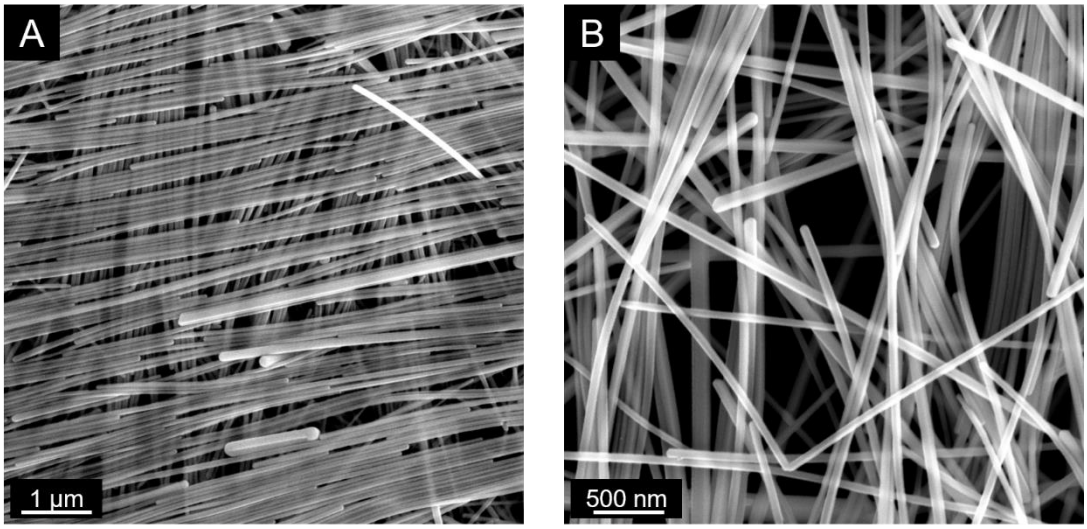

Figure 47. SEM images of silver nanowires obtained from the polyol process with a magnification of 25,000 (A) and 50,000 (B) were recorded with an accelerating voltage of 15 kV.

However, determining the hydrodynamic radius of silver nanowires by DLS could be problematic due to their anisotropic morphology. The synthesized nanowires were characterized by DLS. Figure 48 shows the size distribution obtained from the measurement. However, this characterization method exhibits limitations regarding this specific morphology. DLS provided a monomodal size distribution of silver nanowires with a mean length of 590 nm and a standard deviation of 14 nm, which did not agree with the measurements obtained from SEM. The PDI value of 0.27 showed a monodisperse system. Nevertheless, PDI was calculated based on the full width at half maximum of Gaussian peak fitting (see eq. 5, Chapter 3.2.1). In this case, it could not be considered as this method cannot deliver representative results about the size of the particles.

The strong negative ζ-potential, -39 mV, showed an electrosteric stable colloidal system. Even though the nanowires are stabilized with PVP, the negative value can be attributed to the negative Cl^- ions adsorbed on the surface of the wires, which derive from the NaCl added during the synthesis.

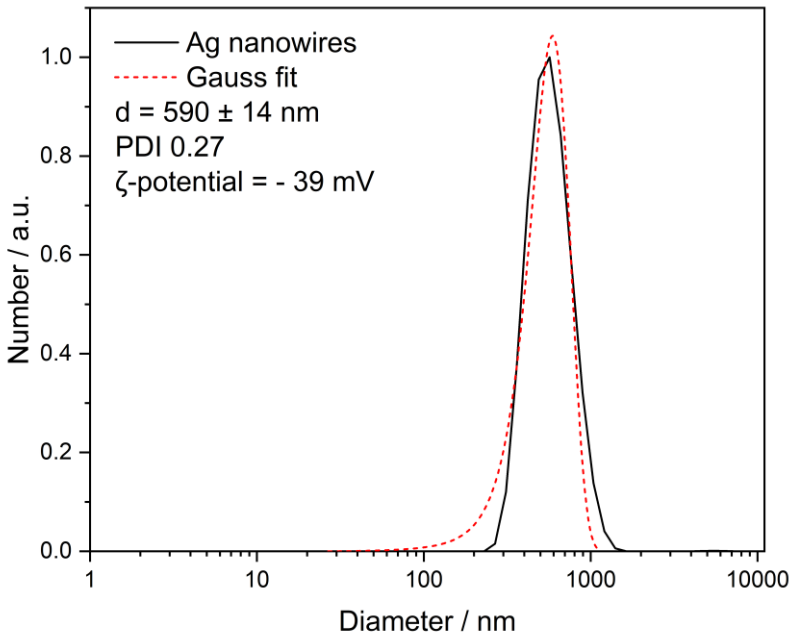

Figure 48. Particle size distribution (by number) determined by DLS measurement of silver nanowires.

The anisotropic morphology of silver nanowires and their long length were not only problematic for the DLS measurements. Obtaining the size distribution through DCS was also not possible. Their large size caused them to sediment quickly, making it impossible to get valuable data. Furthermore, the fast rotation of the disk might cause the nanowires breakage, which could result in misleading data.

To examine the phase purity and the crystallinity of the synthesized silver nanowires, powder X-ray diffraction was carried out. The position of the reflexes on the diffraction pattern (Fig. 49) agreed with the correspondent reflexes of the fcc silver phase (Table 12). No other reflexes were visible, confirming the absence of AgCl seeds generated during the synthesis and used as templates for the growth of silver nanowires.

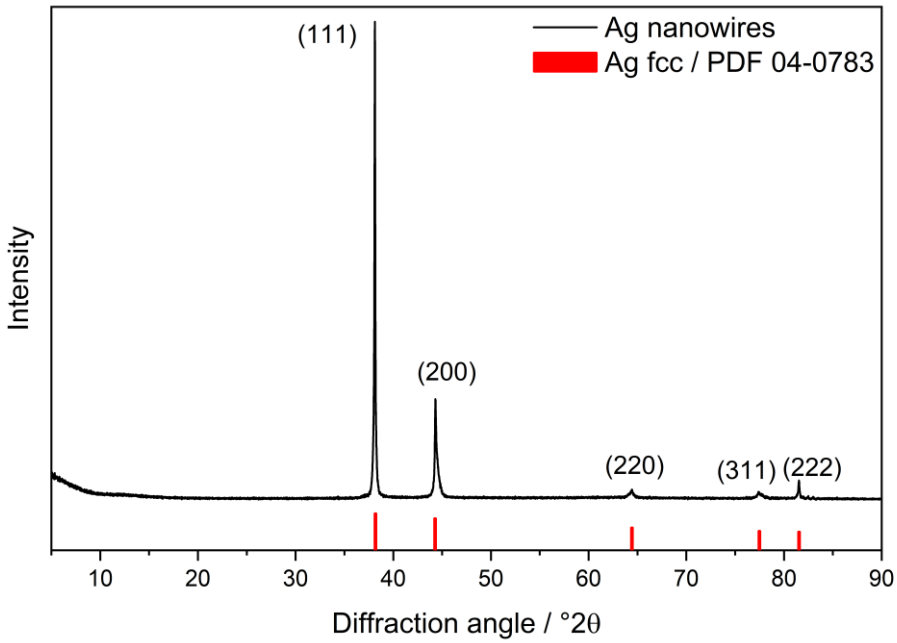

Figure 49. Diffraction pattern of the silver nanowires, obtained from powder X-ray diffraction. The Miller indices of the fcc silver peaks are indicated in parentheses.

Table 12. Classification of the experimental reflexes of silver nanowires obtained from PXRD, based on the database ICDD-PDF 04-0783.

Experimental reflex °2θ	Literature reflex °2θ	Lattice plane (hkl)
38.119	38.117	111
44.310	44.279	200
64.440	64.428	220
77.368	77.475	311
81.537	81.539	222

5.2.2 Characterization of silver nanocubes

The synthesis of silver nanocubes has been the subject of extensive research, particularly by Xia's group, over the last two decades.[149, 179-181] The generation of cubic silver nanostructures has posed significant challenges due to the limited knowledge about their growth mechanism, making it almost impossible to develop reproducible protocols.[181] Unlike thermodynamically stable (111)-faceted structures, nanocubes are enclosed by (100) facets, requiring precise kinetic control for their synthesis. After extensive research and experiments, silver nanocubes can be generated by the oxidative etching of twinned particles, which are unavoidably formed at the early stages of the synthesis. In this work, a modified polyol synthesis from Dr. Helmlinger[151] and Dr. Pappert,[152] first introduced by Xia's group, was used.[149]

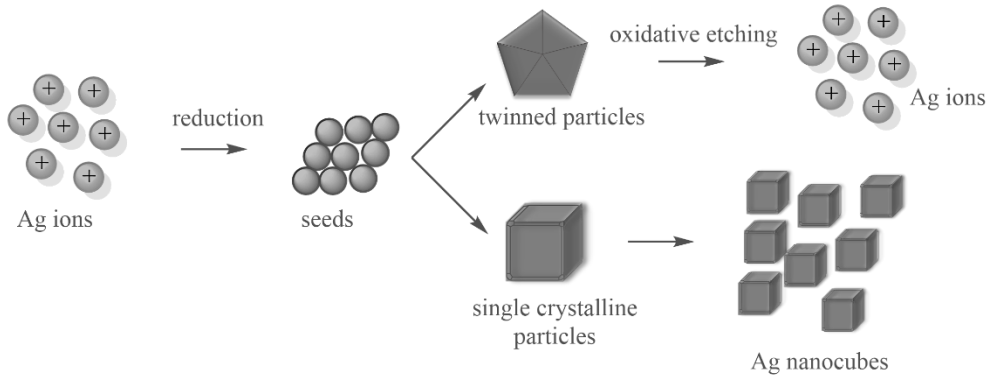

Figure 50. Proposed mechanism of the oxidative etching of the five-fold twinned particles during the silver nanocubes synthesis, proposed by Im *et al*.[149]

An essential step before the beginning of the actual reaction is heating ethylene glycol at 160 °C in an open reaction vessel for an hour. This heating step serves two essential purposes:

- allows any absorbed water by ethylene glycol to evaporate
- allows oxygen from the atmosphere to flow into the flask, which plays a crucial role in the subsequent etching step.

Another critical step in the reaction is preparing the silver nitrate solution. It is essential to prepare the solution exactly before adding it to the reaction mixture because even a slightly aged $AgNO_3$ solution can lead to the generation of silver nanowires.[182] In the case of adding aged $AgNO_3$ solution, the amount of HCl should be adjusted accordingly. After adding $AgNO_3$ to the solution, the reduction of silver starts, following

the reaction discussed in Chapter 4.4.2.1. As the concentration of silver atoms reaches a supersaturation level, nucleation occurs, and nanoparticles begin to grow. At this stage, two crystalline structures are generated: single-crystal and five-fold twinned. However, only the single-crystal structures can lead to the generation of silver nanocubes. In the meantime, during the synthesis, the H^+ cations produced after the reduction of the $AgNO_3$ and the free NO_3^- generate *in situ* HNO_3, initiating a backward reaction that selectively dissolves the twinned silver structures formed (eq. 13). The earlier addition of HCl also contributes H^+ to the reaction mixture, leading to the production of more HNO_3, which is gradually consumed. Subsequently, a second nucleation takes place, enhancing the formation of single-crystal nanostructures, i.e., nanocubes.[149]

$$4\ HNO_3 + 3\ Ag \rightarrow 3\ AgNO_3 + NO + 2\ H_2O \qquad (13)$$

The five-fold twinned decahedral particles are selectively dissolved during the oxidative etching, while single-crystal nanocubes remain intact. The twinned structures provide active sites for oxidative dissolution; hence they dissolve, and in turn, they release silver ions into the solution, which leads to the growth of the existing nanocubes.[183] The majority of nanoparticles obtained from this synthesis showed a cubic morphology.

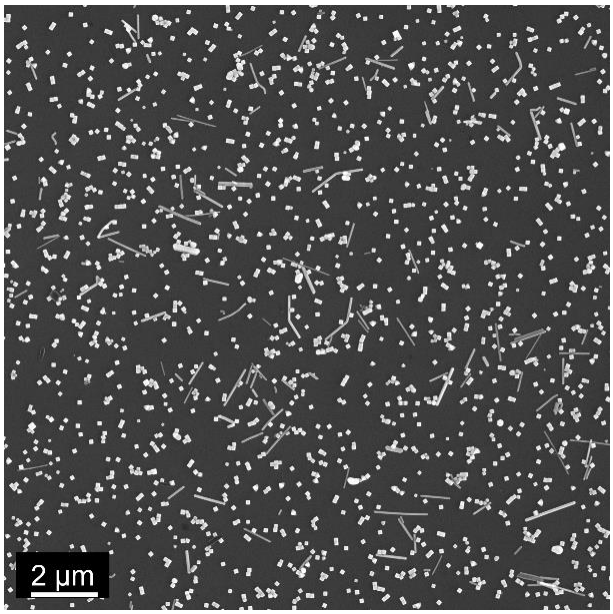

Figure 51. A mixture of silver nanocubes and nanowires from the described synthesis before the filtration in a magnification of 10,000 times. The image was recorded with an accelerating voltage of 15 kV. Both nanocubes and nanowires were observed.

Despite the careful control of all the parameters, the formation of some nanowires was inevitable (Fig. 51). To isolate the cubes, the resulting dispersion was filtered through a cellulose filter with a pore diameter of 0.45 µm. The nanowires are very long and cannot pass through the filter. Hence only the smaller particles remained in the dispersion after the filtration.

The optical properties of silver nanocubes have been extensively studied as they find applications in surface-enhanced Raman spectroscopy (SERS).[184-186] Silver nanocubes exhibit different optical properties from similarly-sized nanospheres due to their cubic shape. Their sharp corners and edges lead to additional plasmonic modes visible at different wavelengths in the spectrum.

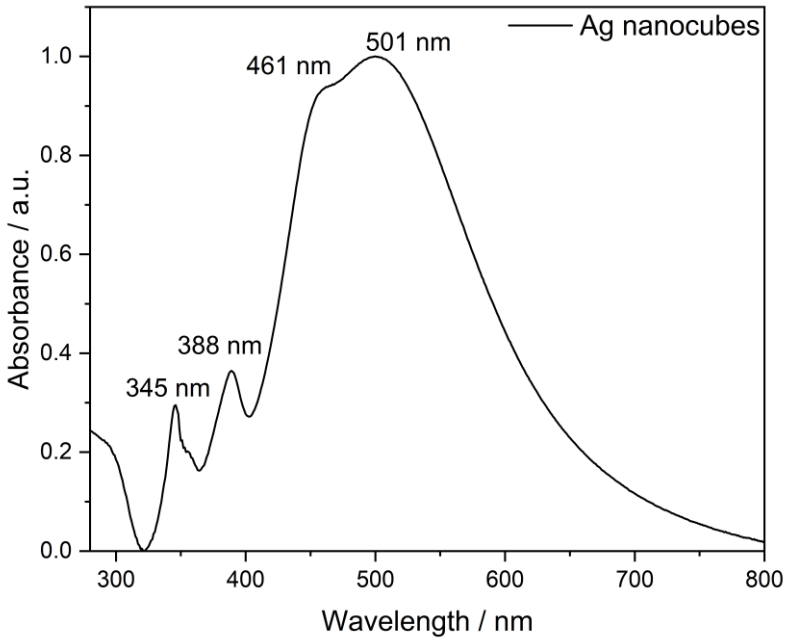

Figure 52. UV-Vis spectrum of the obtained silver nanocubes obtained from the polyol synthesis.

However, similarly to the nanospheres, their absorbance peaks depend also on their size, showing red-shift and broader peaks as their size increases. The obtained UV-Vis spectrum from the synthesized nanocubes showed two maxima at 388 nm and 501 nm and a small shoulder at 461 nm, indicating nanocubes with a mean edge length between 80 and 90 nm.[187, 188] The peak at 501 nm can be attributed to dipole resonance mode, and the small peak at 461 nm can be attributed to quadrupole

resonance mode. The third, at 388 nm, is a hybrid peak arising from the even contribution of dipole and quadrupole resonance modes.[189]

The scanning electron microscopy images (Fig. 53A, B) showed cubic nanoparticles with slightly rounded corners and smooth surfaces. The absence of larger cubical nanoparticles indicated that possibly no byproducts, such as AgCl nanocubes, were generated during the synthesis. Their size is uniform, without visible agglomerates or smaller nanoparticles, meaning a monodisperse and possibly stable system.

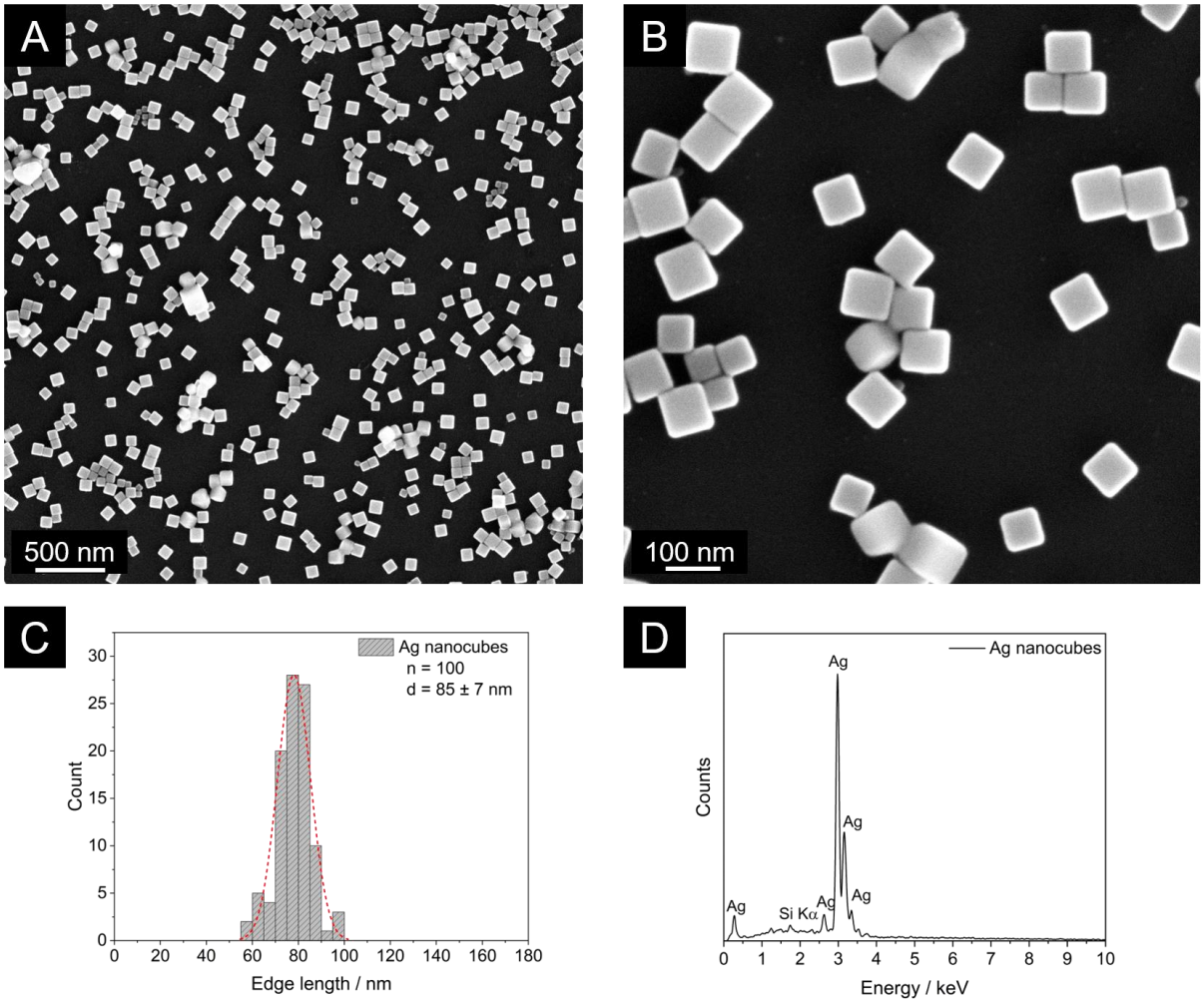

Figure 53. SEM images of silver nanocubes obtained from the polyol process recorded at magnifications of 50,000 (A) and 200,000 (B) with an accelerating voltage of 15 kV. SEM size distribution of silver nanocubes (C) along with the corresponding EDS spectrum (D). Si signal derives from the silicon wafer used for the measurement.

The particles showed a narrow distribution with an average edge length of 85 nm, a standard deviation of ±7 nm, and a PDI of 0.08 (Fig. 53 C). Consequently, the silver nanocubes could be characterized as a monodisperse system. Furthermore, with SEM, energy-dispersive X-ray spectroscopy was performed (Fig. 53 D) to examine if AgCl nanocubes were also formed as byproducts. EDS did not show signals indicating the formation of AgCl byproducts.

DLS and ζ-potential measurement was performed to verify the nanocubes' colloidal stability. Figure 54 shows the obtained size distribution by the number obtained from DLS.

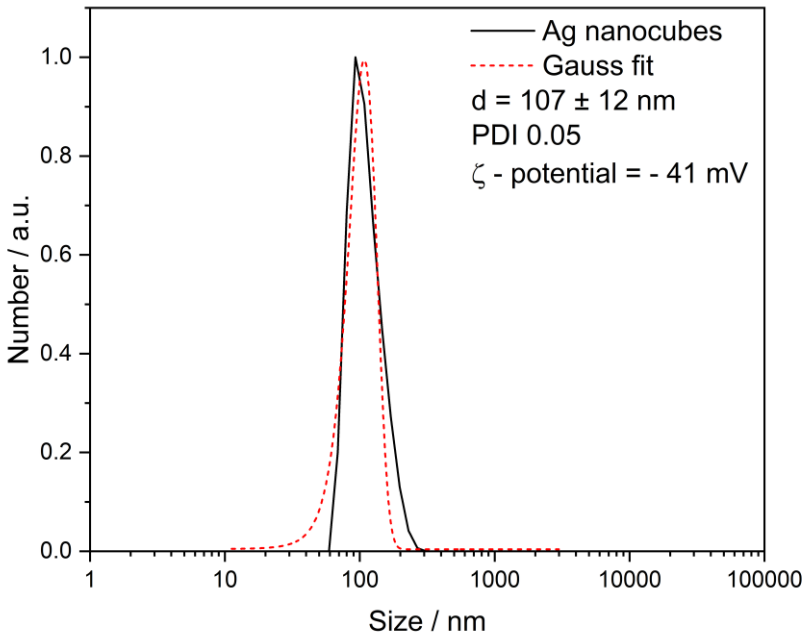

Figure 54. Particle size distribution (by number) obtained from DLS measurement of the silver nanocubes obtained from the polyol synthesis with oxidative etching.

The hydrodynamic diameter obtained from DLS showed a unimodal size distribution with a mean value of 107 nm and a standard deviation of ±12 nm. The size obtained from DLS appeared to be larger than the size of SEM (85 ± 7 nm). This difference between the two methods was expected as DLS provides information about the hydrodynamic diameter. The PDI obtained from DLS 0.06 showed that the system was monodisperse, while the strong negative ζ-potential, -41mV, indicated that the nanocubes were colloidally stable. The substantial negative value can be attributed to

the Cl^- ions, which are adsorbed on the surface of the nanoparticles alongside PVP, hence an electrosteric stabilization.

The DSC measure (Fig. 55) revealed a bimodal distribution as an additional small shoulder appeared. This small peak usually appears in the case of cubic nanoparticles. However, the size distribution obtained from the central peak provided a mean size of 81 ± 7 nm and a PDI of 0.08, which agreed with the values obtained from the previously presented characterization methods.

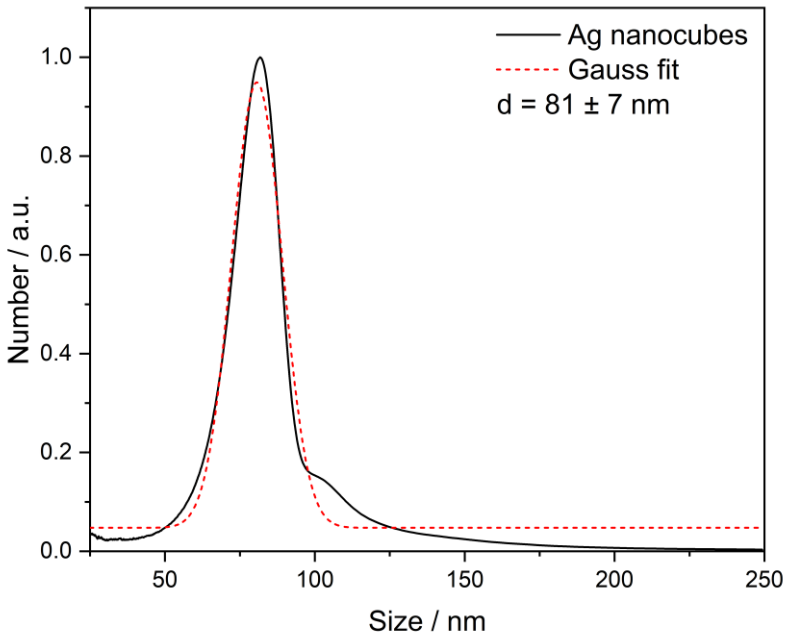

Figure 55. DCS measurements of the silver nanocubes obtained from the polyol synthesis with oxidative etching.

Despite their large size, obtaining images in higher resolution from TEM was possible, confirming the nanocubes' rounded edges and providing information about their crystallinity. Figure 56 (A) shows three silver nanocubes with a mean size of 83 nm, confirming SEM measurements. Furthermore, at a closer look, it was clear they consist only of one crystal, confirming that they are single crystalline structures (Fig. 56 B). Additionally, fast Fourier transformation (FFT) analysis (Fig. 56 C) indicated an [001] orientation and single crystalline nature.

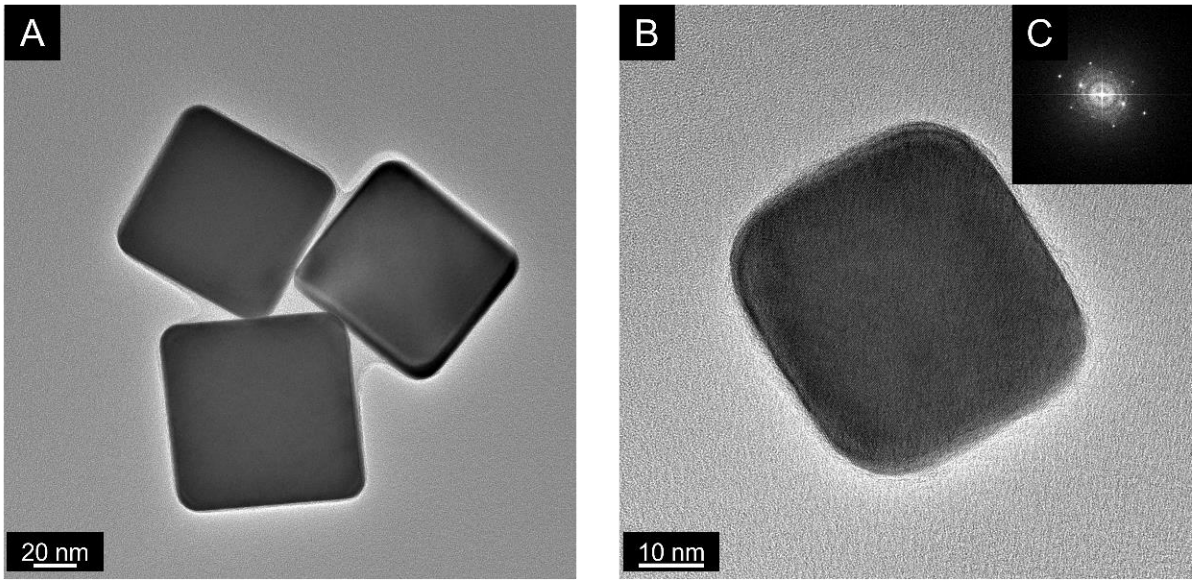

Figure 56. Bright-field TEM images of three silver nanocubes (A), a single nanocube (B) with corresponding FFT analysis (C).

PXRD measurement was performed to examine and confirm the purity and crystallinity of the silver nanocubes. The obtained PXRD pattern (Fig. 57) showed the characteristic reflexes of the fcc phase of metallic silver (Table 13). The strongest reflex corresponding to the (200) plane showed a high texture in the [100] direction, characteristic of cubic structures. The firm texture derived from their geometry. As they are enclosed of (100) planes, their preferred orientation is parallel to the substrate.[159, 190] Consequently, a mirror surface is formed, leading to a diffraction peak with unusually strong intensity.

Table 13. Classification of the experimental reflexes of silver nanocubes obtained from PXRD, based on the databank ICDD-PDF 04-0783.

Obtained reflex °2θ	Literature reflex °2θ	Lattice plane (hkl)
38.152	38.117	111
44.330	44.278	200
64.455	64.427	220
77.368	77.475	311
97.990	97.891	400

Rietveld refinement calculations resulted in a crystallite size of 90 nm, which agreed very well with the particle size determined by SEM, confirming the single crystallinity of silver cubic nanoparticles. The calculated silver lattice parameter, 4.0860 Å, agreed perfectly with the theoretical value of 4.0862 Å.

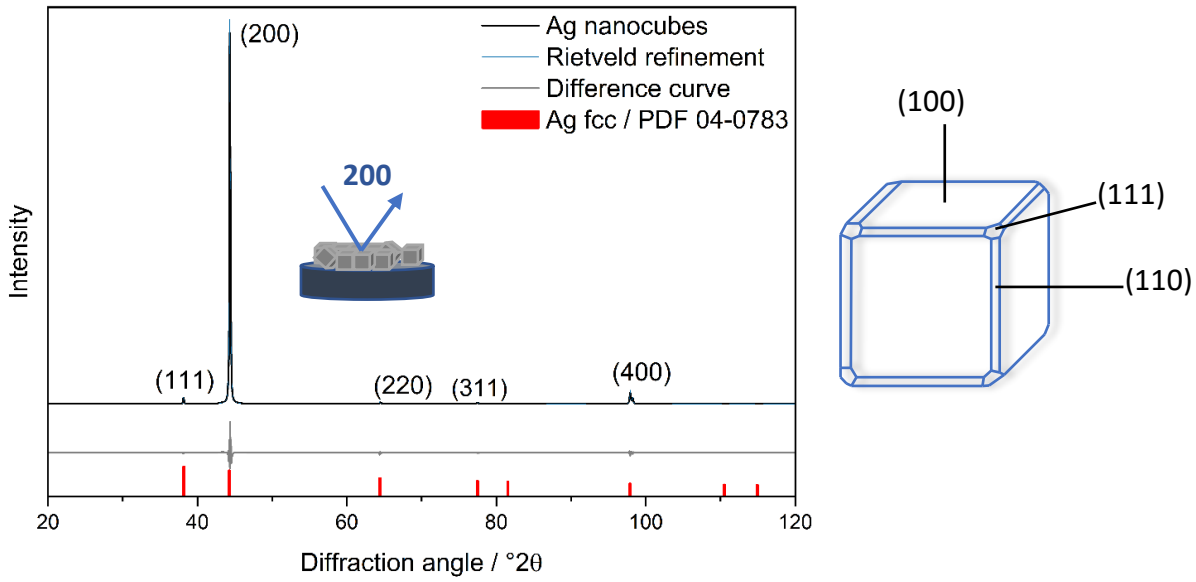

Figure 57. Rietveld-refined diffraction pattern of silver nanocubes obtained from powder X-ray diffraction and a schematic representation of a cube with the crystallographic orientation of the different surfaces.

Silver nanocubes with an average size between 80-90 nm and an average PDI of 0.07 were successfully synthesized. The generated particles were used to perform further core-shell and *in-situ* heating experiments. Table 14 summarizes the particle size distribution, standard deviation, and PDI obtained from scanning electron microscopy, dynamic light scattering, and differential centrifugal sedimentation.

Table 14. Comparison of particle size distribution, standard deviation, and polydispersity index (PDI) of silver nanocubes obtained from all size-determination methods.

Method	SEM	DLS	DCS
Size / nm	85	107	81
Standard deviation / nm	7	12	7
PDI	0.08	0.05	0.08

5.3 Synthesis of bimetallic nanoparticles

5.3.1 Characterization of core-shell silver-gold (Ag@Au) nanocubes

Generating noble metal core-shell structures is a highly challenging task. As discussed in Chapter 2.4.3, the primary obstacle is the galvanic replacement reaction between two metals due to the difference in their electrochemical potentials. It is crucial to successfully suppress and carefully control this reaction to produce core-shell bimetallic nanoparticles.

Here, the synthesized silver nanocubes were used as templates for the growth of a gold shell around them. The galvanic replacement reaction between silver nanoparticles and gold ions deriving from the reduction of tetrachloroauric (III) acid from ascorbic acid can be described with the following two half equations:[191]

$$Ag^{+}_{(aq)} + 1\ e^{-} \rightarrow Ag \qquad \varepsilon_1^0 = 0.8\ V \tag{13}$$

$$AuCl_4^{-}{}_{(aq)} + 3\ e^{-} \rightarrow Au^0 + 4\ Cl^{-}_{(aq)} \qquad \varepsilon_2^0 = 1.0\ V \tag{14}$$

Which leads to the final balanced equation:

$$AuCl_4^{-}{}_{(aq)} + 3\ Ag^0 \rightarrow 3\ Ag^{+}_{(aq)} + Au^0 + 4\ Cl^{-}_{(aq)} \qquad \varepsilon_3^0 = 0.2\ V \tag{15}$$

The silver atoms from the surface of the nanoparticles can be quickly oxidized and dissolved from the $AuCl_4^-$ ions due to the higher standard potential producing Ag^+ ions. These, in turn, lead to the formation of vacancies on the surface of the particles, offering open spots for the deposition of gold atoms produced from the reduction of gold ions (Fig. 58). Gradually, this results in hollow nanostructures.

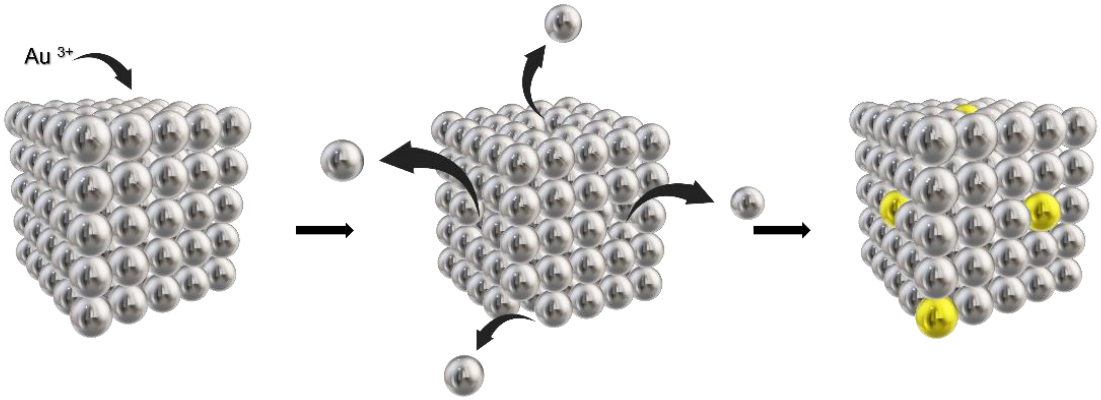

Figure 58. Schematic mechanism of the galvanic replacement reaction between silver and gold.

Several key parameters were carefully considered to establish a reliable and reproducible synthesis route that avoids the formation of hollow nanoparticles. Factors such as the molar ratio between the two metals, solution pH level, precursor concentration, and addition rate were thoroughly examined in the framework of this project.

The synthesis presented in this work was initially based on a methodology proposed by Yang *et al.*, with necessary modifications made accordingly. Their study suggested that adjusting the pH level of the solution to 11 optimizes the reduction power of ascorbic acid. The added tetrachloroauric acid will be exclusively reduced by the ascorbic acid before initiating the galvanic replacement reaction, resulting in a deposition of gold atoms on the surface of the silver nanocubes.

As previously mentioned, the variability among different systems necessitated the performance of multiple synthetic variations to study and optimize the synthesis process thoroughly. The most crucial objective was generating a complete shell around the nanocubes. Initial experiments revealed that a nominal composition of 70% silver and 30% gold resulted in the desired shell formation. However, to suppress the galvanic replacement reaction, further investigations were conducted. The same synthesis using a silver-to-gold molar ratio of 70:30 was carried out with varying pH values. It was observed that pH values under 11 resulted in hollow spots on the surface of the nanocubes, indicating the oxidation and dissolution of silver atoms from gold.

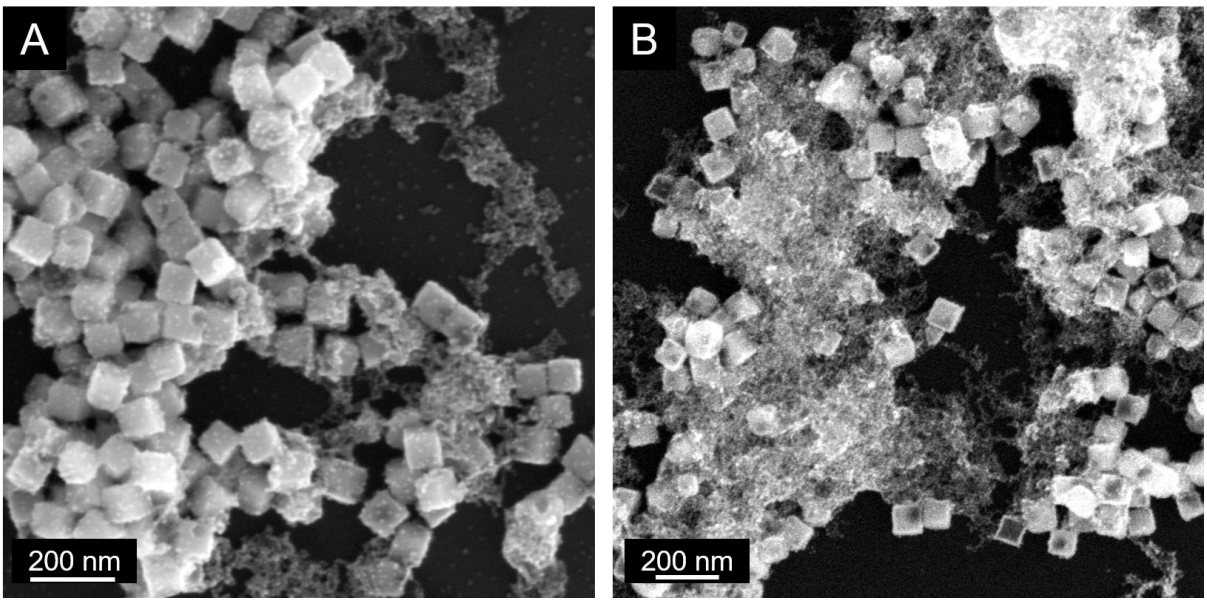

Figure 59. Nanoparticles were obtained from the Ag@Au core-shell synthesis with a molar ratio of 70:30, performed at 0 °C (A) and 50 °C (B). The images were taken at a magnification 200,000 (A) and 100,000 (B) times, and the accelerating voltage was 15 kV.

On the other hand, when the pH was above 12.5, the formation of small gold nanoparticles was observed. The same behavior was also observed when the synthesis was performed at both low temperatures (0 °C synthesis was performed in an ice bath, Fig. 59 A) and higher temperatures (50 °C). In the case of synthesis performed at 50 °C small gold nanoparticles were accompanied by hollow gold nanocubes (Fig. 59 B). Additionally, higher precursor concentrations resulted in the formation of hollow nanoparticles and a significant number of smaller nanoparticles. Using energy dispersive and atomic absorption spectroscopy, the analysis revealed that the final nominal composition between silver and gold was approximately 55:45 and 63:37, respectively. The higher concentration of gold likely contributed to the complete dissolution of silver nanocubes and the formation of smaller particles (Fig. 60).

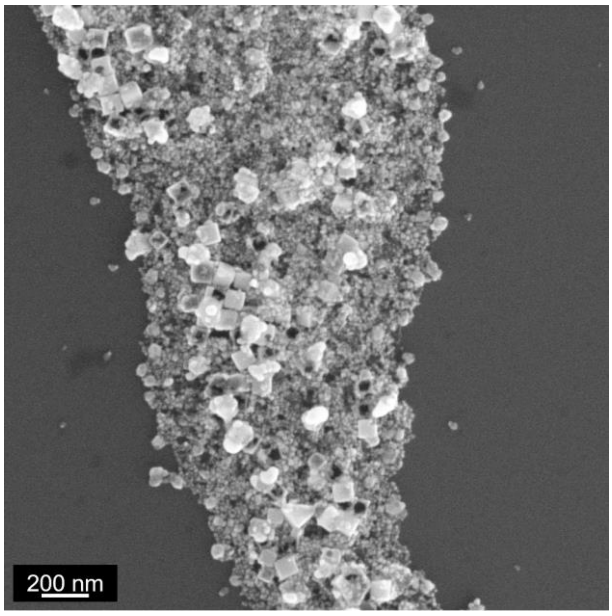

Figure 60. Nanoparticles obtained from the Ag@Au core-shell synthesis with a molar ratio 70:30 were carried out with a higher precursor concentration. The image was recorded at a 50,000 magnification, and the accelerating voltage was 15 kV.

The addition rate of the metal precursor ($HAuCl_4$) plays a crucial role in the synthesis, influencing the outcome. Figure 61 shows scanning electron microscopy images and corresponding mapping obtained from energy dispersive spectroscopy from the synthesis conducted at varying addition rates. When the metal precursor, tetrachloroauric (III) acid, was added at 0.2 and 0.15 mL min^{-1}. SEM images exhibited core-shell silver nanocubes with a well-formed and compact shell. However, upon careful evaluation, the optimal addition rate of 0.15 mL min^{-1} was selected due to its ability to deliver a final molar ratio between the two metals (AAS 76:24, EDS 77:23) that closely matched the initial molar ratio (70:30). This choice ensured a more controlled and desired composition.

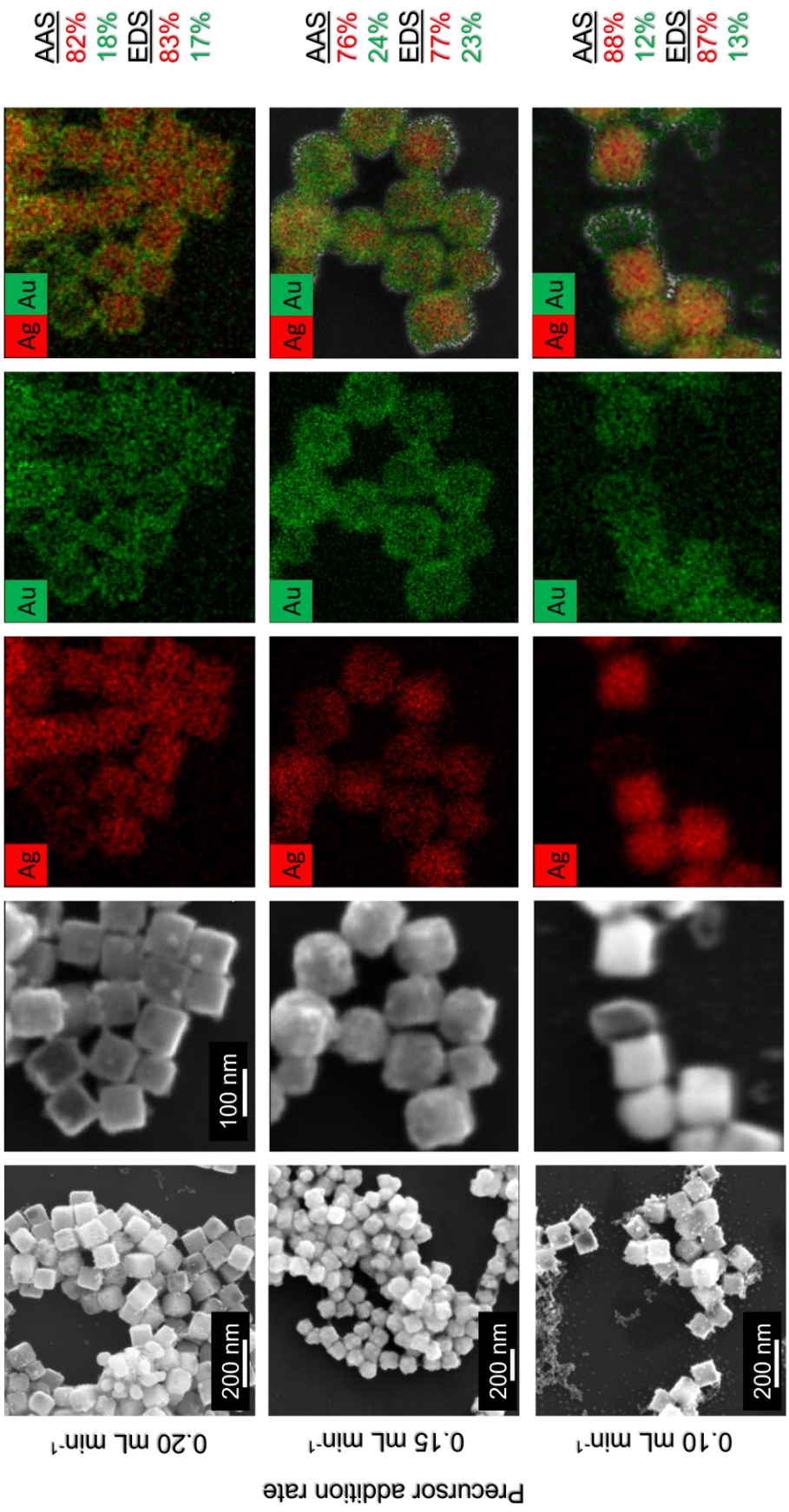

Figure 61. Core-shell Ag@Au synthesis with a nominal composition 70:30. The gold precursor was added in each synthesis at a different rate. SEM images taken with an accelerating voltage of 15 kV (first column), and 10 kV (second column), EDS mapping of Ag (marked with red, third column), Au (marked with green, fourth column), overlay, fifth column), nominal composition obtained from AAS and EDS (last column).

The optical properties of the obtained core-shell nanocubes were examined by ultra-violet and visible spectroscopy. It is known that both silver and gold nanoparticles exhibit plasmonic behavior, and the presence of a shell around the nanocubes is expected to result in a distinct spectral response.

Figure 62 shows a comparison of the UV-Vis spectra obtained from pure silver and core-shell silver-gold nanocubes with a molar ratio of 70:30. As expected, the prominent maxima at 388 nm and 501 nm of the silver nanoparticles were no longer visible in the core-shell spectrum. Instead, a red-shifted peak at 680 nm emerged, characteristic of gold nanoparticles.[192] The absence of the characteristic localized surface plasmon resonance (LSPR) peaks of the silver nanocubes in the spectrum of the bimetallic structures could be considered a strong indication of the formation of a compact gold shell around the seeds.

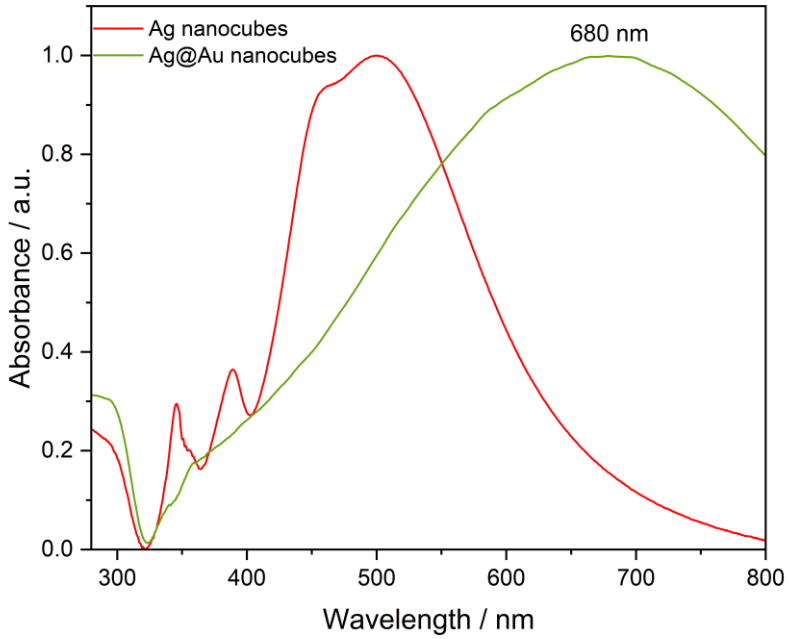

Figure 62. UV-Vis spectra of silver (red) and silver-gold core-shell nanocubes (green) with a molar ratio silver to gold 70:30.

Scanning electron microscopy images have provided further evidence of the successful formation of a complete shell around the silver nanocubes (Fig. 63A). Compared to the smooth surface of the silver nanocubes, the core-shell nanoparticles exhibited an uneven surface after adding gold. This unevenness was attributed to the

deposition of gold atoms on their surface. The SEM analysis also yielded a particle size distribution (Fig. 63B), revealing an average edge length of 96±10 nm with a low PDI of 0.1.

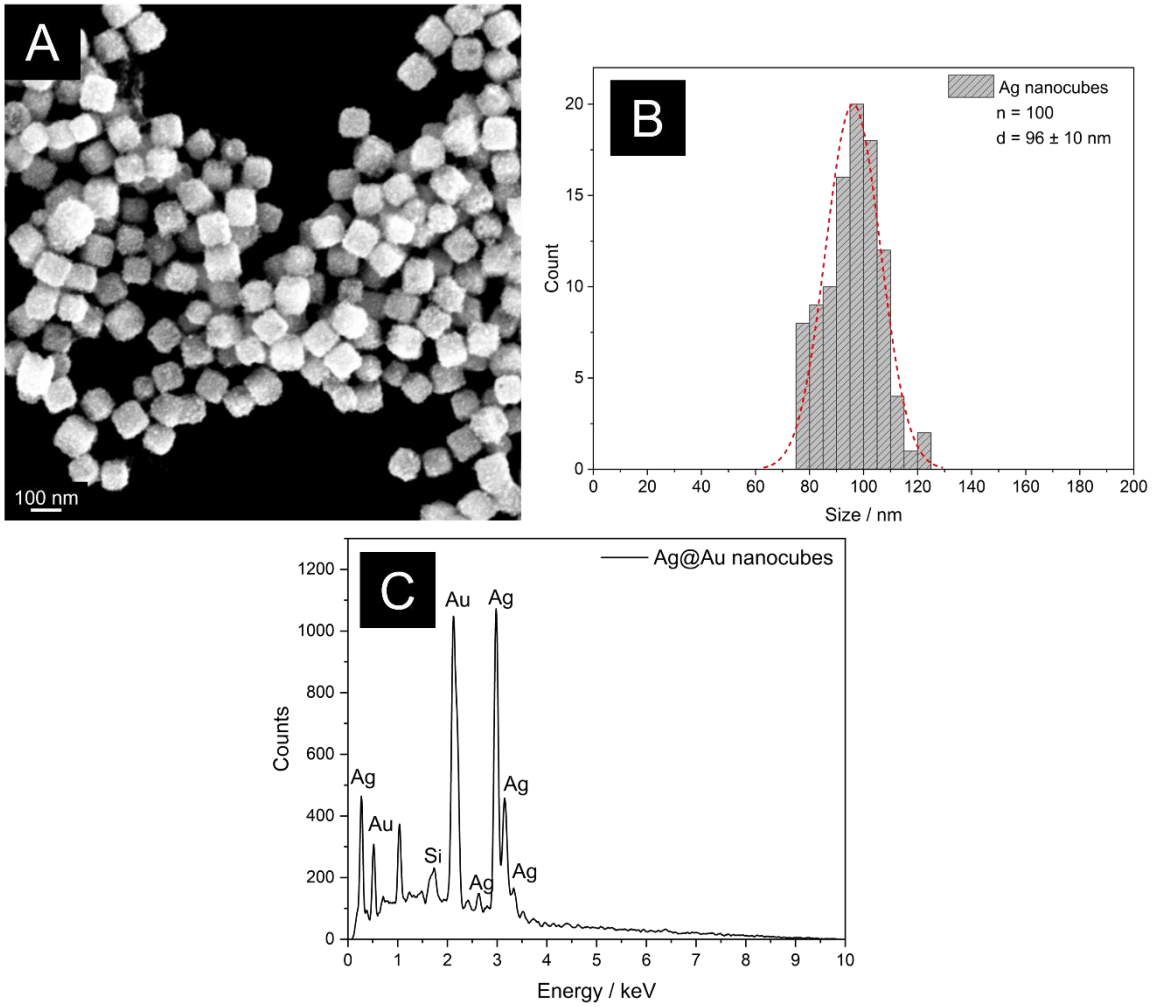

Figure 63. SEM image of the obtained core-shell nanocubes with a nominal composition 70:30 (A), the corresponding particle distribution (B), and EDS spectrum (C). The SEM image was taken with a magnification of 150,000 times and an accelerating voltage of 10 kV.

To determine the molar ratio of the two metals in the final product, energy dispersive X-ray spectroscopy (EDS) was employed. The EDS analysis provided a molar silver-to-gold ratio of 77:23. EDS mapping was conducted to visualize the exact distribution of gold and silver on the particles, further confirming the formation of core-shell structure rather than alloyed nanoparticles (Fig. 61 middle row). Moreover, atomic absorption spectroscopy was employed to determine the final nominal

composition of silver-to-gold. The analysis resulted in a molar ratio of 76:24, which aligns perfectly with the composition obtained from EDS.

To assess the size distribution and colloidal stability of the core-shell nanoparticles, DLS was conducted and ζ-potential was measured. The hydrodynamic diameter obtained from dynamic light scattering showed a mean value of 127 nm with a standard deviation of 13 nm. This increase in size compared to the initial silver nanocubes (107 nm) indicated the successful formation of a gold shell around the particles. The low PDI of 0.02 further confirmed the monodispersity of the core-shell system. The negative ζ-potential, -25 mV, also indicated a colloidally stable system.

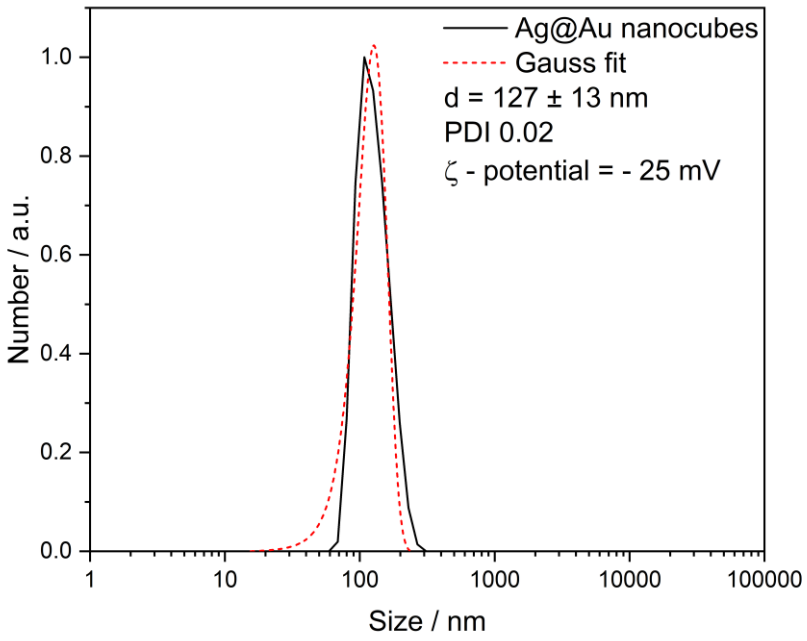

Figure 64. DLS measurement of the silver-gold core shell nanocubes with a nominal composition of silver-to-gold 70:30.

The core-shell particles were examined under transmission electron microscopy (TEM) and X-ray powder diffraction to gain more information about the morphology and crystalline structure.

High-angle annular dark field imaging was employed to gain detailed insights into the formation of the gold shell on the silver nanocubes. This imaging technique, which takes advantage of the higher atomic number than silver, allowed the distinction

between the two metals. The obtained images demonstrate the presence of a compact and uniform shell surrounding the silver core. Complementary EDS map (Fig. 65B) further confirmed the core-shell nature of the bimetallic nanocubes.

In a previous work by Dr. Pappert, it was proposed that the growth of the gold shell around the nanocubes initiates preferentially on the (111) facets.[152] This preference can be attributed to the inhibiting effect of the stabilizing agent PVP on the (100) facets, retarding the crystallization of gold atoms on these planes. As a result, the (111) facets serve as the preferred sites for gold deposition. In this case, the gold atoms crystallized epitaxially on the surface of silver nanocubes, forming a shell with a thickness of approximately 8-9 nm. However, it is worth noting that there were regions where the shell thickness appeared thicker and exhibited uneven growth.

This growth behavior can be explained by the Stranski-Krastanov mechanism. According to this mechanism, initially, the shell formation occurs as a two-dimensional layer. As the layer reaches a critical thickness, three-dimensional islands begin to form, leading to the observed variations in shell thickness. The critical layer thickness depends on the substrate and the layer's surface energies and lattice parameters.[193-195]

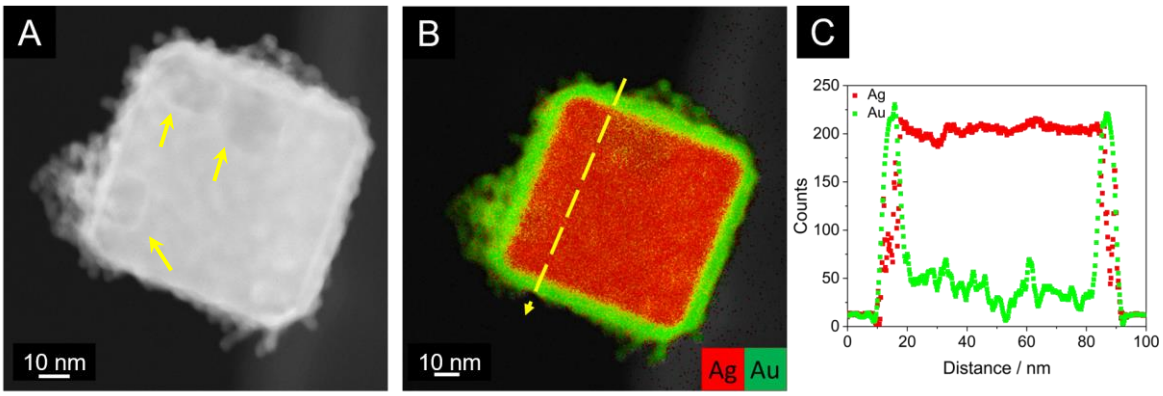

Figure 65. HAADF STEM image (A) and map (B) of a silver-gold core-shell nanocube with a nominal composition 70:30 and the corresponding line scan (dashed yellow arrow B, C).

The slightly darker regions (indicated by yellow arrows, Fig. 65 A) observed in the HAADF image of the displayed particle can be attributed to variations in the density within the silver core. These regions might be porous or hollow due to local galvanic replacement reactions that take place.

X-ray diffraction provided information about the crystallography of the formed shell around the silver seeds. Figure 66 shows the recorded diffractogram of the silver-gold core-shell nanocubes. At first look, the absence of the strong intensity of the (200) observed previously on the diffraction pattern of silver cubes indicated that the rough surface of the bimetallic structures has affected the preferred orientation. It can be assumed that the nanocubes were not laying anymore on their (100) surfaces, and if they did, their uneven surface could not provide comparatively the same strong signals.

As the lattice parameter of silver (4.086 Å) and gold (4.079 Å)[196] for the fcc phase are almost similar, distinguishing and classifying the obtained reflexes can often be challenging.[197]

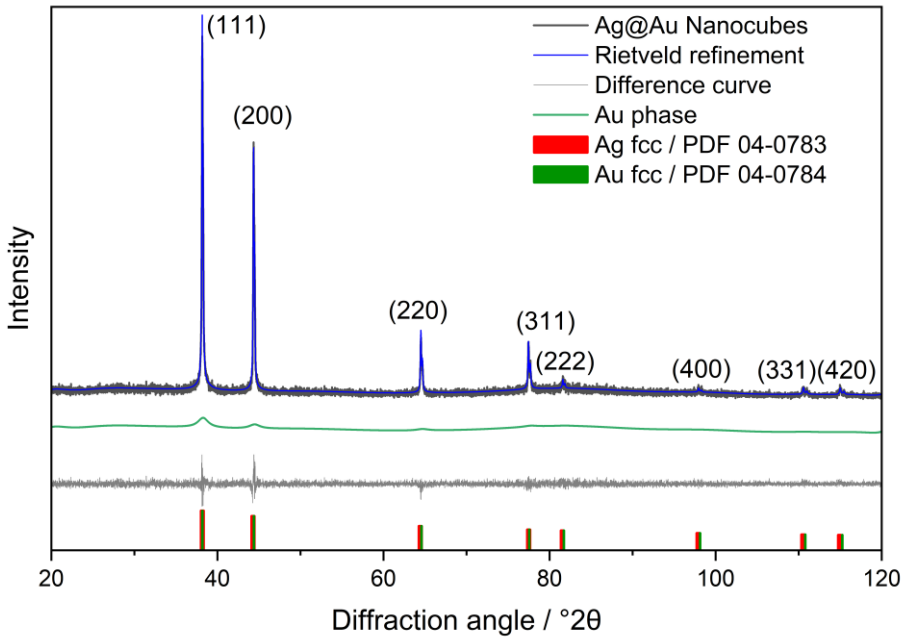

Figure 66. Rietveld-refined diffraction pattern of silver-gold core-shell nanocubes obtained from powder X-ray diffraction. The peak profile was calculated using fcc-phases of silver and gold. Miller indices of Ag and Au fcc phases are given in parentheses.

Table 15 depicts each phase's lattice parameter and crystallite size, as determined through Rietveld analysis. The analysis of the silver fcc phase gave a crystallite size of 70 nm, slightly smaller than the initial size of silver nanocubes without the shell. The reduction in the silver crystallite size of silver can be attributed to the dissolution of a

certain amount of silver during the deposition of gold on the surface. The presence of gold atoms on the surface leads to the replacement of silver atoms, resulting in a decrease in the domain size of the silver phase. Respectively, the gold fcc phase analysis gave a crystallite size of 3 nm. This size corresponded to approximately 1/3 of the particle size (10 nm) obtained from transmission electron microscopy images (Fig.67). The smaller crystallite size than the particle size indicated a polycrystalline structure of the gold nanoparticles crystallized on the surface of silver nanocubes, i.e., five-fold twinned silver nanospheres.

Table 15. Lattice parameters and crystallite sizes were calculated from Rietveld refinement analysis.

Phase	Lattice parameter / Å	Crystallite size / nm
Ag fcc	4.085 (2)	70 (2)
Au fcc	4.079 (1)	3 (1)

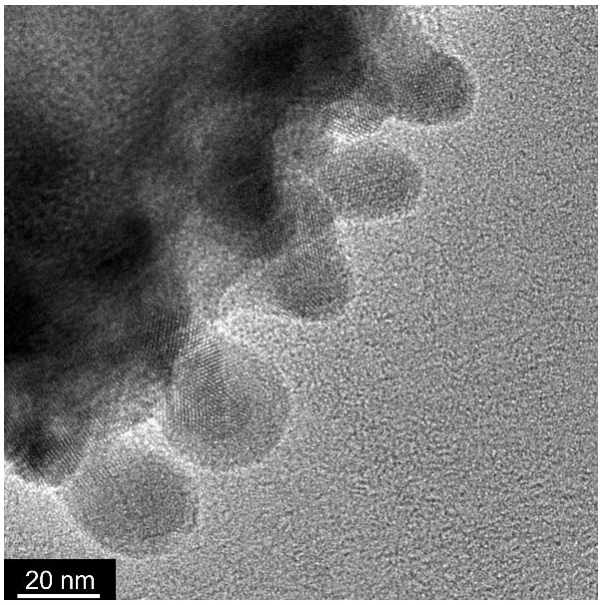

Figure 67. Bright-field TEM image of the gold shell formed on the surface of the silver nanocubes, consisting of 10 nm gold nanoparticles.

The lattice parameters calculated for the silver and gold fcc phases, 4.085 Å and 4.079 Å, respectively, match closely with the theoretical values of 4.086 Å and 4.078 Å. The accurate alignment with the theoretical lattice parameters further supported the

core-shell structure and verified the absence of significant interfusion or alloying between silver and gold.

The composition analysis also obtained from Rietveld analysis revealed that the particles consisted of 72% silver and 28% gold. The composition aligned well with the results obtained from AAS and EDS (Table 16), providing consistent and reliable information about the relative amounts of silver and gold within the core-shell nanoparticles.

Table 16. Three independent methods determined the elemental composition of silver-and gold core-shell nanocubes.

	AAS	**EDS**	**XRD**
Silver / mol%	77 ± 6	76 ± 4	72 ± 5
Gold / mol%	23 ± 7	24 ± 2	28 ± 5

Overall, 96 nm silver-gold core-shell nanocubes with an approximate nominal composition of silver-to-gold 75:25 were successfully synthesized and fully characterized using spectroscopical, colloidal, microscopical, and diffraction techniques.

5.3.2 Characterization of platinum nanocages

For the synthesis of platinum nanocages, 85 nm silver nanocubes that had been previously synthesized were used as sacrificial template. By exploiting the galvanic replacement reaction that occurs between platinum and silver[198] (since platinum is nobler that silver, eq. 16), hollow platinum nanocubes were successfully produced.

$$2\ Ag_{(s)} + [PtCl_4]^{2-}{}_{(ag)} \rightarrow 2AgCl_{(aq\ or\ s)} + Pt_{(s)} + 2\ Cl^-_{(aq)} \qquad (16)$$

The optical properties of the obtained nanocages were examined by ultra-violet and visible spectroscopy. As silver nanoparticles exhibit plasmonic behavior, it was expected that they would show characteristic peaks in the UV-Vis spectrum. However, in the case of the platinum-coated nanocubes, no signal corresponding to the silver nanoparticles was observed (Fig. 68). The absence of the prominent maxima at 388 nm and 501 nm indicated the complete dissolution of the silver nanocubes and suggested the formation of nanocages, core-shell structures, or other platinum nanoparticles. Further characterization was needed to determine the exact nature of the resulting structures.

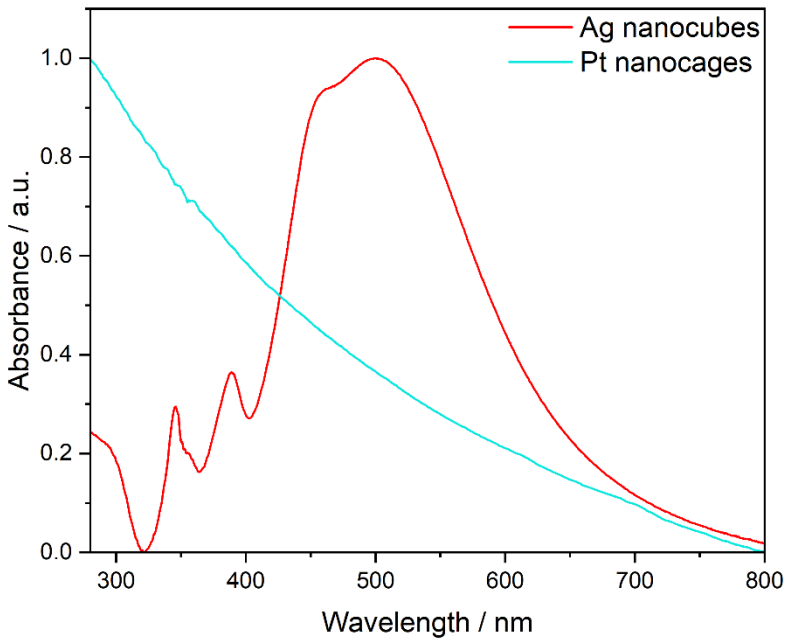

Figure 68. Comparison of UV-Vis spectra of Ag nanocubes (red curve) and Pt nanocages (light blue). The Pt curve shows no LSPR signal indicating the formation of a Pt shell.

Scanning electron microscopy imaging of the synthesized nanocages (Fig. 69) revealed the formation of uniformly sized particles with an average outer edge length of 104 ± 8 nm, inner edge length of 74 ± 10 nm, and a PDI 0.05. The consistent cage-like structure observed exhibited a monomodal size distribution without signs of agglomerates or the formation of smaller nanoparticles or other morphologies. The calculated thickness of the platinum shell was about 10 nm.

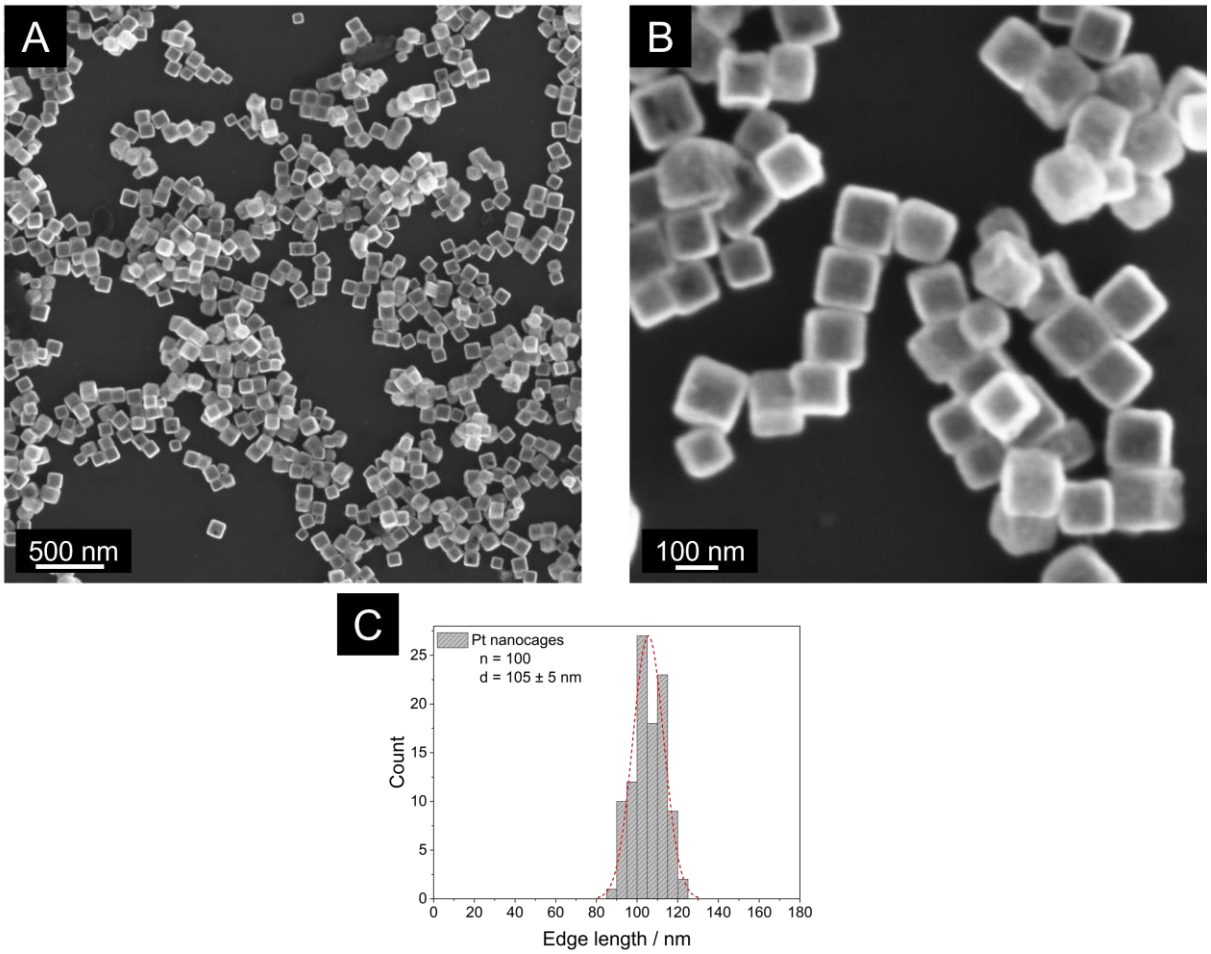

Figure 69. SEM images of platinum nanocages were recorded both with an accelerating voltage of 15 kV and magnification of 100,000 (A) and 200,000 (B) times and corresponding SEM particle size distribution.

Dynamic light scattering analysis (Fig. 70) of the nanocages yielded a particle size distribution with an average hydrodynamic size of 157 nm and a standard deviation of 15 nm. The low PDI of 0.15 indicated a monodisperse system, suggesting that the majority of the particles had a similar size and no additional platinum nanoparticles were formed during the deposition of platinum on the surface of the particles. Additionally, the ζ-potential value of -23mV indicated a colloidally stable system. This suggested that the nanocages were well-dispersed and less likely to agglomerate or precipitate, contributing to their long-term stability.

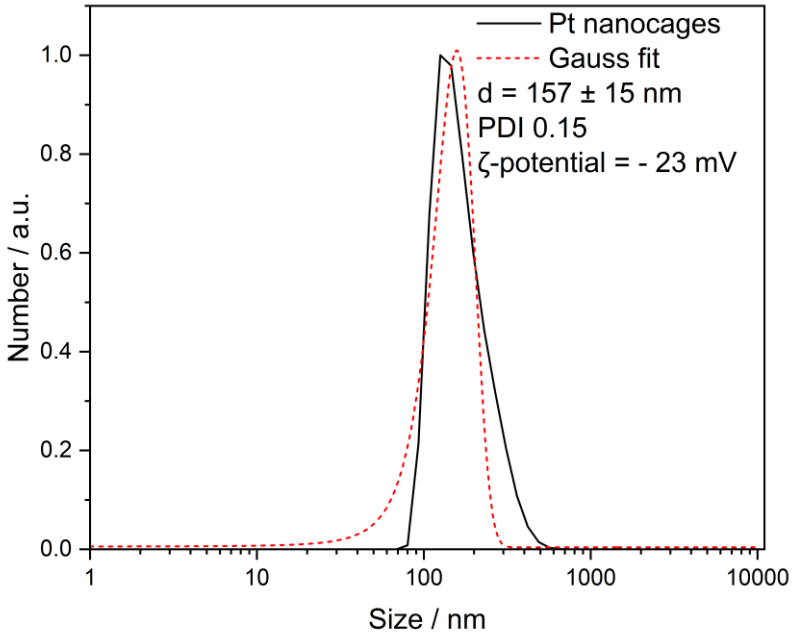

Figure 70. Particle size distribution (by number), PDI obtained from DLS measurement of platinum nanocages and the corresponding ζ-potential value.

Electron X-ray dispersive spectroscopy was employed to examine the composition of the platinum nanocages precisely. The analysis revealed a molar ratio of 95:5 for platinum to silver. Despite the samples being washed with concentrated nitric acid, a small amount of silver was still detected. It can be assumed that during the formation of the shell and the galvanic replacement reaction, a few silver atoms were not fully displaced from the particles. Consequently, they were “trapped” underneath or between the platinum nanoparticles that constitute the shell/frame of the

nanocages.[199] The concentrated nitric acid used during the washing process was unable to penetrate and dissolve the remaining silver, hence the small silver amount.

Additionally, EDS mapping (Fig. 71) was conducted, which further confirmed the platinum rich the frame of the nanocages.

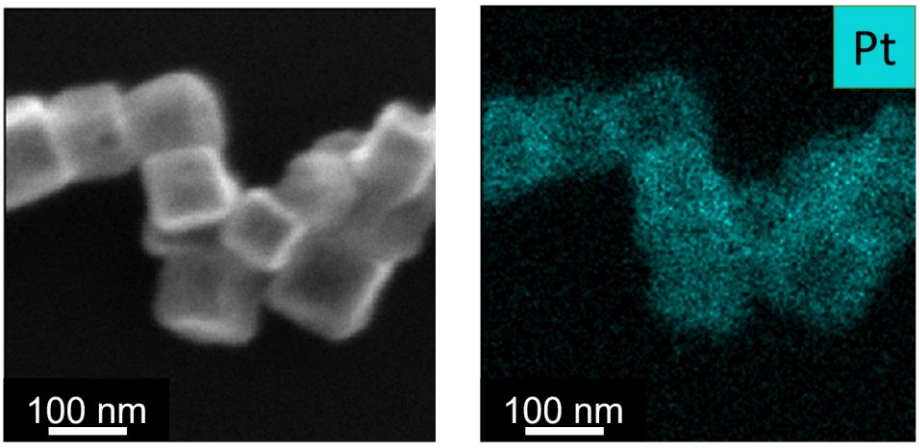

Figure 71. EDS mapping of the generated platinum nanocages, showing the platinum-rich frame.

A more detailed insight into the structure of platinum nanocages was provided by TEM. Figure 72 (A) displays an overview of seven nanocages. Unlike SEM, it was evident there that the shell/frame, like the silver-gold core-shell nanocubes previously discussed, consisted of small platinum nanoparticles measuring approximately 3-4 nm (Fig. 72 C). This observation suggested that the shell's growth did not occur through the epitaxial deposition of platinum atoms on the nanocubes' surface. Instead, small nanoparticles were deposited, forming a compact yet relatively porous shell, which in turn led to nanocages with an uneven surface. The shell's thickness was about 10 nm, which was consistent with the previous SEM measurements.

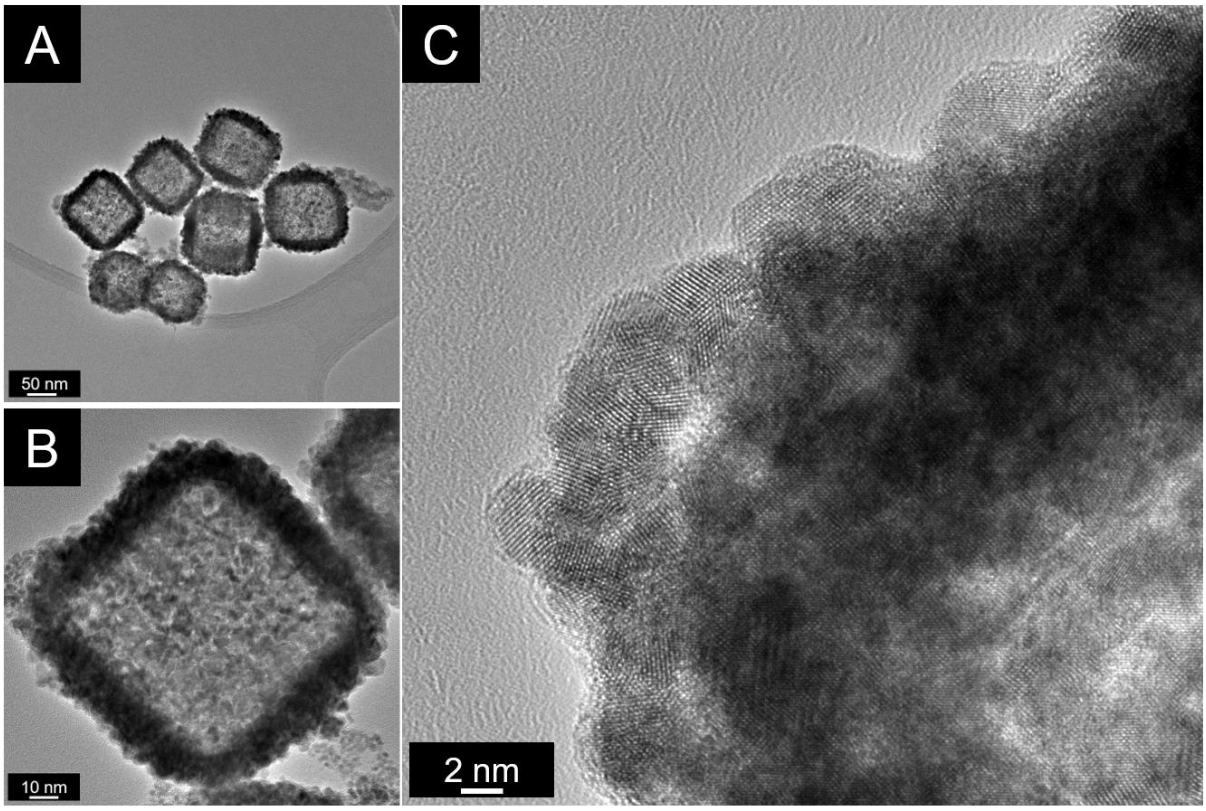

Figure 72. Overview of several Pt nanocages in TEM (A), a single nanocage (B), and focused image on the Pt (C) nanoparticles on the frame of the cages.

5.3.3 Characterization of core-shell palladium-platinum nanocubes

To produce palladium-platinum core-shell nanocubes, a seed-and-growth approach was chosen based on a protocol proposed by Xie *et al*.[200] Palladium nanocubes, 18 nm in size, were used as seeds and a solution of hexachloroplatinate (IV) hexahydrate was added at a carefully controlled rate the in presence of ascorbic acid, potassium bromide and polyvinylpyrrolidone to initiate the platinum shell formation.

UV-Vis spectra obtained from the bimetallic nanoparticles showed no LSPR peak. The absence of the LSPR peak in the UV-Vis spectrum of the bimetallic nanoparticles strongly suggested the formation of a platinum shell around the 18 nm palladium nanocubes.

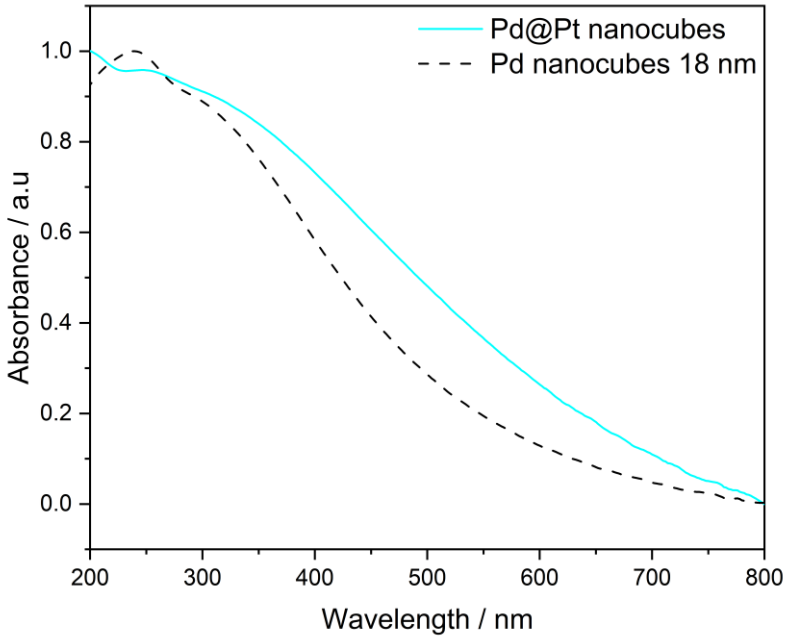

Figure 73. Comparison of UV-Vis spectra of palladium nanocubes (dashed curve) and bimetallic Pd-Pt nanocubes (light blue).

Scanning transmission electron microscopy images (Fig. 74) revealed that the nanoparticles maintained their cubic morphology, although with some noticeable changes. The edges and corners of the particles appeared more rounded, and the overall shape was less well-defined compared to the 18 nm palladium nanoparticles. The increase in the edge length from 18 to 21 nm for the nanocubes (Fig. 74 C) and from 21 to 24 nm for the nanobars (indicated with red arrows Fig. 74 A, Fig.74 D)

further confirmed the deposition of platinum onto the palladium nanoparticles. Additionally, no hollow structures were observed, indicating the formation of core-shell structures rather than hollow nanoparticles.

Energy-dispersive X-ray spectroscopy (Fig. 74 B) analysis was performed and confirmed the presence of both platinum and palladium in the sample, with a nominal composition of 85:15. This finding was in good agreement with the ratio determined through atomic absorption spectroscopy, which showed a nominal composition of 90:10.

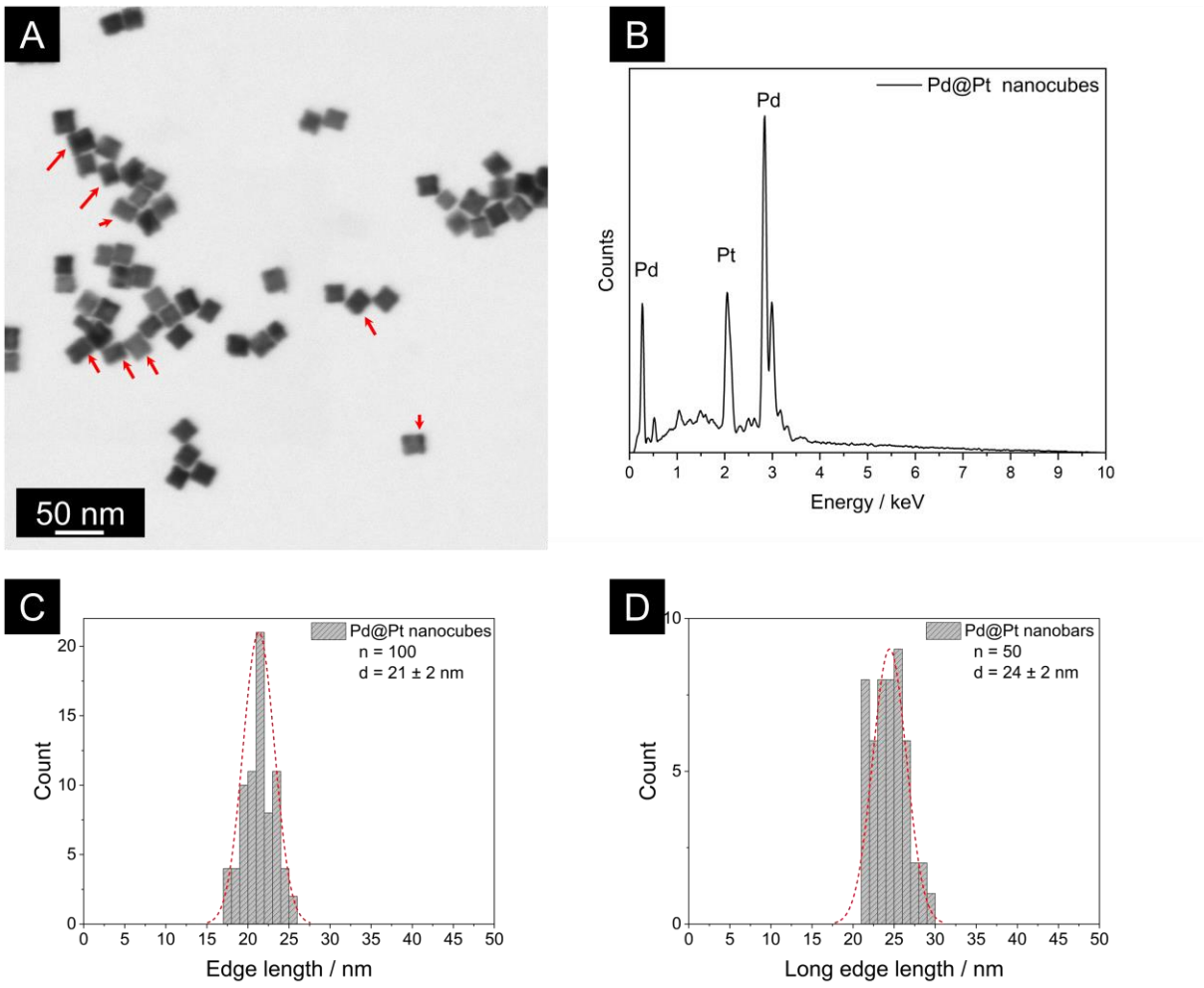

Figure 74. STEM image of core-shell Pd@Pt nanocubes and nanobars (A), EDS spectrum (B), and the correspondent STEM particle size distribution for both structures (C and D).

The particle size distribution obtained from dynamic light scattering (Fig. 75) showed a similar increase in the mean hydrodynamic diameter of the nanoparticles from 35 ± 8 nm to 42 ± 9 nm, confirming the deposition of platinum on the palladium

nanoparticles. Furthermore, the polydispersity index value of 0.26 remained almost unchanged, indicating a monodisperse system. The ζ-potential also remained constant at -24 mV, indicating that the bimetallic nanoparticles remained colloidally stable throughout the synthesis.

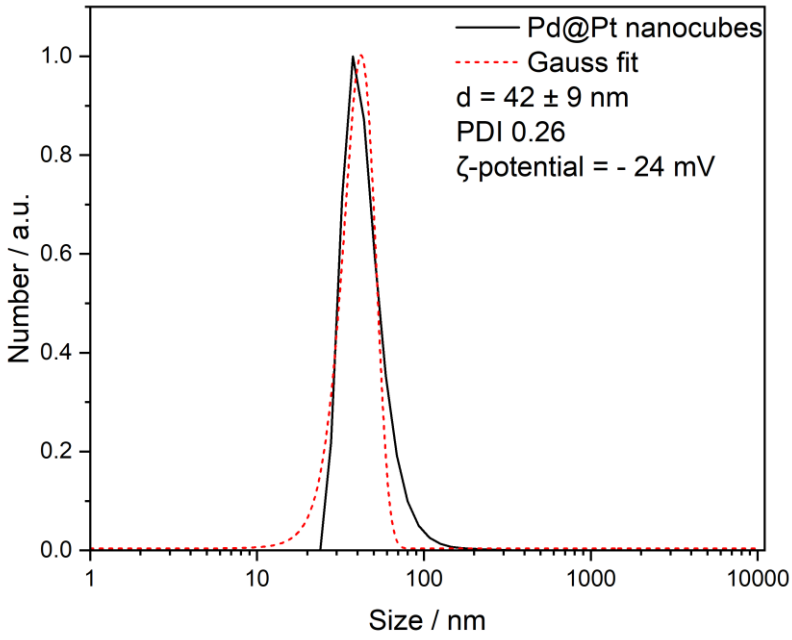

Figure 75. Particle size distribution (by numner) obtained from the DLS measurement of core-shell Pd@Pt faceted nanoparticles synthesized with a seed-and-growth approach.

Transmission electron microscopy images provided clear evidence of the successful formation of bimetallic core-shell palladium-platinum nanostructures (Fig. 76). The similar lattice constants of platinum and palladium (3.9242 Å for Pt[201] and 3.8907 Å for Pd[1]) enabled conformal deposition, resulting in epitaxial growth of platinum on the palladium seeds. The slow injection of the platinum precursor in the reaction mixture aimed to achieve heterogeneous nucleation of platinum atoms on the palladium seeds, and this approach proved to be effective. However, it was also observed that the palladium core partially dissolved during the process, leading to the formation of concave nanostructures. Although further experiments were not conducted within the scope of this thesis, optimization of the synthesis parameters may offer opportunities

to control the rate of precursor deposition and fine-tune the final shell thickness of the nanoparticles.

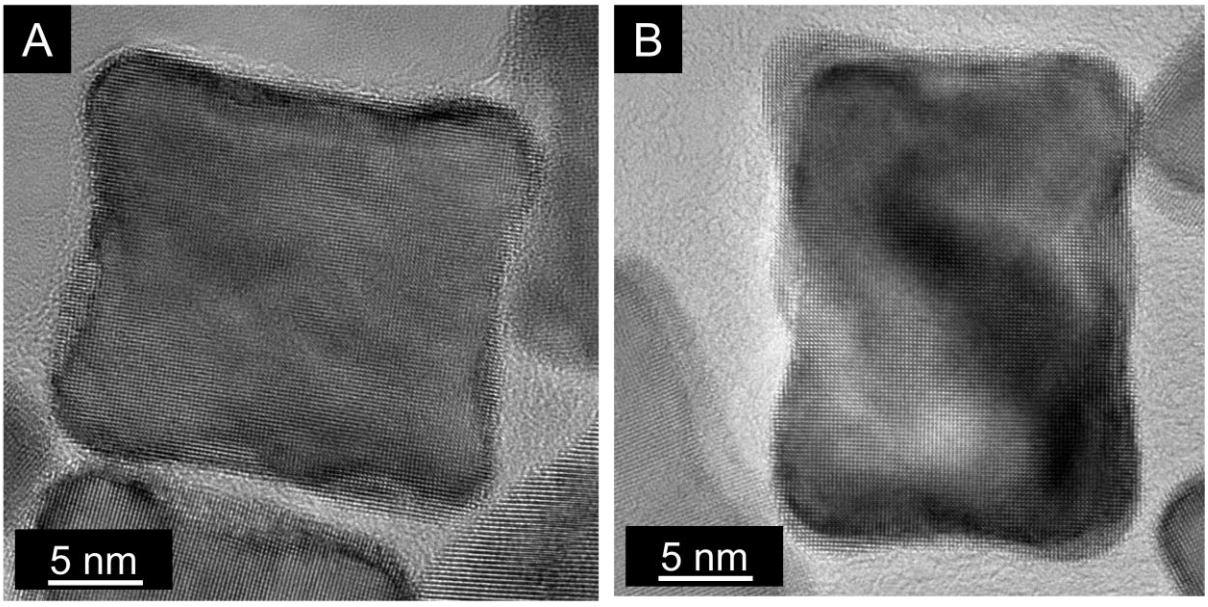

Figure 76. TEM images of core-shell Pd@Pt faceted nanoparticles, a nanocube (A), and a cuboid (B) showing the epitaxial formation of the Pt shell.

5.4 Thermal stability experiments

5.4.1 *In-situ* TEM and XRD heating experiments on silver nanocubes

Figure 76 showcases a series of transmission electron microscopy images captured while heating silver nanocubes at temperatures ranging from 25 to 800 °C. The investigation focused on three nanoparticles located at a specific position with varying edge lengths (84 nm, 77 nm, and 89 nm). Interestingly, the nanoparticles' size exhibited stability up to 600 °C. However, at 600 °C, the corners of the nanocubes began to gradually round off by exposing their (110) facets. Their size remained unchanged until 650 °C (Video 1, Appendix 9.3). Upon reaching 700 °C, they lost their cubic shape as the exposure of (110) facets increased, resulting in the formation of truncated octahedra. Finally, at 800 °C, the silver nanocubes underwent complete sublimation. The outline of the nanocubes at 800 °C can be attributed to the pyrolysis products of the capping agent, PVP, and to stretch marks of the carbon substrate.

Previous studies on the kinetic pathways of the sublimation of silver spherical nanoparticles have demonstrated its dependence on size, crystallinity defects, and time. Regarding size dependence, it has been observed that the sublimation temperature increases with increasing particle size, confirming the theoretical predictions deriving from the Kelvin equation.[202-204] However, in this case, even the smaller nanocubes maintained their size integrity up to 600 °C, exhibiting similar behavior to the larger cubes. It could be concluded that the size difference between them should be significantly larger to observe an earlier initiation of the sublimation process.

As for the crystallinity defects, it was concluded that silver nanoparticles with a high surface energy, i.e., silver nanoparticles with defects in their atomic structure , such as five-fold twinned silver nanoparticles, underwent a non-uniform sublimation pathway. [205]

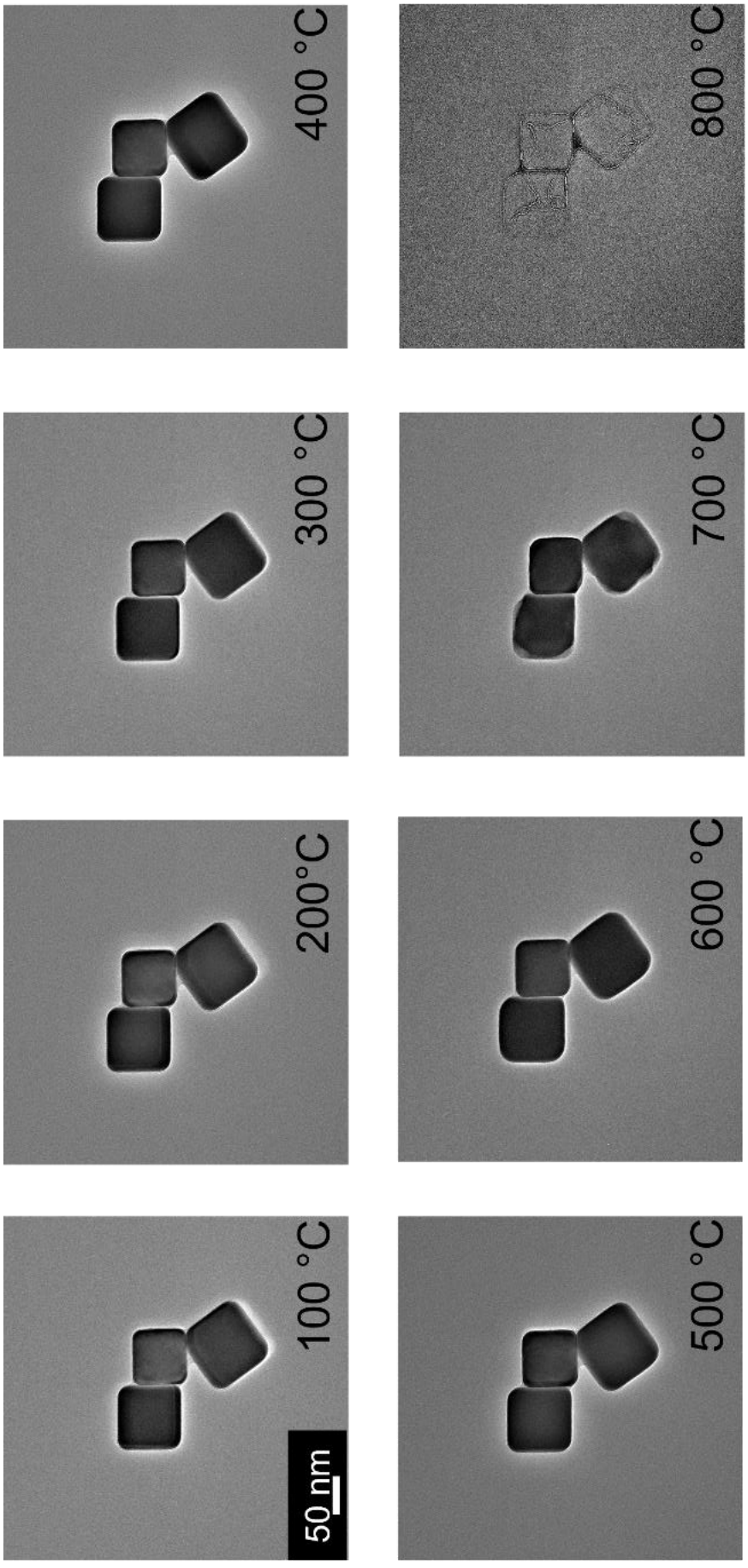

Figure 76. Bright-field TEM images of silver nanocubes during *in-situ* heating experiment up to 800 °C. Above 700 °C, sublimation of silver occurred (pressure 10^{-5} Pa).

In-situ X-ray powder diffraction (PXRD) experiments were conducted to gain insight into the crystal structure and its potential changes during the heating process. Figure 77 demonstrates a series of PXRD patterns collected from room temperature to 800 °C.

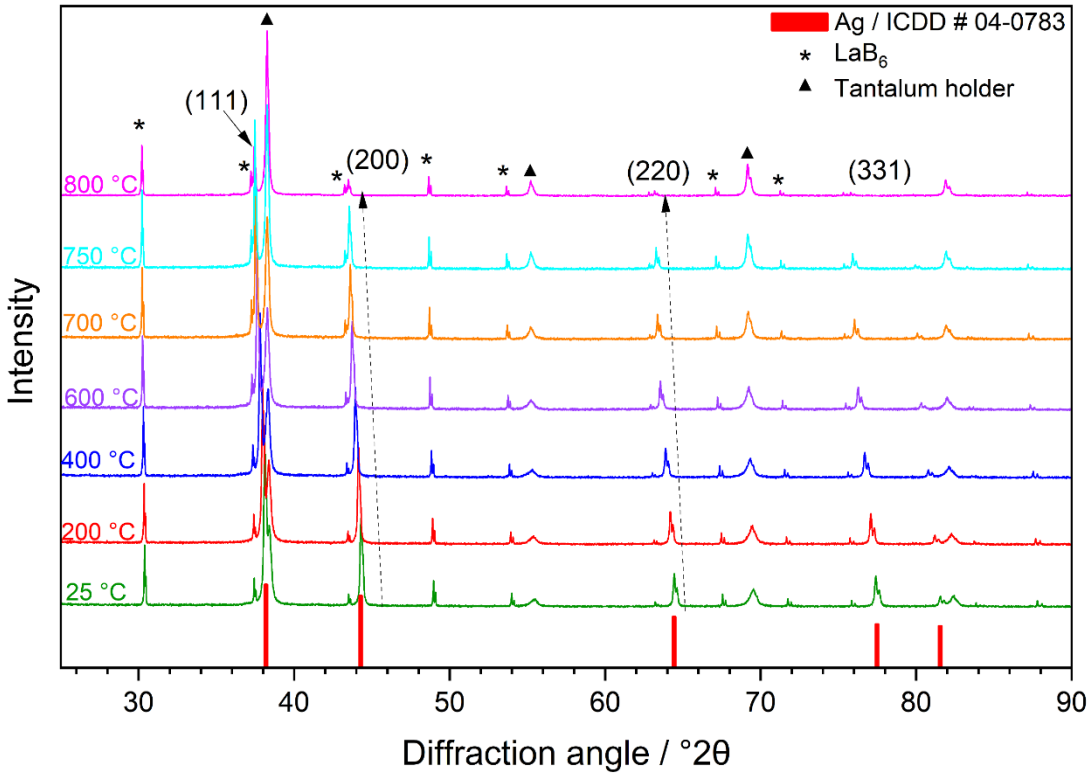

Figure 77. *In-situ* X-ray powder diffractograms of silver nanocubes mixed with LaB_6 (labeled with *; split peaks due to Cu K_α1,2 radiation) on a tantalum sample holder (marked with ▲). The silver (fcc) peaks (111), (200), (220), and (331) are indicated.

All patterns exhibited the characteristic diffraction peaks corresponding to the fcc phase of elemental silver, as discussed in Chapter 4.4.2.3. Additionally, apparent reflexes originated from the tantalum sample holder (marked with ▲) and the incorporated reference material LaB_6 (marked with *). As the temperature increased, a shift towards lower 2θ values was observed for all the peaks attributed to the fcc silver phase. The shift was expected due to the unit cell's thermal expansion. Upon closer examination, it became evident that the intensity of the silver diffraction peaks decreased alongside the shift. This effect was particularly noticeable for the (200) and (220) reflexes, as the (111) peak partially overlapped with the strong signal from the

tantalum sample holder. Comparing the intensity of these silver peaks with those of the reference sample, it became apparent that their intensity remained unchanged up to 600 °C. However, beyond this temperature, the intensity started to decline, and eventually, the obtained peaks became almost invisible, indicating the sublimation of silver.

Furthermore, all patterns showed sharp and narrow reflexes. No amorphous phase was present during the procedure, confirming that silver remained crystalline and no melting process occurred. These observations from the XRD experiments align perfectly with the earlier findings from the *in-situ* TEM heating experiments.

Rietveld analysis was performed to quantify the approximate amount of silver sublimated for every diffraction pattern obtained. Table 17 shows the mass loss of silver at every step of the experiment. In the end, it was found that 63% of the initial silver amount was sublimated (Fig. 78).

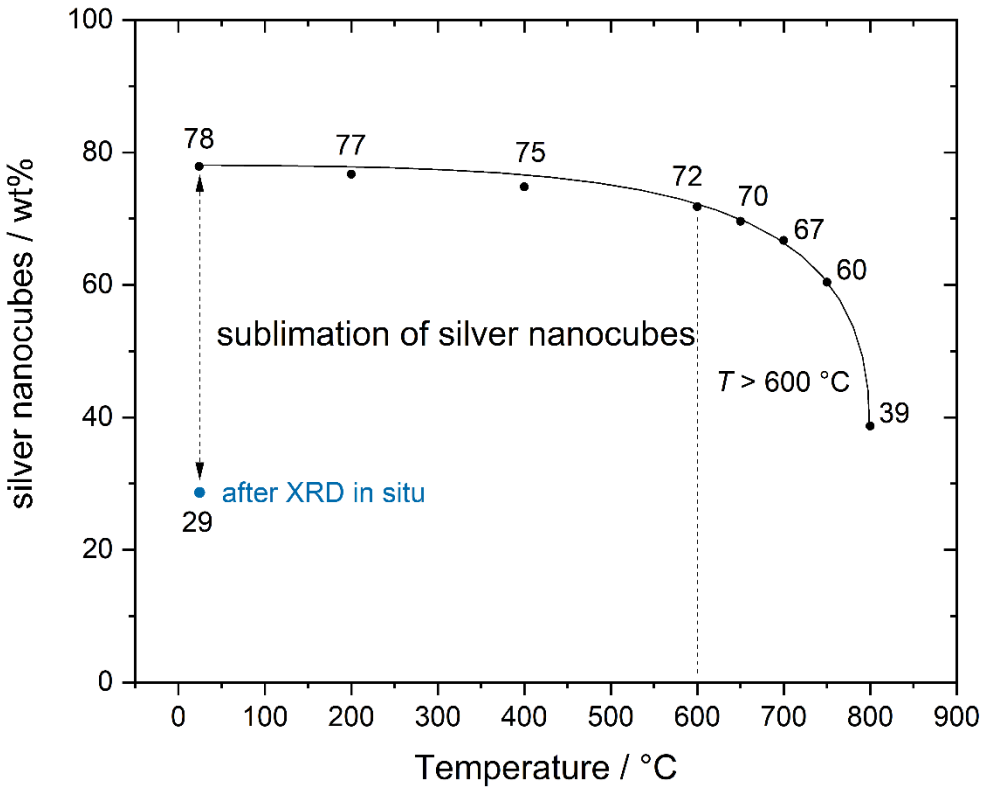

Figure 79. Temperature-dependent mass of silver nanocubes as derived from XRD after Rietveld refinement. Given is the mass ratios of silver to the standard LaB_6 (start: 22:78; after the heating: 71:29)

5.4.2 *In-situ* microscopy (SEM, TEM) and XRD heating experiments on silver-gold core-shell nanocubes

The silver-gold core-shell bimetallic nanocubes synthesized in this study were similar in size to the pure silver nanocubes subjected to heating electron microscopy and X-ray diffraction experiments.

Figure 80 (and video 2, Appendix 9.2) demonstrates a series of transmission electron microscopy images recorded at temperatures ranging from 25 and 900 °C. *In-situ* microscopy experiments revealed that as the temperature increased, the surface texture of the nanoparticles became smoother and more uniform. Additionally, between 400 and 500 °C, the pores within the silver core (lighter regions), resulting from partial dissolution during the formation of the gold shell through galvanic replacement, became filled, indicating atom mobility within the structure. In contrast to the silver nanocubes, which lost their morphology at lower temperatures, the silver-gold core-shell nanocubes maintained their shape up to 700 °C. However, in this case, the gradual rounding of the corners was still observed.

Complementary scanning electron microscopy *in-situ* experiments were conducted (video 3, Appendix 9.2) to investigate the nanocubes' behavior further. As depicted in Figure 81, EDS analysis was performed to determine the metal distribution on the nanoparticles at various temperatures. Line scanning was also conducted at each step to understand the nanocubes' composition better. The obtained EDS maps and line scans confirmed the preservation of the core-shell structure of the bimetallic nanocubes up to 400 °C. However, above this temperature, an alloying process was observed to take place. The increase in temperature induced the mobility of gold atoms. More specifically, it was observed that between 400 and 600 °C, gold atoms from the outer shell started moving towards the inner part of the nanocubes. This phenomenon, initially observed in TEM, was validated and could be attributed to the diffusion of gold atoms through the silver lattice. Consequently, as a result of the alloying process, alloyed nanostructures were formed within the nanocubes.[196, 206, 207]

This alloying process led to the gradual exposure of silver atoms on the surface of the particles, causing the sublimation of silver once again. After the evaporation of silver, the nanoparticles underwent significant morphological changes and completely lost their cubical shape. The outcome was leaving behind one gold nanoparticle originating from the small 10 nm gold nanoparticles that initially covered the silver nanocubes.

This aggregation of gold nanoparticles can be attributed to their tendecy to reduce their surface energy and stabilize themselves, forming larger structures.

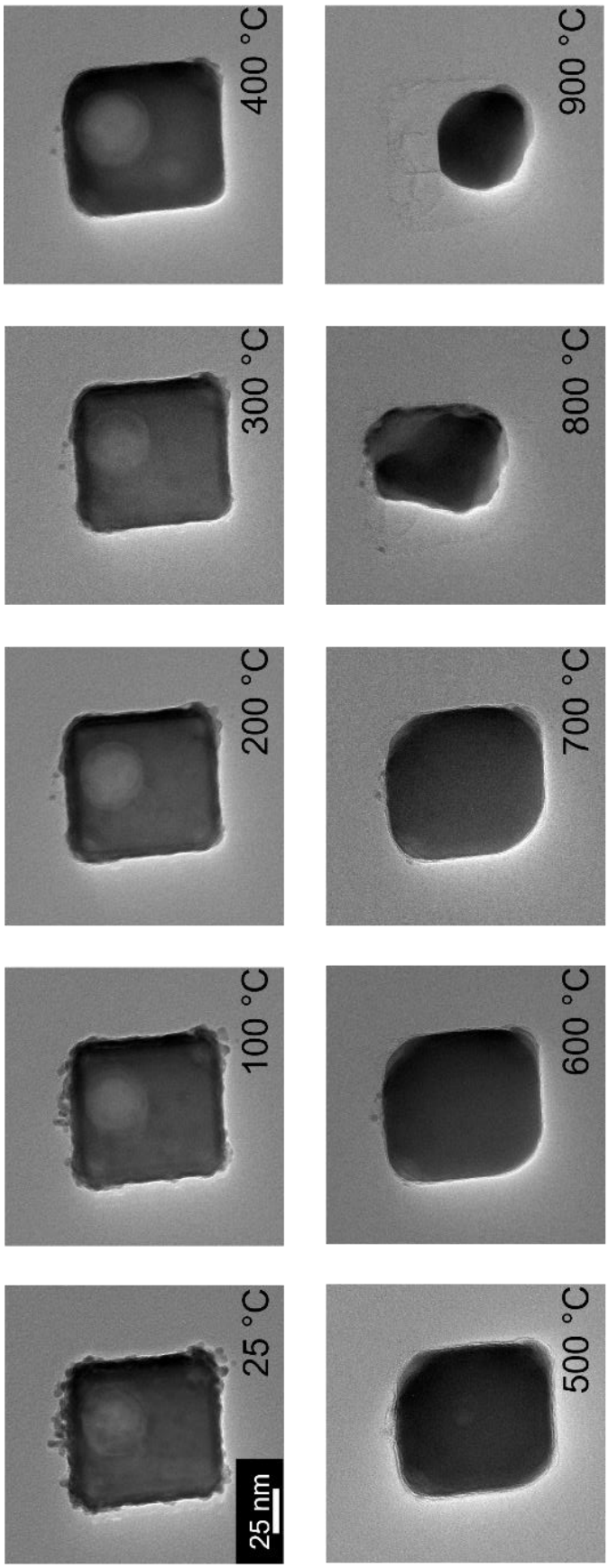

Figure 80. Bright field *in-situ* TEM images of a silver-gold core-shell nanocube during heating. Note the presence of an internal pore in the nanocube formed by galvanic replacement during synthesis that was gradually filled with gold diffusing from the surface during the *in-situ* experiment above 400 °C.

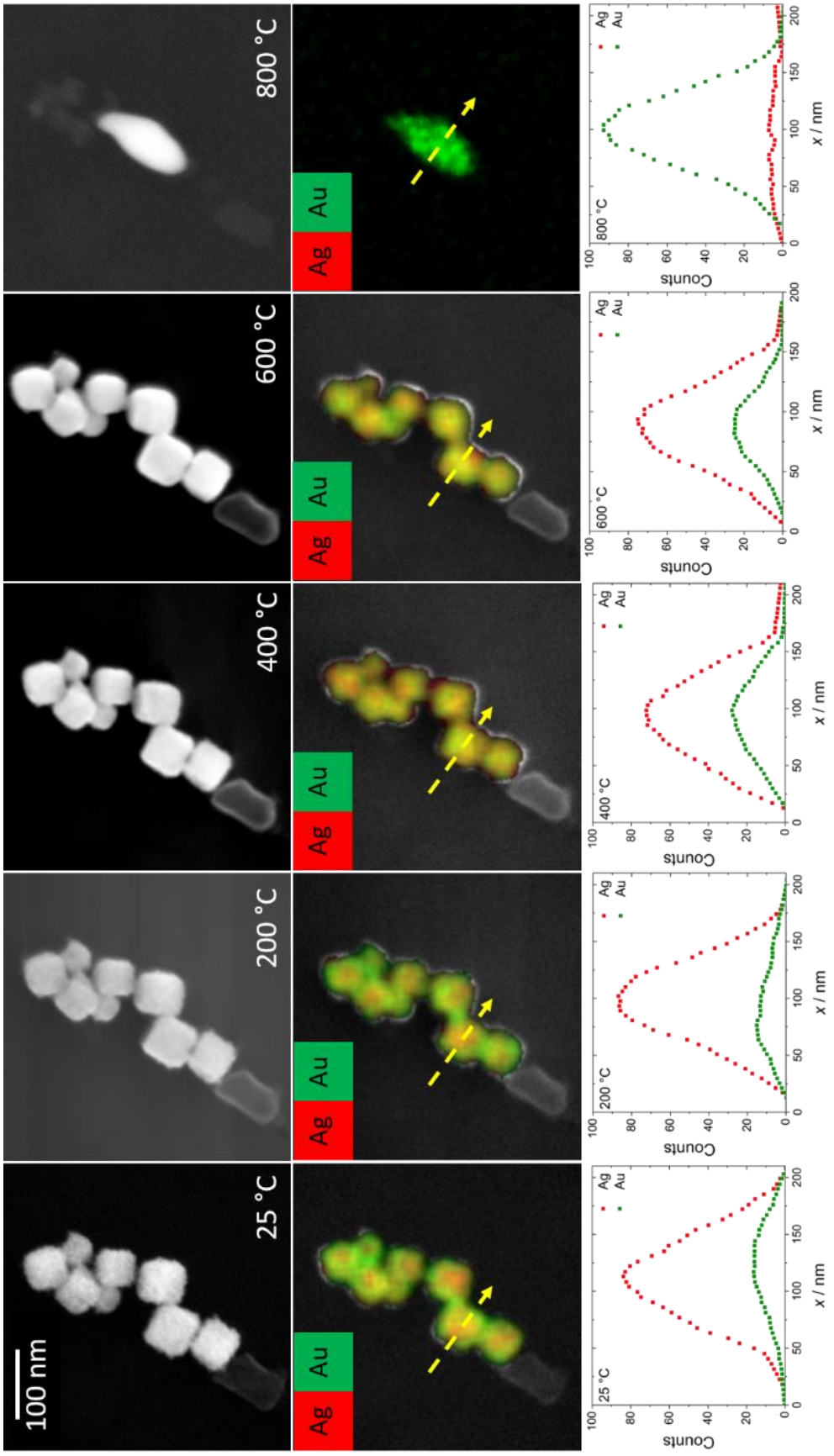

Figure 81. *In-situ* SEM images of silver-gold core-shell particles (top row), corresponding EDS maps (centre row), and EDS line scans of one particle (bottom row)

Figures 82 and 83 present a series of diffraction patterns obtained from *in-situ* X-ray powder diffraction experiments conducted on the silver-gold nanocubes in a high vacuum environment (10^{-3} Pa). These diffraction experiments further confirmed the observations during the corresponding SEM and TEM experiments.

Up to 600 °C, the (200) and (220) peaks shifted towards lower 2θ values, similar to what was observed in the silver nanocubes, indicating thermal expansion of the unit shell. The intensity of those peaks remained relatively unchanged during this temperature range. However, above 650 °C, a reverse shift towards higher 2θ values was observed, accompanied by a decrease in peak intensity. This “right” shift in peak position confirmed the alloying of silver and gold at temperatures above 650 °C, as observed in SEM experiments, and indicated a contraction of the lattice.

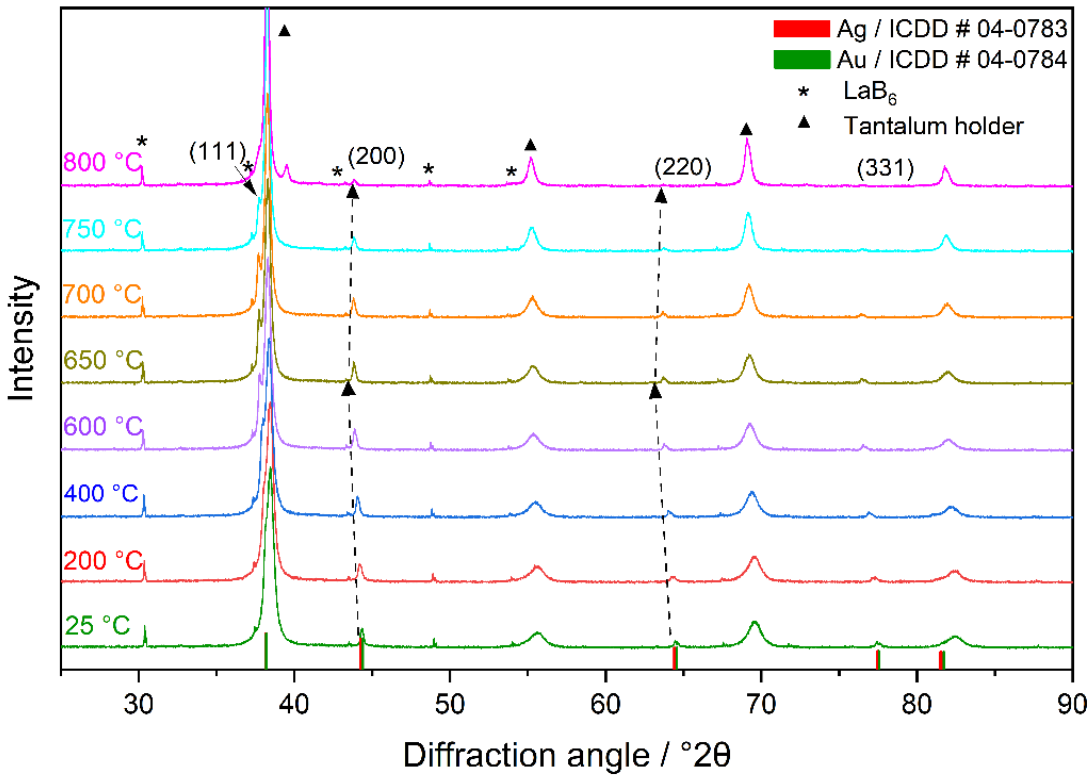

Figure 82. *In-situ* X-ray powder diffractograms of silver-gold core-shell nanocubes mixed with LaB_6 (marked with *) on a tantalum sample holder (marked with ▲). Miller indices of Ag and Au fcc phases are given in parentheses.

The gradual decrease in peak intensity was attributed to the sublimation of silver nanoparticles. In contrast to smaller alloyed silver-gold nanoparticles (8 nm), the larger nanoparticles studied in this experiment did not undergo structural relaxation due to recrystallization between 150 and 250 °C.[207] This observation, previously reported by Prymak *et al*., indicated that the larger nanoparticles maintained their crystalline structure throughout the heating procedure, confirming the formation of silver-gold core-shell nanoparticles with distinct phases for each metal.

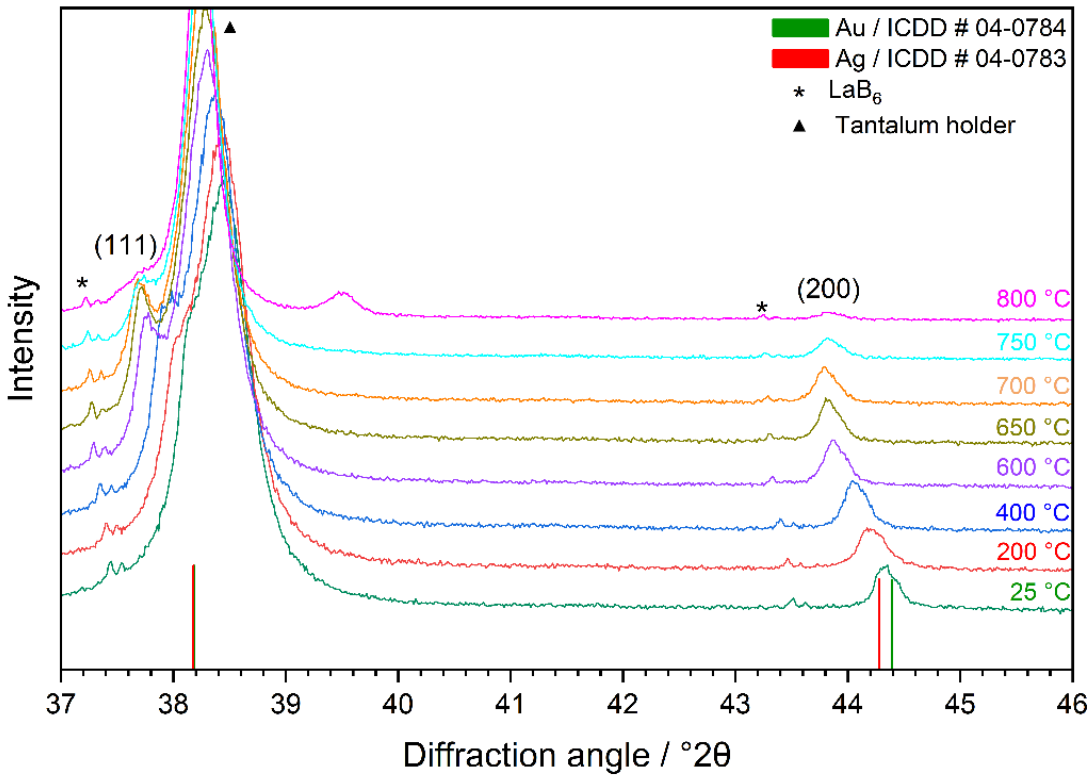

Figure 83. Enlargement of *in-situ* X-ray powder diffractograms from Figure 82, showing the (111) and (200) peaks of silver and gold.

The sublimation of silver is attributed to its higher vapor pressure compared to other noble metals such as Ru, Rh, Pd, Os, Ir, Pt, and Au.[208, 209] Due to their high specific area and free enthalpy; silver nanoparticles exhibited earlier sublimation than bulk silver when subjected to low-pressure conditions. However, whether this effect was a nanoscale phenomenon arose.

To investigate the behavior at the microscale, a control experiment was conducted using silver powder (Fig. 84) consisting of larger micro-particles (µ-powder). The micropowder was introduced to X-ray powder diffraction and examined *in-situ*, as the previously discussed samples.

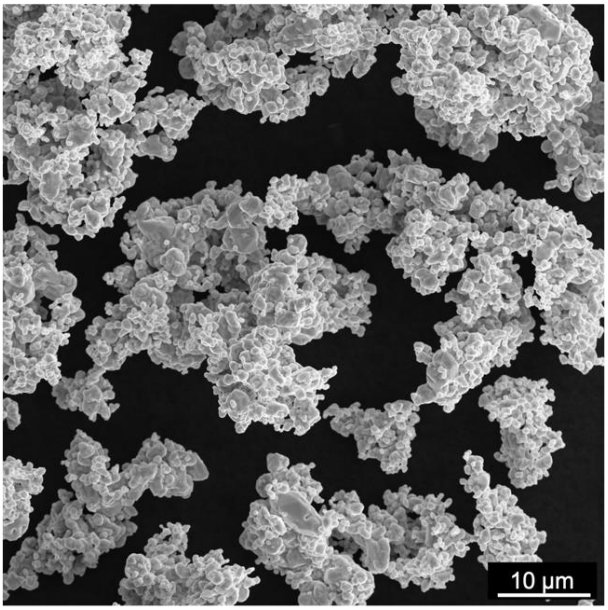

Figure 84. SEM image of silver powder containing micro-particles 5-8 µm.

A series of diffraction patterns taken at various temperatures were taken under high vacuum conditions, as depicted in Figure 85. Unlike the silver nanoparticles discussed earlier, which exhibited a strong and intense (200) peak due to their preferred orientation, the silver micropowder provided a typical diffraction pattern, characteristic of the fcc silver phase. The diffraction peaks appeared sharp and narrow, indicating a sample with high crystallinity. As the temperature increased, the diffraction peaks exhibited the expected shift towards lower 2θ values, reflecting the thermal expansion of the unit cell. Notably, a difference was observed in the behavior of the diffraction peaks among micropowder, silver, and silver-gold nanocubes. While the silver ones experienced a gradual decrease in intensity as the temperature increased, indicating the sublimation of silver, the powder's diffraction peaks remained unchanged throughout the entire experiment, indicating that microparticles did not undergo any sublimation.

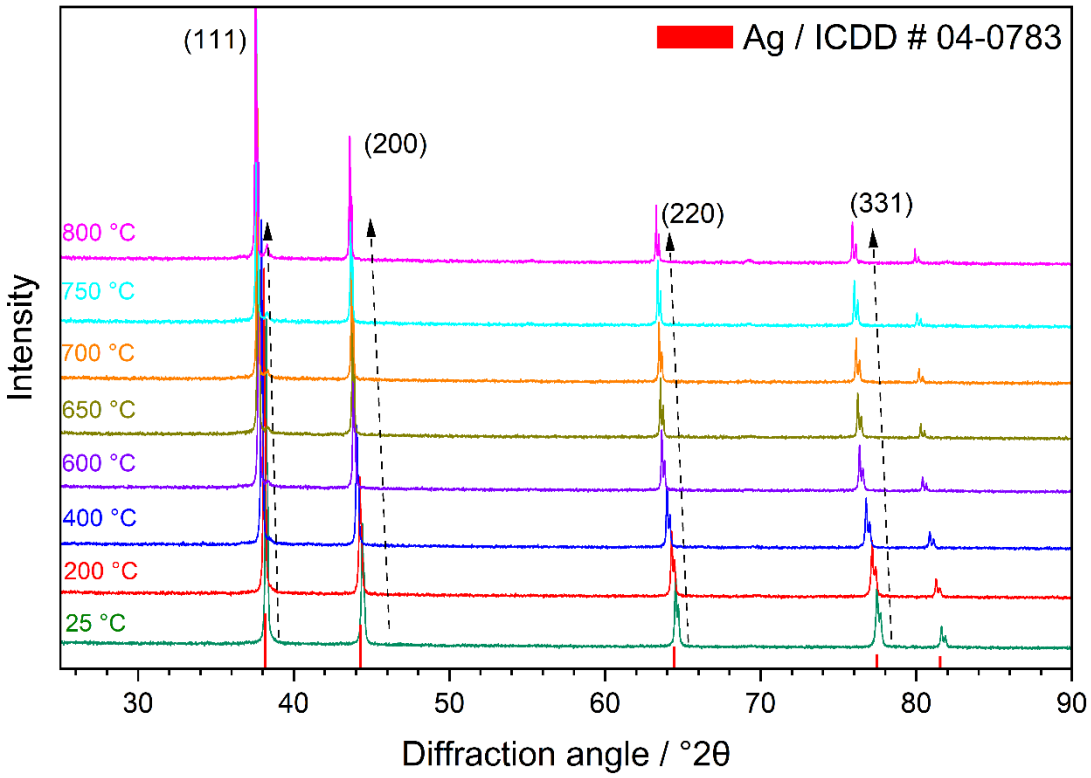

Figure 85. *In-situ* X-ray powder diffractograms of silver micropowder. Miller indices of Ag and Au fcc phases are given in parentheses.

Figure 86 depicts the temperature dependence of the lattice parameter *a* for all samples investigated, including the previously *in-situ* examined silver and gold nanospheres, as a comparison.

The lattice parameter of the silver nanocubes (green), silver nanospheres[207] (35 nm, red), and silver µ-powder (pink) exhibited an almost identical linear increase with the temperature. Despite the bimetallic nature of the silver-gold nanocubes (black), the small amount of gold covering the silver nanocubes has a negligible impact on the calculated lattice parameter of the silver. Therefore, the lattice parameter of silver-gold nanocubes initially followed the same trend as that of the silver nanoparticles. However, a gradual deviation toward lower lattice parameters was observed as the temperature rose. This deviation indicated the diffusion of gold atoms from the surface of the nanocubes, resulting in the alloying of gold with the silver core.

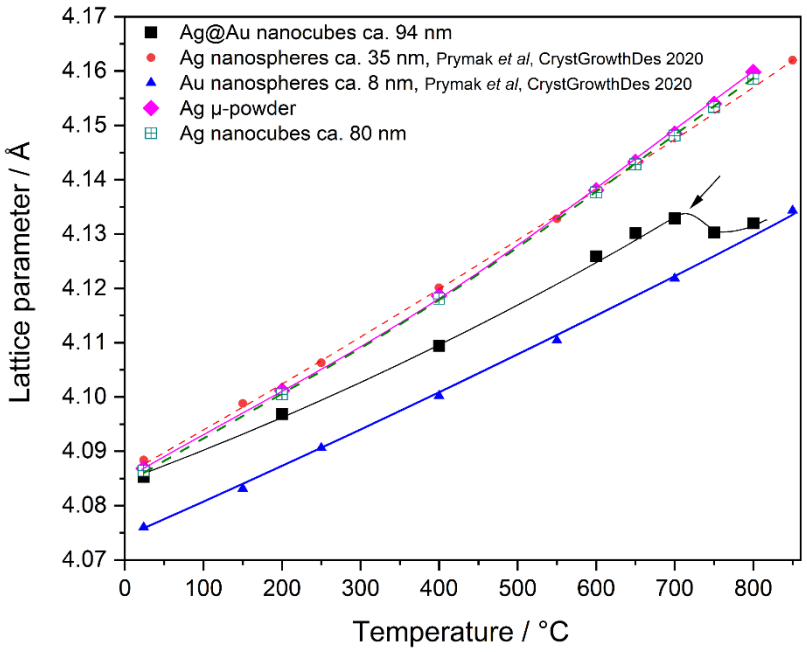

Figure 86. Temperature-dependent lattice parameter *a* of silver nanospheres (35 nm), silver nanocubes, silver microparticles, silver-gold core-shell nanocubes, and gold nanospheres (8 nm)[207].

The sudden drop of the lattice parameter values at approximately 700 °C confirmed the sublimation of silver, leaving behind only the gold part. After this point, the lattice parameters matched those of pure gold nanospheres (8 nm, blue)[207], as gold does not undergo sublimation under these experimental conditions. [210]

5.4.3 *Ex-situ* experiments on silver nanoparticles

In this work, silver spherical nanoparticles were synthesized and fully characterized. *Ex-situ* X-ray powder diffraction experiments were conducted to investigate whether the sublimation of silver nanoparticles is solely dependent on vacuum and temperature. Instead of silver nanocubes, silver nanospheres were chosen to be examined. This choice was made due to the similarity in the lattice parameter trends (comparable to those of silver nanocubes) during *in-situ* examination (Fig. 86).

For these experiments, a customized quartz sample holder was used. The lyophilized sample was evenly distributed on the holder to ensure uniformity. The first diffraction measurement was conducted at room temperature as the initial reference point. Subsequently, the sample-loaded holder was placed in a muffle furnace and heated at a rate of 5 K min^{-1} until reaching a temperature of up to 200 °C. Before and after each heating step, the mass of the sample was carefully recorded to monitor any changes. This procedure was repeated incrementally, with measurements taken at 200 °C intervals up to a final temperature of 800 °C.

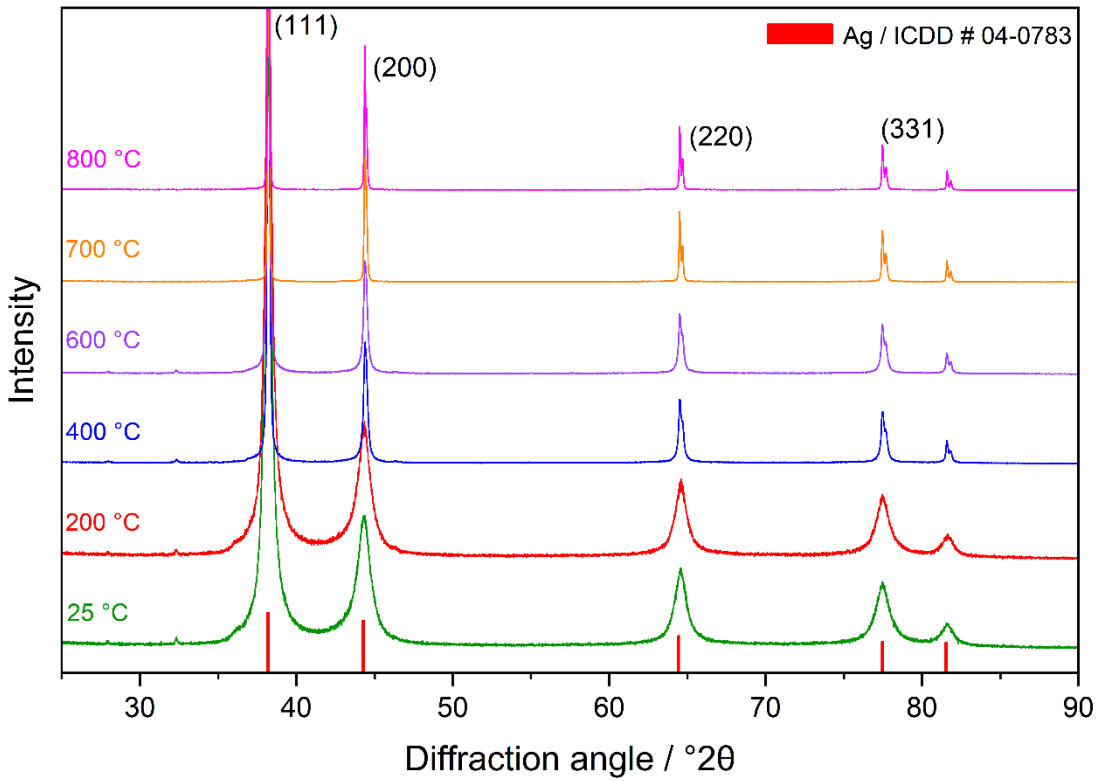

Figure 87. *Ex-situ* X-ray powder diffractograms of silver nanospheres. Miller indices of Ag phases are given in parentheses.

The obtained diffraction patterns are presented in Figure 87, exhibiting the characteristic reflections of the pure silver fcc phase. However, compared to the diffraction patterns of the cubical nanoparticles discussed earlier, the signals obtained at 25 °C appear relatively wider. This broadening can be attributed to their smaller size of spherical nanoparticles and the smaller crystallite size. The five-fold twinned decahedral structures that silver forms, consisting of several domains and defects, have already been extensively studied in the literature.[159, 211-213]

As the temperature increased, a noticeable transformation occurred in the diffraction patterns. The reflexes became sharper and narrower due to continuous crystallization. Throughout the experiment, no loss in peak intensity was observed, suggesting that when the silver nanoparticles were heated under no vacuum condition, they did not undergo sublimation. Table 18 shows the mass loss measured after each heating cycle, as well as the calculated lattice parameter *a* and crystallite size (CS) determined through Rietveld analysis performed at each step.

Table 18. Sample mass after every heating cycle (5 K min^{-1}), lattice parameter, and crystallite size obtained from Rietveld refinement for each heating step.

T / °C	$m_{(Q + Ag)}$ / g	m_{Ag} / mg	Mass loss (%)	a_{Ag} / Å	CS_{Ag} / nm
25	1.1371	6.7	0	4.089 (1)	15 (1)
200	1.1371	6.7	0	4.090 (1)	16 (1)
400	1.1368	6.4	- 4.5	4.085 (1)	78 (1)
600	1.1369	6.5	- 3.0	4.085 (1)	80 (1)
700	1.1362	5.8	- 13.4	4.085 (1)	336 (4)
800	1.1380	7.6	+ 13,4	4.084 (1)	436 (6)

mass of quartz sample holder, m_Q= 1.1304 g, *mass of quartz sample holder and sample* m_{Q+Ag} = 1.371 g, *mass of sample* m_{Ag}= 6.7mg

Up to 700 °C, a total mass sample loss of 13.4% was observed. This mass loss could be attributed to the melting or decomposition of the stabilizing agent, PVP. The calculated lattice parameter at each step matched very well with the theoretical value, confirming the stability of the crystal structure throughout the heating process. As for the crystallite size, the initial size obtained at 25 and 200 °C, approximately 15 nm, corresponds to about 1/3 of the silver nanospheres' particle size (35 nm), confirming

their polycrystalline nature. Above 200 °C, a continuous recrystallization process occurred, as indicated by the increasing crystallite size values with increasing temperature (Fig. 88).

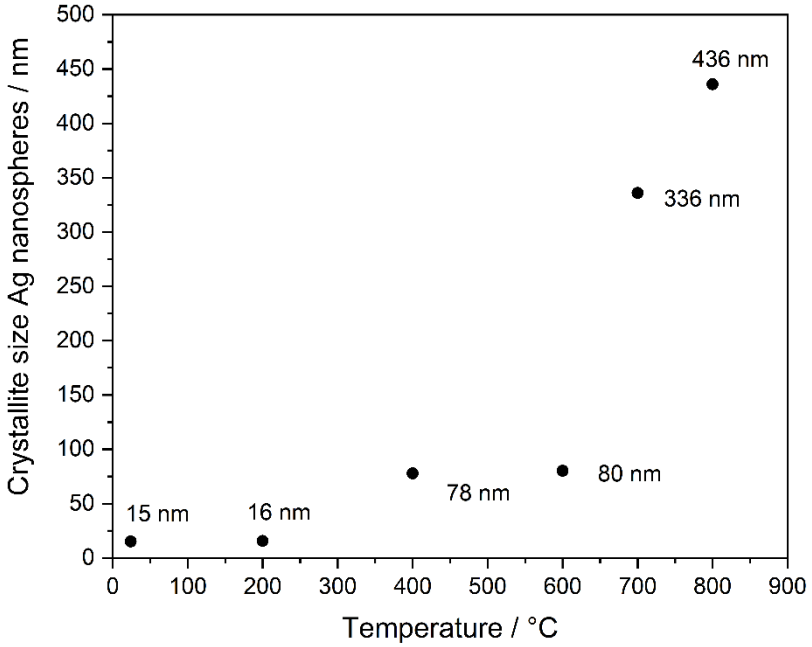

Figure 88. Temperature-dependent diagram crystallite size during the ex-situ XRD heating experiments. A gradual increase in size was observed during the heating process.

At 800 °C, an unexpected increase in mass was observed, which may potentially be attributed to experimental error or external factors influencing the measurements. For instance, contamination could occur during the transportation of the sample between the muffle furnace and the diffractometer. Even during the heating procedure, the muffle furnace itself could be a source of contamination leading to misleading mass measurements. The calculated lattice parameter, as well as the crystallite size calculated at 800 °C, did not, however, suggest any unexpected structural change of silver.

A control experiment was conducted to investigate potential sources of error and exclude the possibility of mass gain originating from the sample holder. Another quartz sample holder, lacking any sample, was subjected to the same heating procedure up

to 800 °C. The mass of the empty holder was recorded before and after heating, revealing no indication of mass gain or other significant changes.

To confirm whether the observed mass loss is attributed to the decomposition of the stabilizing agent, PVP, thermogravimetric analysis (TGA) was conducted. Figure 89 shows the obtained TGA diagram, which provides information on weight loss as a function of temperature.

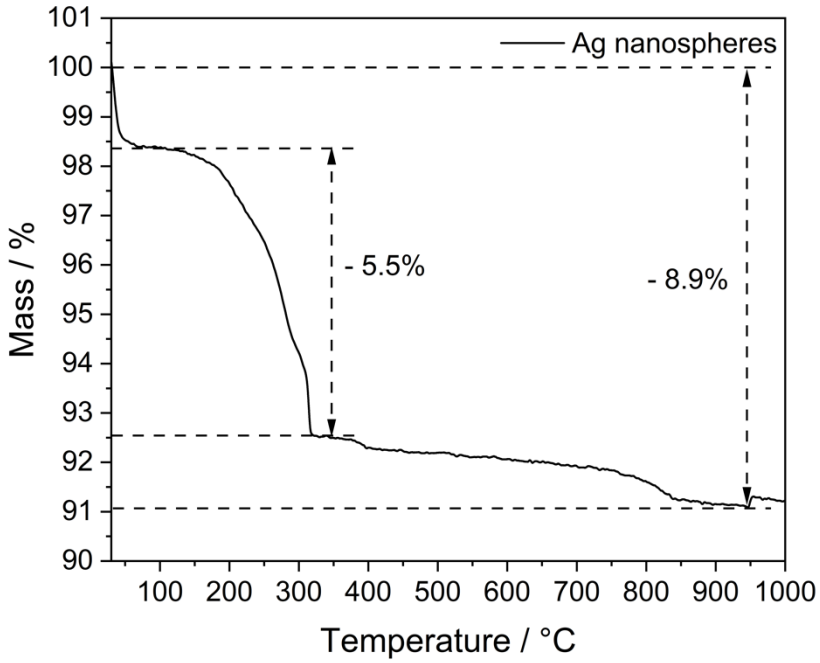

Figure 89. Thermogravimetric analysis of 35 nm silver nanospheres stabilized with PVP_{40} in O_2 atmosphere.

The TGA curve displayed a weight loss of approximately 5.5% starting at around 150 °C, corresponding to the decomposition temperature of PVP. The decomposition of pure PVP normally starts at 380 °C; however, it was reported that when nanoparticles are coated with PVP, its decomposition can occur at lower temperatures.[214] Additionally, a further mass loss of roughly 1,5% was observed until the end of the experiment.

The additional weight loss can also be attributed to the residual PVP, as indicated by the TGA curve of pure PVP_{40} (Fig. 90). The decomposition started approximately at 350 °C, as expected. Between 500 and 600 °C, approximately 87% of the initial

amount of PVP was decomposed while the rest of the polymer decomposed gradually up to 900 °C.

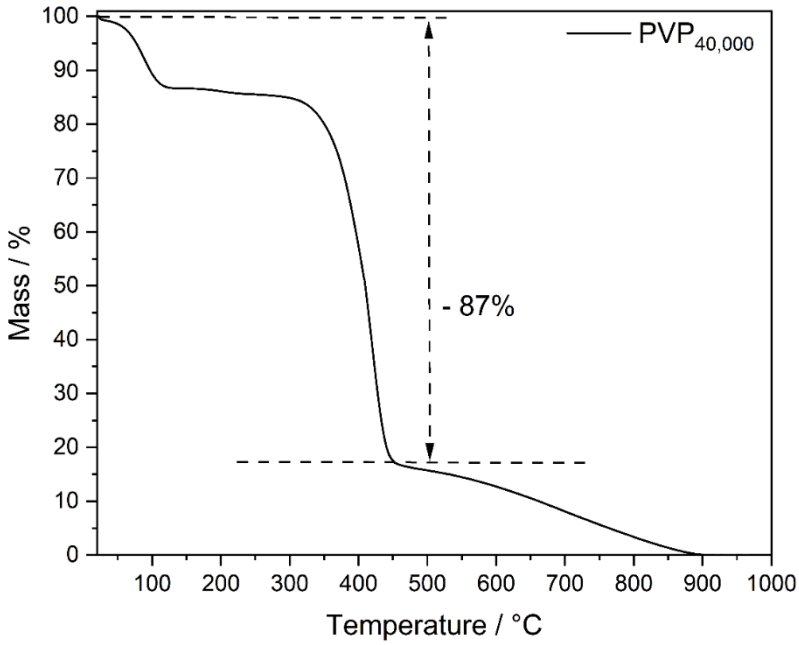

Figure 90. TGA analysis of pure PVP with a molecular weight of 40,000 g mol^{-1}, which was used for the stabilization of Ag nanospheres in O_2 atmosphere.

This observation confirmed the suggestion that the mass loss seen in the XRD experiments can be attributed to the decomposition of the capping agent rather than the sublimation of silver nanoparticles. Additional TGA experiments were conducted to compare the thermal behavior of different silver particles, including nanocubes, micro particles (µ-powder), and bulk silver foil.

As expected, the silver foil showed no significant change in mass throughout the heating process (Fig. 91A). The microparticles exhibited a minimal mass loss of approximately 1%, which can be attributed to the presence of PVP as a stabilizing agent (Fig. 91B). Similarly, the silver nanocubes showed a noticeable mass loss at around 300 °C, indicating the decomposition of the stabilizing agent, PVP (Fig. 91C). However, the subsequent mass changes were negligible after this initial mass loss. These findings suggest that there was no sublimation of silver during the heating of silver nanoparticles under ambient conditions.

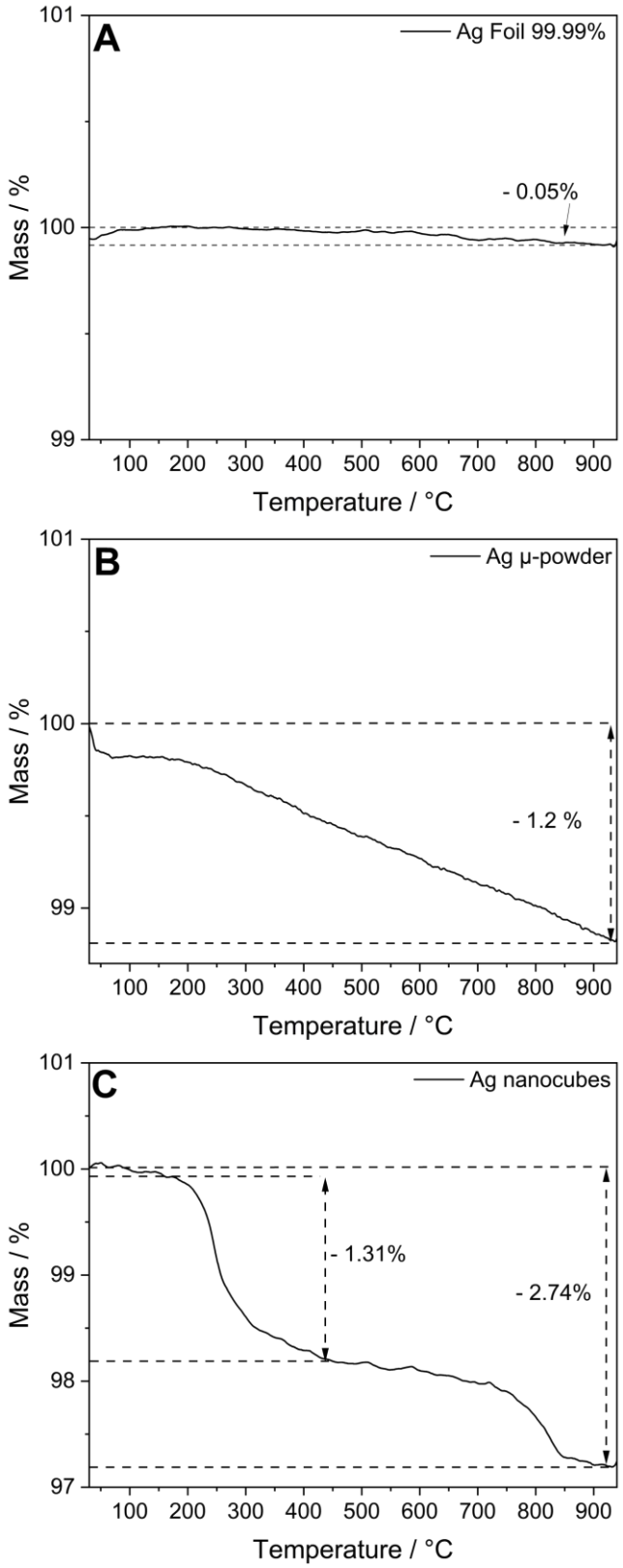

Figure 91. Thermogravimetric analysis of Ag foil (bulk material) (A), Ag microparticles (5-8 µm) stabilized with PVP (B) and Ag nanocubes (85 nm), stabilized with PVP (C), in O_2 atmosphere.

6. CONCLUSIONS – SUMMARY

This study focused on creating nanoparticles of mono- and bimetallic noble metals (Ag, Au, Pd, Pt) with specific shapes and analyzing them using various methods such as spectroscopy, microscopy, and diffraction.

Silver nanoparticles, approximately 35 nm in size, with a quasi-spherical shape and plasmonic behavior, were successfully synthesized via the reduction of silver nitrate by glucose in water. These nanoparticles had a five-fold twinned crystalline structure and could explain the deformation from a perfect spherical shape.

Silver nanowires were synthesized through a polyol-based method involving the reduction of metal salt in the presence of a stabilizing agent, ethylene glycol (polyol method). The process allowed for anisotropic silver nanoparticles. The method utilized silver chloride seeds formed *in-situ*, which grew into nanowires through a seed-and-growth approach. PVP and NaCl influenced the resulting morphology by inhibiting certain facets, leading to elongated nanowires with five-fold symmetry. The anisotropic morphology of the nanowires gave rise to interesting optical properties, as observed in the UV-Vis spectrum with two maxima at 348 nm and 379 nm, corresponding to different surface plasmons. SEM images revealed uniform-width nanowires with an average width of 74 ± 15 nm and a length of 15 µm. However, determining the hydrodynamic radius through DLS was problematic due to their anisotropic shape and high length. The synthesized nanowires showed electrosteric stabilization. PXRD confirmed the phase purity and crystallinity, confirming the absence of AgCl seeds used as templates for growth.

Silver nanocubes stabilized with PVP were prepared using a modified polyol process with oxidative etching. The synthesis was successfully optimized and provided nanocubes with slightly rounded corners and smooth surfaces, with an average edge length of 85 nm. Various tests showed that they were colloidally stable, with a hydrodynamic diameter of around 107 nm and a negative ζ-potential of -41 mV. They were also found to be single crystalline structures with a [001] orientation and exhibited characteristic reflections of the fcc phase of metallic silver. These synthesized nanoparticles were used for further core-shell syntheses and *in-situ* heating experiments.

Palladium nanoparticles were synthesized using ascorbic acid in water, resulting in 18 nm nanoparticles with well-defined shapes enclosed by (100) facets. The nanoparticles were thoroughly characterized using various methods, including UV-Vis, DLS, DCS, STEM, and PXRD, to determine their size, structure, and stability. By adjusting the amount of etching agent KBr during synthesis, a correlation was observed between bromide ion concentration and nanoparticle size, with decreasing concentrations resulting in smaller nanoparticles. The synthesis produced monodisperse, colloidal stable cubical nanoparticles, demonstrating the controllability of nanoparticle size. When using different lengths of capping agent (PVP), no significant changes in morphology and size were observed, but additional shapes, such as rods and pyramids, were generated. Through a seed-and-growth approach, the 18 nm palladium nanoparticles were used as seeds to generate larger, approximately 45 nm nanoparticles, which maintained their monodispersity and single-crystalline nature. The growth mechanism was examined by analyzing samples collected at different intervals, revealing a relatively fast growth rate in the first 7 hours of synthesis, resulting in octahedral structures. The growth rate then gradually decreased, but the nanoparticles regained their cubic shape, resulting after 24 hours to the final products.

The synthesis of noble metal core-shell structures presents a challenge due to the galvanic replacement reactions that occur between metals with varying electrochemical potentials. The reaction between silver nanoparticles and gold ions could easily lead to the creation of hollow nanostructures. After careful consideration of various parameters, such as the molar ratio of the two metals, solution pH level, temperature, precursor concentration, and addition rate, a reliable and reproducible synthesis was developed. The optimal conditions resulted in the creation of 96 nm core-shell silver-gold nanocubes with a nominal composition of 75% silver and 25% gold, and a complete formation of a gold shell around the silver nanocubes. Through TEM and PXRD, it was confirmed that small, 10 nm gold nanoparticles were deposited on the surface of the silver cubes, while EDS mapping showed the precise distribution of the two metals, thereby confirming the core-shell nature of the particles. Further, TEM and PXRD experiments were conducted using Ag@Au nanocubes for *in-situ* heating.

Through a seed-mediated approach utilizing the galvanic replacement reaction, 100 nm platinum nanocages were successfully synthesized. The absence of LSPR peaks in the UV-Vis spectrum indicated the formation of a platinum shell. SEM and TEM imaging confirmed the complete dissolution of silver nanocubes and the formation of nanocages or other platinum nanoparticles. The platinum shell exhibited a thickness of approximately 10 nm. EDS analysis validated the platinum-rich composition, revealing a molar ratio of 95:5 for platinum to silver. TEM images further revealed that the shell consisted of 2 nm platinum nanoparticles, forming a compact frame structure.

Palladium-platinum core-shell structures were also generated through a seed-and-growth method. Cubic nanoparticles with slightly rounded edges and corners, with an average edge length of approximately 21 nm, and a nominal composition of palladium to platinum 90:10 were successfully synthesized. TEM images provided evidence of the successful formation of bimetallic core-shell palladium-platinum nanostructures. The similar lattice constants of platinum and palladium allowed epitaxial deposition of platinum on the palladium seeds. However, the partial dissolution of the palladium core led to the formation of concave nanostructures. Further optimization of synthesis parameters may allow better control of the final shell thickness of the nanoparticles.

In-situ heating microscopy and diffraction experiments were carried out to assess the thermal behavior of silver nanocubes and silver-gold core-shell nanocubes. The silver nanocubes exhibited stability up to 600 °C, maintaining their cubic shape, but above 600 °C, the corners rounded off, forming truncated octahedra. Above 700 °C, the silver nanocubes lost their morphology and underwent sublimation. Silver-gold core-shell nanocubes also maintained their shape up to 700 °C and underwent an alloying process above 400 °C, followed by sublimation of silver, resulting in morphological changes. XRD showed that no melting process had occurred, as the nanoparticles remained crystalline throughout the whole experiment. *Ex-situ* experiments on silver nanospheres showed no sublimation when heated under ambient conditions. Instead, the mass loss observed was attributed to the decomposition of the stabilizing agent, PVP.

7. GERMAN SUMMARY – ZUSAMMENFASSUNG

Die vorliegende Arbeit umfasst die Synthese und Charakterisierung von mono- und bimetallischen Nanopartikeln, die aus den Edelmetallen Ag, Au, Pd und Pt mit spezifischen Formen hergestellt und mittels verschiedener spektroskopischer und mikroskopischer Methoden sowieso Röntgenbeugung analysiert wurden.

Durch eine Polyol basierte Synthese, bei der in Gegenwart eines stabilisierenden Liganden ein Metallsalz mittels Ethylenglykols reduziert wurde, konnten Silbernanopartikel mit einer stäbchenförmigen Morphologie dargestellt werden. Bei der Herstellung der Partikel wurden in-situ gebildete Silberchlorid-Keime verwendet, die sich durch eine *seed-and-growth* Methode bildeten. Indem PVP und NaCl das Wachstum bestimmter Kristallflächen hemmten, wurde die Bildung von stäbchenförmigen Nanopartikeln mit fünffacher Symmetrie begünstigt. Die anisotrope Morphologie der Nanostäbchen führte zu interessanten optischen Eigenschaften. Folglich konnten in der UV-Vis-Spektroskopie zwei Maxima bei 348 nm und 379 nm beobachtet werden, die verschiedenen Oberflächenplasmonen entsprachen. SEM-Bilder zeigten Nanostäbchen mit einer durchschnittlichen Breite von 74 ± 15 nm und einer Länge von 15 µm. Die Bestimmung des hydrodynamischen Radius mittels DLS war aufgrund der anisotropen Form und Länge der Partikel problematisch. Die synthetisierten Nanostäbchen zeigten eine elektrosterische Stabilisierung. Durch die Abwesenheit der als *seeds* verwendeten AgCl-Keimen konnte über PXRD die Phasenreinheit und Kristallinität bestätigt werden.

PVP stabilisierte Silber-Nanowürfel wurden mittels eines modifizierten Polyol-Verfahrens mit oxidativem Ätzen hergestellt. Die Synthese konnte erfolgreich modifiziert werden und lieferte Nanowürfel mit leicht abgerundeten Ecken und glatten Oberflächen sowieso einer durchschnittlichen Kantenlänge von 85 nm. Verschiedene Methoden zeigten, dass die Silber-Nanowürfel mit einem hydrodynamischen Durchmesser von etwa 107 nm und einem negativen Zetapotential -41 mV kolloidal stabil waren. Die Partikel wiesen eine einkristalline Struktur mit einer [001]-Orientierung auf und zeigten charakteristische Reflexe der fcc-Phase von metallischem Silber. Diese wurden anschließend für weitere Core-Shell-Synthesen und *in-situ*-Heizexperimente verwendet.

Palladium-Nanopartikel wurden unter Verwendung von Ascorbinsäure in Wasser dargestellt. Sie zeigten klar definierten Formen, umschlossen von (100)-Flächen,

sowieso eine durchschnittliche Größe von 18 nm. Die Charakterisierung erfolgte mittels UV-Vis, DLS, DCS, STEM und PXRD. Durch die Anpassung der Menge des Ätzmittels KBr während der Synthese wurde eine Korrelation zwischen der Bromidionenkonzentration und der Nanopartikelgröße beobachtet, wobei eine Abnahme der Br^- Konzentration zu kleineren Nanopartikeln führte. Die Synthese lieferte monodisperse, kolloidal stabile, kubische Nanopartikel und demonstrierte somit die Kontrollierbarkeit der Nanopartikelgröße. Bei Verwendung unterschiedlicher Längen des Liganden PVP wurden keine signifikanten Veränderungen der Morphologie und Größe beobachtet, jedoch kam es zur Bildung von weiteren Morphologien wie Stäbchen und Pyramiden. Durch den Einsatz von 18 nm großen Palladium-Nanopartikel als *seeds* bei einem *seed-and-growth* Methode wurden Partikel mit einer Größe von 45 nm erzeugt, die ihre Monodispersität und einkristalline Natur beibehielten. Der Wachstumsmechanismus wurde analysiert, indem Proben zu verschiedenen Zeitpunkten während der Synthese entnommen wurden. Es zeigte sich eine schnelle Wachstumsrate in den ersten sieben Stunden, wobei die Bildung von oktaedrischen Strukturen beobachtet werden konnte. Danach nahm ihre Wachstumsrate langsam ab. Die Nanopartikel erlangten nach 24 Stunden ihre kubische Form wieder.

Die Synthese von Edelmetall-Core-Shell-Strukturen stellt eine Herausforderung dar, da Opferanodeneffekt zwischen Metallen mit unterschiedlichen elektrochemischen Potenzialen auftreten. Die Reaktion zwischen Silbernanopartikeln und Gold-Ionen könnte leicht zur Bildung hohler Nanostrukturen führen. Nach sorgfältiger Berücksichtigung verschiedener Parameter während der Synthesen wie dem molaren Verhältnis der beiden Metalle, dem pH-Wert der Lösung, der Temperatur, der Präkursorkonzentration und der Zugabegeschwindigkeit wurde eine zuverlässige und reproduzierbare Synthese entwickelt. Die optimalen Bedingungen führten zur Bildung von 96 nm großen Core-Shell Silber-Gold-Nanowürfeln mit einer nominellen Zusammensetzung von 75 % Silber und 25 % Gold, wobei eine vollständige Goldschale um die Silbernanowürfel zu sehen war. Mithilfe von TEM und PXRD wurde bestätigt, dass sich kleine, 10 nm große Goldnanopartikel auf der Oberfläche der Silberwürfel anlagerten, während EDS-Mapping die genaue Verteilung der beiden Metalle zeigte und somit die core-shell-Struktur der Partikel bestätigte. Weitere TEM- und PXRD-Experimente wurden mit Ag@Au-Nanowürfeln für In-situ-Experimente durchgeführt.

Durch einen seed Ansatz unter Verwendung der Opferanodeneffekt wurden erfolgreich 104 nm große Platin-Nanokäfige synthetisiert. Das Fehlen von LSPR-Peaks im UV-Vis-Spektrum deutete auf die Bildung einer Platinhülle hin. SEM- und TEM-Bilder bestätigten die vollständige Auflösung der Silbernanowürfel und die Bildung von Nanokäfigen oder anderen Platin-Nanopartikeln. Die Platinhülle besaß eine Dicke von etwa 10 nm. Die Analyse mittels EDS zeigte eine platinreiche Zusammensetzung mit einem molaren Verhältnis von 95:5 für Platin zu Silber. Durch TEM-Aufnahmen konnte eine kompakte Hülle aus ultrakleinen Platin-Nanopartikeln mit einem Durchmesser von 2 nm bestätigt werden.

Auch Palladium-Platin Core-Shell-Strukturen wurden mithilfe eines *seed-and-growth* Ansatzes erzeugt. Dabei konnten kubische Nanopartikel mit leicht abgerundeten Kanten und Ecken sowie einer durchschnittlichen Kantenlänge von 21 nm und einer Zusammensetzung von Palladium zu Platin von 90:10 erfolgreich synthetisiert werden. TEM-Aufnahmen lieferten Beweise für die erfolgreiche Bildung bimetallischer Core-Shell Palladium-Platin-Nanostrukturen. Aufgrund der ähnlichen Gitterkonstanten von Platin und Palladium konnte eine konforme Abscheidung ermöglicht werden, welche zu epitaktischem Wachstum von Platin auf den Palladium-Würfeln führte. Die partielle Auflösung des Palladium-Kerns resultierte jedoch in der Bildung konkaver Nanostrukturen. Eine weitere Optimierung der Syntheseparameter könnte eine bessere Kontrolle der endgültigen Schalendicke der Nanopartikel ermöglichen.

Um das thermische Verhalten dieser Nano-Systeme zu untersuchen wurden *in-situ* REM- und XRD-Experimente an Silber-Nanowürfeln und Silber-Gold Core-Shell-Nanowürfeln durchgeführt. Die Silber-Nanowürfel waren bis 600 °C stabil und behielten ihre kubische Form bei, jedoch rundeten sich oberhalb von 600 °C die Ecken ab und es bildeten sich abgeschnittene Oktaeder. Oberhalb von 700 °C verloren die Silbernanowürfel ihre Morphologie und sublimierten. Die Silber-Gold Core-Shell-Nanowürfel behielten bis zu 700 °C ihre Form und durchliefen oberhalb von 400 °C einen Legierungsprozess, gefolgt von der Sublimation von Silber, was zu morphologischen Veränderungen führte. Durch XRD-Messungen konnte ein Schmelzprozess ausgeschlossen werden, da die Nanopartikel während des gesamten Experiments kristallin blieben. Ex-situ-Experimente an Silbernano-sphären zeigten keine Sublimation während der Erhitzung unter Umgebungsbedingungen. Die

beobachtete Massenabnahme wurde stattdessen auf die Zersetzung des Stabilisierungsmittels PVP zurückgeführt.

8. REFERENCES

1. Arblaster, J.W., *Crystallographic properties of palladium.* Platinum Metals Review, **2012**. 56(3): p. 181-189.
2. Pelaz, B.,Alexiou, C.,Alvarez-Puebla, R.A.,Alves, F.,Andrews, A.M.,Ashraf, S.,Balogh, L.P.,Ballerini, L.,Bestetti, A.,Brendel, C.,Bosi, S.,Carril, M.,Chan, W.C.W.,Chen, C.,Chen, X.,Chen, X.,Cheng, Z.,Cui, D.,Du, J.,Dullin, C.,Escudero, A.,Feliu, N.,Gao, M.,George, M.,Gogotsi, Y.,Grünweller, A.,Gu, Z.,Halas, N.J.,Hampp, N.,Hartmann, R.K.,Hersam, M.C.,Hunziker, P.,Jian, J.,Jiang, X.,Jungebluth, P.,Kadhiresan, P.,Kataoka, K.,Khademhosseini, A.,Kopeček, J.,Kotov, N.A.,Krug, H.F.,Lee, D.S.,Lehr, C.-M.,Leong, K.W.,Liang, X.-J.,Ling Lim, M.,Liz-Marzán, L.M.,Ma, X.,Macchiarini, P.,Meng, H.,Möhwald, H.,Mulvaney, P.,Nel, A.E.,Nie, S.,Nordlander, P.,Okano, T.,Oliveira, J.,Park, T.H.,Penner, R.M.,Prato, M.,Puntes, V.,Rotello, V.M.,Samarakoon, A.,Schaak, R.E.,Shen, Y.,Sjöqvist, S.,Skirtach, A.G.,Soliman, M.G.,Stevens, M.M.,Sung, H.-W.,Tang, B.Z.,Tietze, R.,Udugama, B.N.,Vanepps, J.S.,Weil, T.,Weiss, P.S.,Willner, I.,Wu, Y.,Yang, L.,Yue, Z.,Zhang, Q.,Zhang, Q.,Zhang, X.-E.,Zhao, Y.,Zhou, X., Parak, W.J., *Diverse applications of nanomedicine.* ACS Nano, **2017**. 11(3): p. 2313-2381.
3. Mistry, H.,Varela, A.S.,Kühl, S.,Strasser, P., Cuenya, B.R., *Nanostructured electrocatalysts with tunable activity and selectivity.* Nature Reviews Materials, **2016**. 1(4): p. 1-14.
4. Abalde-Cela, S.,Carregal-Romero, S.,Coelho, J.P., Guerrero-Martínez, A., *Recent progress on colloidal metal nanoparticles as signal enhancers in nanosensing.* Advances in colloid and interface science, **2016**. 233: p. 255-270.
5. Sokolov, K.,Follen, M.,Aaron, J.,Pavlova, I.,Malpica, A.,Lotan, R., Richards-Kortum, R., *Real-time vital optical imaging of precancer using anti-epidermal growth factor receptor antibodies conjugated to gold nanoparticles.* Cancer research, **2003**. 63(9): p. 1999-2004.
6. El-Sayed, I.H.,Huang, X., El-Sayed, M.A., *Surface plasmon resonance scattering and absorption of anti-EGFR antibody conjugated gold nanoparticles in cancer diagnostics: Applications in oral cancer.* Nano letters, **2005**. 5(5): p. 829-834.

7. Wang, S.,Lu, G., *Applications of gold nanoparticles in cancer imaging and treatment.* Noble and precious metals-properties, nanoscale effects and applications, **2018**. 1: p. 291-309.
8. Huang, H.-C.,Barua, S.,Sharma, G.,Dey, S.K., Rege, K., *Inorganic nanoparticles for cancer imaging and therapy.* Journal of controlled Release, **2011**. 155(3): p. 344-357.
9. Jin, R., *The impacts of nanotechnology on catalysis by precious metal nanoparticles.* Nanotechnology Reviews, **2012**. 1(1): p. 31-56.
10. Helmlinger, J.,Sengstock, C.,Groß-Heitfeld, C.,Mayer, C.,Schildhauer, T.,Köller, M., Epple, M., *Silver nanoparticles with different size and shape: Equal cytotoxicity, but different antibacterial effects.* RSC advances, **2016**. 6(22): p. 18490-18501.
11. Kittler, S.,Greulich, C.,Diendorf, J.,Koller, M., Epple, M., *Toxicity of silver nanoparticles increases during storage because of slow dissolution under release of silver ions.* Chemistry of materials, **2010**. 22(16): p. 4548-4554.
12. Köller, M.,Bellova, P.,Javid, S.M.,Motemani, Y.,Khare, C.,Sengstock, C.,Tschulik, K.,Schildhauer, T.A., Ludwig, A., *Antibacterial activity of microstructured sacrificial anode thin films by combination of silver with platinum group elements (platinum, palladium, iridium).* Materials Science and Engineering: C, **2017**. 74: p. 536-541.
13. Jaiswal, R.L.,Pandey, B.K., *Modeling for the study of thermophysical properties of metallic nanoparticles.* SN Applied Sciences, **2021**. 3(4): p. 466.
14. Kibria, M.,Anisur, M.,Mahfuz, M.,Saidur, R., Metselaar, I., *A review on thermophysical properties of nanoparticle dispersed phase change materials.* Energy conversion and management, **2015**. 95: p. 69-89.
15. Qi, W.,Wang, M., *Size and shape dependent lattice parameters of metallic nanoparticles.* Journal of Nanoparticle Research, **2005**. 7: p. 51-57.
16. Guenther, G.,Guillon, O., *Models of size-dependent nanoparticle melting tested on gold.* Journal of Materials Science, **2014**. 49(23): p. 7915-7932.
17. Qu, Y.D.,Liang, X.L.,Kong, X.Q., Zhang, W.J., *Size-dependent cohesive energy, melting temperature, and debye temperature of spherical metallic nanoparticles.* Physics of Metals and Metallography, **2017**. 118(6): p. 528-534.

18. Yu, X.,Zhan, Z., *The effects of the size of nanocrystalline materials on their thermodynamic and mechanical properties.* Nanoscale Research Letters, **2014**. 9: p. 1-6.
19. Salati, A.,Ramazani, A., Almasi Kashi, M., *Deciphering magnetic hyperthermia properties of compositionally and morphologically modulated feni nanoparticles using first-order reversal curve analysis.* Nanotechnology, **2019**. 30(2): p. 025707.
20. Noh, S.-H.,Moon, S.H.,Shin, T.-H.,Lim, Y., Cheon, J., *Recent advances of magneto-thermal capabilities of nanoparticles: From design principles to biomedical applications.* Nano Today, **2017**. 13: p. 61-76.
21. Koroleva, E.A.,Shabalkin, I.D., Krivoshapkin, P.V., *Monometallic and alloy nanoparticles: A review of biomedical applications.* Journal of Materials Chemistry B, **2023**.
22. Dheyab, M.A.,Aziz, A.A.,Khaniabadi, P.M.,Jameel, M.S.,Oladzadabbasabadi, N.,Rahman, A.A.,Braim, F.S., Mehrdel, B., *Gold nanoparticles-based photothermal therapy for breast cancer.* Photodiagnosis and photodynamic therapy, **2023**: p. 103312.
23. Yun, W.S.,Park, J.-H.,Lim, D.-K.,Ahn, C.-H.,Sun, I.-C., Kim, K., *How did conventional nanoparticle-mediated photothermal therapy become "HOT" in combination with cancer immunotherapy?* Cancers, **2022**. 14(8): p. 2044.
24. Cole-Hamilton, D.J., *Homogeneous catalysis--new approaches to catalyst separation, recovery, and recycling.* Science, **2003**. 299(5613): p. 1702-1706.
25. Rodrigues, T.S.,Da Silva, A.G.M., Camargo, P.H.C., *Nanocatalysis by noble metal nanoparticles: Controlled synthesis for the optimization and understanding of activities.* Journal of Materials Chemistry A, **2019**. 7(11): p. 5857-5874.
26. Dang-Bao, T.,Pla, D.,Favier, I., Gómez, M., *Bimetallic nanoparticles in alternative solvents for catalytic purposes.* Catalysts, **2017**. 7(7): p. 207.
27. Gao, C.,Lyu, F., Yin, Y., *Encapsulated metal nanoparticles for catalysis.* Chemical Reviews, **2021**. 121(2): p. 834-881.
28. Haruta, M., *Size- and support-dependency in the catalysis of gold.* Catalysis Today, **1997**. 36(1): p. 153-166.

29. Priecel, P.,Salami, H.A.,Padilla, R.H.,Zhong, Z., Lopez-Sanchez, J.A., *Anisotropic gold nanoparticles: Preparation and applications in catalysis.* chinese Journal of catalysis, **2016**. 37(10): p. 1619-1650.
30. Vourros, A.,Garagounis, I.,Kyriakou, V.,Carabineiro, S.,Maldonado-Hódar, F.,Marnellos, G., Konsolakis, M., *Carbon dioxide hydrogenation over supported Au nanoparticles: Effect of the support.* Journal of CO_2 utilization, **2017**. 19: p. 247-256.
31. Wilkinson, K.E.,Palmberg, L.,Witasp, E.,Kupczyk, M.,Feliu, N.,Gerde, P.,Seisenbaeva, G.A.,Fadeel, B.,Dahlen, S.-E., Kessler, V.G., *Solution-engineered palladium nanoparticles: Model for health effect studies of automotive particulate pollution.* ACS nano, **2011**. 5(7): p. 5312-5324.
32. Pérez-Lorenzo, M., *Palladium nanoparticles as efficient catalysts for Suzuki cross-coupling reactions.* The Journal of Physical Chemistry Letters, **2012**. 3(2): p. 167-174.
33. Zhang, Z.,Wang, Z., *Diatomite-supported pd nanoparticles: An efficient catalyst for Heck and Suzuki reactions.* The Journal of organic chemistry, **2006**. 71(19): p. 7485-7487.
34. Pacardo, D.B.,Sethi, M.,Jones, S.E.,Naik, R.R., Knecht, M.R., *Biomimetic synthesis of Pd nanocatalysts for the Stille coupling reaction.* ACS nano, **2009**. 3(5): p. 1288-1296.
35. Choi, K.W.,Ye, S.J., Park, O.O., *Shape-and size-controlled synthesis of noble metal nanoparticles.* Advances in Materials Research, **2014**. 3(4): p. 199.
36. Li, Y.,Boone, E., El-Sayed, M.A., *Size effects of PVP−Pd nanoparticles on the catalytic Suzuki reactions in aqueous solution.* Langmuir, **2002**. 18(12): p. 4921-4925.
37. An, K.,Somorjai, G.A., *Size and shape control of metal nanoparticles for reaction selectivity in catalysis.* ChemCatChem, **2012**. 4(10): p. 1512-1524.
38. Xie, S.,Choi, S.-I.,Xia, X., Xia, Y., *Catalysis on faceted noble-metal nanocrystals: Both shape and size matter.* Current Opinion in Chemical Engineering, **2013**. 2(2): p. 142-150.
39. Xu, R.,Wang, D.,Zhang, J., Li, Y., *Shape-dependent catalytic activity of silver nanoparticles for the oxidation of styrene.* Chemistry–An Asian Journal, **2006**. 1(6): p. 888-893.

40. Bratlie, K.M.,Lee, H.,Komvopoulos, K.,Yang, P., Somorjai, G.A., *Platinum nanoparticle shape effects on benzene hydrogenation selectivity.* Nano letters, **2007**. 7(10): p. 3097-3101.
41. Zhou, K.,Li, Y., *Catalysis based on nanocrystals with well-defined facets.* Angewandte Chemie International Edition, **2012**. 51(3): p. 602-613.
42. Xiao, C.,Lu, B.-A.,Xue, P.,Tian, N.,Zhou, Z.-Y.,Lin, X.,Lin, W.-F., Sun, S.-G., *High-index-facet- and high-surface-energy nanocrystals of metals and metal oxides as highly efficient catalysts.* Joule, **2020**. 4(12): p. 2562-2598.
43. Nguyen, V.-L.,Ohtaki, M.,Ngo, V.N.,Cao, M.-T., Nogami, M., *Structure and morphology of platinum nanoparticles with critical new issues of low-and high-index facets.* Advances in Natural Sciences: Nanoscience and Nanotechnology, **2012**. 3(2): p. 025005.
44. Liao, H.G.,Jiang, Y.X.,Zhou, Z.Y.,Chen, S.P., Sun, S.G., *Shape-controlled synthesis of gold nanoparticles in deep eutectic solvents for studies of structure–functionality relationships in electrocatalysis.* Angewandte Chemie International Edition, **2008**. 47(47): p. 9100-9103.
45. Zhang, P.,Wyman, I.,Hu, J.,Lin, S.,Zhong, Z.,Tu, Y.,Huang, Z., Wei, Y., *Silver nanowires: Synthesis technologies, growth mechanism and multifunctional applications.* Materials Science and Engineering: B, **2017**. 223: p. 1-23.
46. Mohanty, A.,Garg, N., Jin, R., *A universal approach to the synthesis of noble metal nanodendrites and their catalytic properties.* Angewandte Chemie, **2010**. 122(29): p. 5082-5086.
47. Auffan, M.,Rose, J.,Wiesner, M.R., Bottero, J.-Y., *Chemical stability of metallic nanoparticles: A parameter controlling their potential cellular toxicity in vitro.* Environmental Pollution, **2009**. 157(4): p. 1127-1133.
48. Toshima, N., *Metal nanoparticles for energy conversion.* Pure and Applied Chemistry, **2013**. 85(2): p. 437-451.
49. Gan, L.,Heggen, M.,O'malley, R.,Theobald, B., Strasser, P., *Understanding and controlling nanoporosity formation for improving the stability of bimetallic fuel cell catalysts.* Nano letters, **2013**. 13(3): p. 1131-1138.
50. Gawande, M.B.,Goswami, A.,Asefa, T.,Guo, H.,Biradar, A.V.,Peng, D.-L.,Zboril, R., Varma, R.S., *Core–shell nanoparticles: Synthesis and applications in catalysis and electrocatalysis.* Chemical Society Reviews, **2015**. 44(21): p. 7540-7590.

51. Mcnamara, K.,Tofail, S.A., *Nanosystems: The use of nanoalloys, metallic, bimetallic, and magnetic nanoparticles in biomedical applications.* Physical chemistry chemical physics, **2015**. 17(42): p. 27981-27995.
52. Loza, K.,Heggen, M., Epple, M., *Synthesis, structure, properties, and applications of bimetallic nanoparticles of noble metals.* Advanced Functional Materials, **2020**. 30(21): p. 1909260.
53. Peng, Z.,Yang, H., *Synthesis and oxygen reduction electrocatalytic property of Pt-on-Pd bimetallic heteronanostructures.* Journal of the American Chemical Society, **2009**. 131(22): p. 7542-7543.
54. Ye, H.,Crooks, R.M., *Effect of elemental composition of PtPd bimetallic nanoparticles containing an average of 180 atoms on the kinetics of the electrochemical oxygen reduction reaction.* Journal of the American Chemical Society, **2007**. 129(12): p. 3627-3633.
55. Alan, D.M.,Andrew, W., *Compendium of chemical terminology : IUPAC recommendations*. 1997: Second edition. Oxford [Oxfordshire] ; Malden, MA : Blackwell Science, 1997.
56. Cosgrove, T., *Colloid science: Principles, methods and applications*. 2010: John Wiley & Sons.
57. Mansfield, E.,Kaiser, D.L.,Fujita, D., Van De Voorde, M., *Metrology and standardization for nanotechnology: Protocols and industrial innovations*. 2017: John Wiley & Sons.
58. Bleeker, E.A.,De Jong, W.H.,Geertsma, R.E.,Groenewold, M.,Heugens, E.H.,Koers-Jacquemijns, M.,Van De Meent, D.,Popma, J.R.,Rietveld, A.G., Wijnhoven, S.W., *Considerations on the EU definition of a nanomaterial: Science to support policy making.* Regulatory toxicology and pharmacology, **2013**. 65(1): p. 119-125.
59. Barhoum, A.,García-Betancourt, M.L.,Jeevanandam, J.,Hussien, E.A.,Mekkawy, S.A.,Mostafa, M.,Omran, M.M.,S. Abdalla, M., Bechelany, M., *Review on natural, incidental, bioinspired, and engineered nanomaterials: History, definitions, classifications, synthesis, properties, market, toxicities, risks, and regulations.* Nanomaterials, **2022**. 12(2): p. 177.
60. Jeevanandam, J.,Barhoum, A.,Chan, Y.S.,Dufresne, A., Danquah, M.K., *Review on nanoparticles and nanostructured materials: History, sources,*

toxicity and regulations. Beilstein journal of nanotechnology, **2018**. 9(1): p. 1050-1074.

61. Lövestam, G.,Rauscher, H.,Roebben, G.,Klüttgen, B.S.,Gibson, N.,Putaud, J.-P., Stamm, H., *Considerations on a definition of nanomaterial for regulatory purposes.* Joint Research Centre (JRC) Reference Reports, **2010**. 80: p. 00-41.
62. Ding, J.,Miao, W.,Mccormick, P., Street, R., *Mechanochemical synthesis of ultrafine fe powder.* Applied Physics Letters, **1995**. 67(25): p. 3804-3806.
63. Barcikowski, S.,Hahn, A.,Kabashin, A., Chichkov, B., *Properties of nanoparticles generated during femtosecond laser machining in air and water.* Applied Physics A, **2007**. 87: p. 47-55.
64. Baig, N.,Kammakakam, I., Falath, W., *Nanomaterials: A review of synthesis methods, properties, recent progress, and challenges.* Materials Advances, **2021**. 2(6): p. 1821-1871.
65. Khan, I.,Saeed, K., Khan, I., *Nanoparticles: Properties, applications and toxicities.* Arabian journal of chemistry, **2019**. 12(7): p. 908-931.
66. Kolahalam, L.A.,Kasi Viswanath, I.V.,Diwakar, B.S.,Govindh, B.,Reddy, V., Murthy, Y.L.N., *Review on nanomaterials: Synthesis and applications.* Materials Today: Proceedings, **2019**. 18: p. 2182-2190.
67. Jamkhande, P.G.,Ghule, N.W.,Bamer, A.H., Kalaskar, M.G., *Metal nanoparticles synthesis: An overview on methods of preparation, advantages and disadvantages, and applications.* Journal of Drug Delivery Science and Technology, **2019**. 53: p. 101174.
68. Abid, N.,Khan, A.M.,Shujait, S.,Chaudhary, K.,Ikram, M.,Imran, M.,Haider, J.,Khan, M.,Khan, Q., Maqbool, M., *Synthesis of nanomaterials using various top-down and bottom-up approaches, influencing factors, advantages, and disadvantages: A review.* Advances in Colloid and Interface Science, **2022**. 300: p. 102597.
69. Xia, Y.,Xiong, Y.,Lim, B., Skrabalak, S.E., *Formkontrolle bei der synthese von metallnanokristallen: Einfache chemie, komplexe physik?* Angewandte Chemie, **2009**. 121(1): p. 62-108.
70. Mer, V.K.L., *Nucleation in phase transitions.* Industrial & Engineering Chemistry, **1952**. 44(6): p. 1270-1277.
71. Mourdikoudis, S., *Reducing agents in colloidal nanoparticle synthesis*. 2021: Royal Society of Chemistry.

72. Kim, H.-S.,Seo, Y.S.,Kim, K.,Han, J.W.,Park, Y., Cho, S., *Concentration effect of reducing agents on green synthesis of gold nanoparticles: Size, morphology, and growth mechanism.* Nanoscale research letters, **2016**. 11: p. 1-9.
73. Ostwald, W., *Über die vermeintliche isomerie des roten und gelben quecksilberoxyds und die oberflächenspannung fester körper.* Zeitschrift für physikalische Chemie, **1900**. 34(1): p. 495-503.
74. Hughes, R.,Cosgrove, T., *An introduction to colloids.* Colloid Science: Principles, Methods and Applications, **2010**: p. 1-21.
75. Trefalt, G.,Borkovec, M., *Overview of DLVO theory.* Laboratory of Colloid and Surface Chemistry, University of Geneva, Switzerland, **2014**. 304.
76. Derjaguin, B.,Churaev, N.,Muller, V.,Derjaguin, B.,Churaev, N., Muller, V., *The Derjaguin—Landau—Verwey—Overbeek (DLVO) theory of stability of lyophobic colloids.* Surface forces, **1987**: p. 293-310.
77. Dörfler, H.-D., *Grenzflächen und kolloid-disperse systeme: Physik und chemie*. 2002: Springer.
78. Schmid, G., *Nanoparticles: From theory to application*. 2011: John Wiley & Sons.
79. Narayanan, R.,El-Sayed, M.A., *Catalysis with transition metal nanoparticles in colloidal solution: Nanoparticle shape dependence and stability.* The Journal of Physical Chemistry B, **2005**. 109(26): p. 12663-12676.
80. Trovarelli, A.,Llorca, J., *Ceria catalysts at nanoscale: How do crystal shapes shape catalysis?* ACS Catalysis, **2017**. 7(7): p. 4716-4735.
81. Xie, X.,Liao, J.,Shao, X.,Li, Q., Lin, Y., *The effect of shape on cellular uptake of gold nanoparticles in the forms of stars, rods, and triangles.* Scientific reports, **2017**. 7(1): p. 3827.
82. Wiley, B.,Sun, Y., Xia, Y., *Synthesis of silver nanostructures with controlled shapes and properties.* Accounts of chemical research, **2007**. 40(10): p. 1067-1076.
83. Xia, Y.,Xiong, Y.,Lim, B., Skrabalak, S.E., *Shape-controlled synthesis of metal nanocrystals: Simple chemistry meets complex physics?* Angewandte Chemie International Edition, **2009**. 48(1): p. 60-103.
84. Chen, J.,Lim, B.,Lee, E.P., Xia, Y., *Shape-controlled synthesis of platinum nanocrystals for catalytic and electrocatalytic applications.* Nano Today, **2009**. 4(1): p. 81-95.

85. Wang, C.,Huang, Z.,Ding, Y.,Xie, M.,Chi, M., Xia, Y., *Facet-controlled synthesis of platinum-group-metal quaternary alloys: The case of nanocubes and {100} facets.* Journal of the American Chemical Society, **2023**. 145(4): p. 2553-2560.
86. Nguyen, Q.N.,Wang, C.,Shang, Y.,Janssen, A., Xia, Y., *Colloidal synthesis of metal nanocrystals: From asymmetrical growth to symmetry breaking.* Chemical Reviews, **2023**. 123(7): p. 3693-3760.
87. Carroll, K.J.,Reveles, J.U.,Shultz, M.D.,Khanna, S.N., Carpenter, E.E., *Preparation of elemental Cu and Ni nanoparticles by the polyol method: An experimental and theoretical approach.* The Journal of Physical Chemistry C, **2011**. 115(6): p. 2656-2664.
88. Fiévet, F.,Ammar-Merah, S.,Brayner, R.,Chau, F.,Giraud, M.,Mammeri, F.,Peron, J.,Piquemal, J.Y.,Sicard, L., Viau, G., *The polyol process: A unique method for easy access to metal nanoparticles with tailored sizes, shapes and compositions.* Chemical Society Reviews, **2018**. 47(14): p. 5187-5233.
89. Bao, H.,Zhang, Z.,Hua, Q., Huang, W., *Compositions, structures, and catalytic activities of CeO2@Cu_2O nanocomposites prepared by the template-assisted method.* Langmuir, **2014**. 30(22): p. 6427-6436.
90. Chen, S.,Carroll, D.L., *Synthesis and characterization of truncated triangular silver nanoplates.* Nano letters, **2002**. 2(9): p. 1003-1007.
91. Rao, B.,Mukherjee, D., Reddy, B., *Chapter 1: Novel approaches for preparation of nanoparticles, nanostructures for novel therapy, synthesis, characterization and applications, micro and nano technologies*. 2017, Elsevier, Amsterdam.
92. Song, T.,Gao, F.,Guo, S.,Zhang, Y.,Li, S.,You, H., Du, Y., *A review of the role and mechanism of surfactants in the morphology control of metal nanoparticles.* Nanoscale, **2021**. 13(7): p. 3895-3910.
93. Xia, Y.,Xia, X., Peng, H.-C., *Shape-controlled synthesis of colloidal metal nanocrystals: Thermodynamic versus kinetic products.* Journal of the American Chemical Society, **2015**. 137(25): p. 7947-7966.
94. Wang, Y.,He, J.,Liu, C.,Chong, W.H., Chen, H., *Thermodynamics versus kinetics in nanosynthesis.* Angewandte Chemie International Edition, **2015**. 54(7): p. 2022-2051.
95. Wang, Z., *Transmission electron microscopy of shape-controlled nanocrystals and their assemblies*. 2000, ACS Publications. p. 1153-1175.

96. Vitos, L.,Ruban, A.V.,Skriver, H.L., Kollár, J., *The surface energy of metals.* Surface Science, **1998**. 411(1): p. 186-202.
97. Al-Saidi, W.A.,Feng, H., Fichthorn, K.A., *Adsorption of polyvinylpyrrolidone on Ag surfaces: Insight into a structure-directing agent.* Nano Letters, **2012**. 12(2): p. 997-1001.
98. Wu, B.,Zheng, N., *Surface and interface control of noble metal nanocrystals for catalytic and electrocatalytic applications.* Nano Today, **2013**. 8(2): p. 168-197.
99. Chen, Q.,Richardson, N.V., *Surface facetting induced by adsorbates.* Progress in Surface Science, **2003**. 73(4): p. 59-77.
100. Chiu, C.-Y.,Wu, H.,Yao, Z.,Zhou, F.,Zhang, H.,Ozolins, V., Huang, Y., *Facet-selective adsorption on noble metal crystals guided by electrostatic potential surfaces of aromatic molecules.* Journal of the American Chemical Society, **2013**. 135(41): p. 15489-15500.
101. Yang, T.H.,Shi, Y.,Janssen, A., Xia, Y., *Surface capping agents and their roles in shape-controlled synthesis of colloidal metal nanocrystals.* Angewandte Chemie International Edition, **2020**. 59(36): p. 15378-15401.
102. Ristig, S.,Prymak, O.,Loza, K.,Gocyla, M.,Meyer-Zaika, W.,Heggen, M.,Raabe, D., Epple, M., *Nanostructure of wet-chemically prepared, polymer-stabilized silver–gold nanoalloys (6 nm) over the entire composition range.* Journal of Materials Chemistry B, **2015**. 3(23): p. 4654-4662.
103. Zaleska-Medynska, A.,Marchelek, M.,Diak, M., Grabowska, E., *Noble metal-based bimetallic nanoparticles: The effect of the structure on the optical, catalytic and photocatalytic properties.* Advances in colloid and interface science, **2016**. 229: p. 80-107.
104. Safaie, N.,Ferrier, R.C., *Janus nanoparticle synthesis: Overview, recent developments, and applications.* Journal of Applied Physics, **2020**. 127(17).
105. Ghosh, S.K.,Pal, T., *Interparticle coupling effect on the surface plasmon resonance of gold nanoparticles: From theory to applications.* Chemical reviews, **2007**. 107(11): p. 4797-4862.
106. Hou, P.,Liu, H.,Li, J., Yang, J., *One-pot synthesis of noble metal nanoparticles with a core–shell construction.* CrystEngComm, **2015**. 17(8): p. 1826-1832.
107. Kumar-Krishnan, S.,Estevez-González, M.,Pérez, R.,Esparza, R., Meyyappan, M., *A general seed-mediated approach to the synthesis of AgM (M= Au, Pt, and*

Pd) core–shell nanoplates and their sers properties. RSC advances, **2017**. 7(44): p. 27170-27176.

108. Skrabalak, S.E.,Au, L.,Lu, X.,Li, X., Xia, Y., *Gold nanocages for cancer detection and treatment.* **2007**.
109. Oh, M.H.,Yu, T.,Yu, S.-H.,Lim, B.,Ko, K.-T.,Willinger, M.-G.,Seo, D.-H.,Kim, B.H.,Cho, M.G., Park, J.-H., *Galvanic replacement reactions in metal oxide nanocrystals.* Science, **2013**. 340(6135): p. 964-968.
110. Wang, Z.,Zhou, L., Lou, X.W., *Metal oxide hollow nanostructures for lithium-ion batteries*. 2012, Wiley Online Library.
111. Yang, Y.,Liu, J.,Fu, Z.-W., Qin, D., *Galvanic replacement-free deposition of Au on Ag for core–shell nanocubes with enhanced chemical stability and SERS activity.* Journal of the American Chemical Society, **2014**. 136(23): p. 8153-8156.
112. Cheng, H.,Wang, C.,Qin, D., Xia, Y., *Galvanic replacement synthesis of metal nanostructures: Bridging the gap between chemical and electrochemical approaches.* Accounts of Chemical Research, **2023**. 56(7): p. 900-909.
113. Da Silva, A.G.M.,Rodrigues, T.S.,Haigh, S.J., Camargo, P.H.C., *Galvanic replacement reaction: Recent developments for engineering metal nanostructures towards catalytic applications.* Chemical Communications, **2017**. 53(53): p. 7135-7148.
114. Yadav, V.,Jeong, S.,Ye, X., Li, C.W., *Surface-limited galvanic replacement reactions of Pd, Pt, and Au onto Ag core nanoparticles through redox potential tuning.* Chemistry of Materials, **2022**. 34(4): p. 1897-1904.
115. Mendis, P.,De Silva, R.M.,De Silva, K.M.N.,Wijenayaka, L.A.,Jayawardana, K., Yan, M., *Nanosilver rainbow: A rapid and facile method to tune different colours of nanosilver through the controlled synthesis of stable spherical silver nanoparticles.* RSC Advances, **2016**. 6(54): p. 48792-48799.
116. He, R.,Qian, X.,Yin, J., Zhu, Z., *Preparation of polychrome silver nanoparticles in different solvents.* Journal of Materials Chemistry, **2002**. 12(12): p. 3783-3786.
117. Jones, M.R.,Osberg, K.D.,Macfarlane, R.J.,Langille, M.R., Mirkin, C.A., *Templated techniques for the synthesis and assembly of plasmonic nanostructures.* Chemical reviews, **2011**. 111(6): p. 3736-3827.

118. Kelly, K.L.,Coronado, E.,Zhao, L.L., Schatz, G.C., *The optical properties of metal nanoparticles: The influence of size, shape, and dielectric environment*. 2003, ACS Publications. p. 668-677.
119. Gao, Y.,Song, L.,Jiang, P.,Liu, L.F.,Yan, X.Q.,Zhou, Z.P.,Liu, D.F.,Wang, J.X.,Yuan, H.J.,Zhang, Z.X.,Zhao, X.W.,Dou, X.Y.,Zhou, W.Y.,Wang, G.,Xie, S.S.,Chen, H.Y., Li, J.Q., *Silver nanowires with five-fold symmetric cross-section.* Journal of Crystal Growth, **2005**. 276(3): p. 606-612.
120. He, S.,Yao, J.,Jiang, P.,Shi, D.,Zhang, H.,Xie, S.,Pang, S., Gao, H., *Formation of silver nanoparticles and self-assembled two-dimensional ordered superlattice.* Langmuir, **2001**. 17(5): p. 1571-1575.
121. Skoog, D.A.,Holler, F.J., Crouch, S.R., *Principles of instrumental analysis*. 2017: Cengage learning.
122. Amendola, V.,Meneghetti, M., *Size evaluation of gold nanoparticles by UV-Vis spectroscopy.* The Journal of Physical Chemistry C, **2009**. 113(11): p. 4277-4285.
123. Reguera, J.,Langer, J.,De Aberasturi, D.J., Liz-Marzán, L.M., *Anisotropic metal nanoparticles for surface enhanced raman scattering.* Chemical Society Reviews, **2017**. 46(13): p. 3866-3885.
124. Greenway, G.M., *Atomic absorption spectrometry, Bernhard Welz and Michael Sperling, Wiley-VCH, Weinheim, 1999, 94l pp.,(0-352-728-5717), third edition,* **2000**.
125. Mahl, D.,Diendorf, J.,Meyer-Zaika, W., Epple, M., *Possibilities and limitations of different analytical methods for the size determination of a bimodal dispersion of metallic nanoparticles.* Colloids and Surfaces A: Physicochemical and Engineering Aspects, **2011**. 377(1-3): p. 386-392.
126. Schärtl, W., *Light scattering from polymer solutions and nanoparticle dispersions*. 2007: Springer Science & Business Media.
127. Kato, H., *Size determination of nanoparticles by dynamic light scattering*, in *Nanomaterials*. 2012. p. 535-554.
128. Kumar, A.,Dixit, C.K., *3 - methods for characterization of nanoparticles*, in *Advances in nanomedicine for the delivery of therapeutic nucleic acids*, Nimesh, S., Chandra, R., and Gupta, N., Editors. 2017, Woodhead Publishing. p. 43-58.

129. Akbari, B.,Tavandashti, M.P., Zandrahimi, M., *Particle size characterization of nanoparticles - A practical approach.* Iranian Journal of Materials Science and Engineering, **2011**. 8(2): p. 48-56.
130. Gambinossi, F.,Mylon, S.E., Ferri, J.K., *Aggregation kinetics and colloidal stability of functionalized nanoparticles.* Advances in Colloid and Interface Science, **2015**. 222: p. 332-349.
131. Laidlaw, I.,Steinmetz, M., *Introduction to differential sedimentation.* Analytical ultracentrifugation. The Royal Society of Chemistry, Cambridge, **2005**: p. 270-290.
132. Banerjee, S.,Loza, K.,Meyer-Zaika, W.,Prymak, O., Epple, M., *Structural evolution of silver nanoparticles during wet-chemical synthesis.* Chemistry of Materials, **2014**. 26(2): p. 951-957.
133. Amelinckx, S.,Van Dyck, D.,Van Landuyt, J., Van Tendeloo, G., *Electron microscopy: Principles and fundamentals*. 2008: John Wiley & Sons.
134. Akhtar, K.,Khan, S.A.,Khan, S.B., Asiri, A.M., *Scanning electron microscopy: Principle and applications in nanomaterials characterization*, in *Handbook of materials characterization*, Sharma, S.K., Editor. 2018, Springer International Publishing: Cham. p. 113-145.
135. Goodhew, P., *General introduction to transmission electron microscopy (tem).* Aberration-Corrected Analytical Transmission Electron Microscopy, **2011**: p. 1-19.
136. Heggen, M.,Luysberg, M., Tillmann, K., *FEI Titan 80-300 STEM.* Journal of large-scale research facilities JLSRF, **2016**. 2: p. A42-A42.
137. Goldstein, J.I.,Newbury, D.E.,Michael, J.R.,Ritchie, N.W.,Scott, J.H.J., Joy, D.C., *Scanning electron microscopy and X-ray microanalysis*. 2017: Springer.
138. Whittig, L.,Allardice, W., *X-ray diffraction techniques.* Methods of Soil Analysis: Part 1 Physical and Mineralogical Methods, **1986**. 5: p. 331-362.
139. Prime, R.B.,Bair, H.E.,Vyazovkin, S.,Gallagher, P.K., Riga, A., *Thermogravimetric analysis (tga).* Thermal analysis of polymers: Fundamentals and applications, **2009**: p. 241-317.
140. Saadatkhah, N.,Carillo Garcia, A.,Ackermann, S.,Leclerc, P.,Latifi, M.,Samih, S.,Patience, G.S., Chaouki, J., *Experimental methods in chemical engineering: Thermogravimetric analysis—tga.* The Canadian Journal of Chemical Engineering, **2020**. 98(1): p. 34-43.

141. Coats, A.,Redfern, J., *Thermogravimetric analysis. A review.* Analyst, **1963**. 88(1053): p. 906-924.
142. Ahlberg, S.,Antonopulos, A.,Diendorf, J.,Dringen, R.,Epple, M.,Flöck, R.,Goedecke, W.,Graf, C.,Haberl, N., Helmlinger, J., *PVP-coated, negatively charged silver nanoparticles: A multi-center study of their physicochemical characteristics, cell culture and in vivo experiments.* Beilstein journal of nanotechnology, **2014**. 5(1): p. 1944-1965.
143. Wang, H.,Qiao, X.,Chen, J., Ding, S., *Preparation of silver nanoparticles by chemical reduction method.* Colloids and Surfaces A: Physicochemical and Engineering Aspects, **2005**. 256(2): p. 111-115.
144. Loza, K.,Epple, M., *Silver nanoparticles in complex media: An easy procedure to discriminate between metallic silver nanoparticles, reprecipitated silver chloride, and dissolved silver species.* RSC advances, **2018**. 8(43): p. 24386-24391.
145. Jin, M.,Liu, H.,Zhang, H.,Xie, Z.,Liu, J., Xia, Y., *Synthesis of Pd nanocrystals enclosed by {100} facets and with sizes< 10 nm for application in CO oxidation.* Nano Research, **2011**. 4: p. 83-91.
146. Hachani, R.,Lowdell, M.,Birchall, M.,Hervault, A.,Mertz, D.,Begin-Colin, S., Thanh, N.T.K., *Polyol synthesis, functionalisation, and biocompatibility studies of superparamagnetic iron oxide nanoparticles as potential MRI contrast agents.* Nanoscale, **2016**. 8(6): p. 3278-3287.
147. Dong, H.,Chen, Y.-C., Feldmann, C., *Polyol synthesis of nanoparticles: Status and options regarding metals, oxides, chalcogenides, and non-metal elements.* Green chemistry, **2015**. 17(8): p. 4107-4132.
148. Ammar, S.,Fiévet, F., *Polyol synthesis: A versatile wet-chemistry route for the design and production of functional inorganic nanoparticles*. 2020, MDPI. p. 1217.
149. Im, S.H.,Lee, Y.T.,Wiley, B., Xia, Y., *Large-scale synthesis of silver nanocubes: The role of HCL in promoting cube perfection and monodispersity.* Angewandte Chemie International Edition, **2005**. 44(14): p. 2154-2157.
150. Schuette, W.M.,Buhro, W.E., *Silver chloride as a heterogeneous nucleant for the growth of silver nanowires.* Acs Nano, **2013**. 7(5): p. 3844-3853.
151. Helmlinger, J., *Silber-Nanopartikel mit definierter morphologie*. 2015.

152. Pappert, K., *Synthesis and in-depth characterization of mono- and bimetallic nanoparticles*. 2018.
153. Wojtysiak, S.,Solla-Gullón, J.,Dłużewski, P., Kudelski, A., *Synthesis of core-shell silver-platinum nanoparticles, improving shell integrity.* Colloids and Surfaces A: Physicochemical and Engineering Aspects, **2014**. 441: p. 178-183.
154. Mele, L.,Konings, S.,Dona, P.,Evertz, F.,Mitterbauer, C.,Faber, P.,Schampers, R., Jinschek, J.R., *A mems-based heating holder for the direct imaging of simultaneous in-situ heating and biasing experiments in scanning/transmission electron microscopes.* Microscopy Research and Technique, **2016**. 79(4): p. 239-250.
155. accessed on 29.06.2023, Available from: https://denssolutions.com/products/wildfire/.
156. Martínez-Castañon, G.-A.,Nino-Martinez, N.,Martinez-Gutierrez, F.,Martínez-Mendoza, J., Ruiz, F., *Synthesis and antibacterial activity of silver nanoparticles with different sizes.* Journal of nanoparticle research, **2008**. 10: p. 1343-1348.
157. Lee, K.-S.,El-Sayed, M.A., *Gold and silver nanoparticles in sensing and imaging: Sensitivity of plasmon response to size, shape, and metal composition.* The Journal of Physical Chemistry B, **2006**. 110(39): p. 19220-19225.
158. Paramelle, D.,Sadovoy, A.,Gorelik, S.,Free, P.,Hobley, J., Fernig, D.G., *A rapid method to estimate the concentration of citrate capped silver nanoparticles from uv-visible light spectra.* Analyst, **2014**. 139(19): p. 4855-4861.
159. Helmlinger, J.,Prymak, O.,Loza, K.,Gocyla, M.,Heggen, M., Epple, M., *On the crystallography of silver nanoparticles with different shapes.* Crystal Growth & Design, **2016**. 16(7): p. 3677-3687.
160. Helmlinger, J.,Heise, M.,Heggen, M.,Ruck, M., Epple, M., *A rapid, high-yield and large-scale synthesis of uniform spherical silver nanoparticles by a microwave-assisted polyol process.* RSC advances, **2015**. 5(112): p. 92144-92150.
161. Sergeev, M.O.,Revina, A.A.,Busev, S.A.,Zolotarevskiy, V.I.,Zhavoronkova, K.N., Boeva, O.A., *Catalytic properties of monometallic and bimetallic palladium and rhodium nanoparticles obtained in reverse micellar systems.* Nanotechnology Reviews, **2014**. 3(5): p. 515-525.
162. Nasrollahzadeh, M.,Sajadi, S.M.,Honarmand, E., Maham, M., *Preparation of palladium nanoparticles using euphorbia thymifolia l. Leaf extract and*

evaluation of catalytic activity in the ligand-free stille and hiyama cross-coupling reactions in water. New Journal of Chemistry, **2015**. 39(6): p. 4745-4752.

163. Xiong, Y.,Chen, J.,Wiley, B.,Xia, Y.,Yin, Y., Li, Z.-Y., *Size-dependence of surface plasmon resonance and oxidation for Pd nanocubes synthesized via a seed etching process.* Nano letters, **2005**. 5(7): p. 1237-1242.
164. Carrasquillo Jr, A.,Jeng, J.-J.,Barriga, R.J.,Temesghen, W.F., Soriaga, M.P., *Electrode-surface coordination chemistry: Ligand substitution and competitive coordination of halides at well-defined Pd (100) and Pd (111) single crystals.* Inorganica chimica acta, **1997**. 255(2): p. 249-254.
165. Schimpf, J.A.,Abreu, J.B., Soriaga, M.P., *Electrochemical regeneration of clean and ordered Pd(100) surfaces by iodine adsorption-desorption: Evidence from low-energy electron diffraction.* Journal of Electroanalytical Chemistry, **1994**. 364(1): p. 247-249.
166. Xiong, Y.,Cai, H.,Wiley, B.J.,Wang, J.,Kim, M.J., Xia, Y., *Synthesis and mechanistic study of palladium nanobars and nanorods.* Journal of the American Chemical Society, **2007**. 129(12): p. 3665-3675.
167. Niu, W.,Li, Z.-Y.,Shi, L.,Liu, X.,Li, H.,Han, S.,Chen, J., Xu, G., *Seed-mediated growth of nearly monodisperse palladium nanocubes with controllable sizes.* Crystal Growth and Design, **2008**. 8(12): p. 4440-4444.
168. Dutta, B.,Dayal, B., *Lattice constants and thermal expansion of palladium and tungsten up to 878 °C by X-ray method.* physica status solidi (b), **1963**. 3(12): p. 2253-2259.
169. Wu, Z.,Xiao, D.,Lee, J.,Ren, P.,Song, M., Li, D., *Palladium nanostructures with well-controlled morphologies obtained by one-pot and one-step polyol method.* Journal of Crystal Growth, **2019**. 521: p. 34-40.
170. Pimpinelli, A.,Villain, J., *Physics of crystal growth*. 1999.
171. Amirjani, A.,Firouzi, F., Haghshenas, D.F., *Predicting the size of silver nanoparticles from their optical properties.* Plasmonics, **2020**. 15: p. 1077-1082.
172. Yu, Y.,Zhao, Y.,Huang, T., Liu, H., *Microwave-assisted synthesis of palladium nanocubes and nanobars.* Materials Research Bulletin, **2010**. 45(2): p. 159-164.
173. Wiley, B.,Sun, Y.,Chen, J.,Cang, H.,Li, Z.-Y.,Li, X., Xia, Y., *Shape-controlled synthesis of silver and gold nanostructures.* Mrs Bulletin, **2005**. 30(5): p. 356-361.

174. Wiley, B.,Herricks, T.,Sun, Y., Xia, Y., *Polyol synthesis of silver nanoparticles: Use of chloride and oxygen to promote the formation of single-crystal, truncated cubes and tetrahedrons.* Nano Letters, **2004**. 4(9): p. 1733-1739.
175. Schuette, W.M.,Buhro, W.E., *Polyol synthesis of silver nanowires by heterogeneous nucleation; mechanistic aspects influencing nanowire diameter and length.* Chemistry of Materials, **2014**. 26(22): p. 6410-6417.
176. Sun, Y.,Ren, Y.,Liu, Y.,Wen, J.,Okasinski, J.S., Miller, D.J., *Ambient-stable tetragonal phase in silver nanostructures.* Nature Communications, **2012**. 3(1): p. 971.
177. Liu, B.,Yan, H.,Chen, S.,Guan, Y.,Wu, G.,Jin, R., Li, L., *Stable and controllable synthesis of silver nanowires for transparent conducting film.* Nanoscale Research Letters, **2017**. 12(1): p. 212.
178. Mao, H.,Feng, J.,Ma, X.,Wu, C., Zhao, X., *One-dimensional silver nanowires synthesized by self-seeding polyol process.* Journal of Nanoparticle Research, **2012**. 14(6): p. 887.
179. Skrabalak, S.E.,Au, L.,Li, X., Xia, Y., *Facile synthesis of Ag nanocubes and Au nanocages.* Nature Protocols, **2007**. 2(9): p. 2182-2190.
180. Sun, Y.,Xia, Y., *Shape-controlled synthesis of gold and silver nanoparticles.* Science, **2002**. 298(5601): p. 2176-2179.
181. Pawlik, V.,Zhou, S.,Zhou, S.,Qin, D., Xia, Y., *Silver nanocubes: From serendipity to mechanistic understanding, rational synthesis, and Niche applications.* Chemistry of Materials, **2023**. 35(9): p. 3427-3449.
182. Chang, S.,Chen, K.,Hua, Q.,Ma, Y., Huang, W., *Evidence for the growth mechanisms of silver nanocubes and nanowires.* The Journal of Physical Chemistry C, **2011**. 115(16): p. 7979-7986.
183. Tang, X.,Tsuji, M.,Jiang, P.,Nishio, M.,Jang, S.-M., Yoon, S.-H., *Rapid and high-yield synthesis of silver nanowires using air-assisted polyol method with chloride ions.* Colloids and Surfaces A: Physicochemical and Engineering Aspects, **2009**. 338(1-3): p. 33-39.
184. Rycenga, M.,Xia, X.,Moran, C.H.,Zhou, F.,Qin, D.,Li, Z.-Y., Xia, Y., *Generation of hot spots with silver nanocubes for single-molecule detection by surface-enhanced Raman scattering.* Angewandte Chemie (International ed. in English), **2011**. 50(24): p. 5473.

185. Wang, H.,Li, K.,Xu, C.,Xu, S., Li, G., *Large-scale solvothermal synthesis of Ag nanocubes with high sers activity.* Journal of Alloys and Compounds, **2019**. 772: p. 150-156.
186. Liu, L.,Wu, Y.,Yin, N.,Zhang, H., Ma, H., *Silver nanocubes with high SERS performance.* Journal of Quantitative Spectroscopy and Radiative Transfer, **2020**. 240: p. 106682.
187. Gheitaran, R.,Afkhami, A., Madrakian, T., *Effect of light at different wavelengths on polyol synthesis of silver nanocubes.* Scientific Reports, **2022**. 12(1): p. 19202.
188. Sosa, I.O.,Noguez, C., Barrera, R.G., *Optical properties of metal nanoparticles with arbitrary shapes.* The Journal of Physical Chemistry B, **2003**. 107(26): p. 6269-6275.
189. Zhou, F.,Li, Z.-Y.,Liu, Y., Xia, Y., *Quantitative analysis of dipole and quadrupole excitation in the surface plasmon resonance of metal nanoparticles.* The Journal of Physical Chemistry C, **2008**. 112(51): p. 20233-20240.
190. Kan, C.-X.,Zhu, J.-J., Zhu, X.-G., *Silver nanostructures with well-controlled shapes: Synthesis, characterization and growth mechanisms.* Journal of Physics D: Applied Physics, **2008**. 41(15): p. 155304.
191. Sun, X.,Qin, D., *Co-titration of agno 3 and haucl 4: A new route to the synthesis of Ag@ Ag–Au core–frame nanocubes with enhanced plasmonic and catalytic properties.* Journal of Materials Chemistry C, **2015**. 3(45): p. 11833-11841.
192. Martínez, J.,Chequer, N.,González, J., Cordova, T., *Alternative methodology for gold nanoparticles diameter characterization using PCA technique and UV-Vis spectrophotometry.* Nanosci. Nanotechnol, **2012**. 2(6): p. 184-189.
193. Wang, G.,Liu, Y.,Gao, C.,Guo, L.,Chi, M.,Ijiro, K.,Maeda, M., Yin, Y., *Island growth in the seed-mediated overgrowth of monometallic colloidal nanostructures.* Chem, **2017**. 3(4): p. 678-690.
194. Lorenz, W.,Staikov, G., *2D and 3D thin film formation and growth mechanisms in metal electrocrystallization—an atomistic view by in situ STM.* Surface science, **1995**. 335: p. 32-43.
195. Baskaran, A.,Smereka, P., *Mechanisms of Stranski-Krastanov growth.* Journal of Applied Physics, **2012**. 111(4): p. 044321.
196. Tomizuka, C.,Sonder, E., *Self-diffusion in silver.* Physical Review, **1956**. 103(5): p. 1182.

197. Prymak, O.,Jakobi, J.,Rehbock, C.,Epple, M., Barcikowski, S., *Crystallographic characterization of laser-generated, polymer-stabilized 4 nm silver-gold alloyed nanoparticles.* Materials Chemistry and Physics, **2018**. 207: p. 442-450.
198. Sławiński, G.W.,Zamborini, F.P., *Synthesis and alignment of silver nanorods and nanowires and the formation of Pt, Pd, and core/shell structures by galvanic exchange directly on surfaces.* Langmuir, **2007**. 23(20): p. 10357-10365.
199. Zhang, L.,Roling, L.T.,Wang, X.,Vara, M.,Chi, M.,Liu, J.,Choi, S.-I.,Park, J.,Herron, J.A., Xie, Z., *Platinum-based nanocages with subnanometer-thick walls and well-defined, controllable facets.* Science, **2015**. 349(6246): p. 412-416.
200. Xie, S.,Choi, S.-I.,Lu, N.,Roling, L.T.,Herron, J.A.,Zhang, L.,Park, J.,Wang, J.,Kim, M.J., Xie, Z., *Atomic layer-by-layer deposition of Pt on Pd nanocubes for catalysts with enhanced activity and durability toward oxygen reduction.* Nano letters, **2014**. 14(6): p. 3570-3576.
201. Arblaster, J., *Crystallographic properties of platinum.* Platinum Metals Review, **1997**. 41(1): p. 12-21.
202. Asoro, M.A.,Kovar, D., Ferreira, P.J., *In situ transmission electron microscopy observations of sublimation in silver nanoparticles.* ACS nano, **2013**. 7(9): p. 7844-7852.
203. Sambles, J.R., *An electron microscope study of evaporating gold particles: The Kelvin equation for liquid gold and the lowering of the melting point of solid gold particles.* Proceedings of the Royal Society of London. A. Mathematical and Physical Sciences, **1971**. 324(1558): p. 339-351.
204. Sambles, J.R.,Skinner, L., Lisgarten, N., *An electron microscope study of evaporating small particles: The Kelvin equation for liquid lead and the mean surface energy of solid silver.* Proceedings of the Royal Society of London. A. Mathematical and Physical Sciences, **1970**. 318(1535): p. 507-522.
205. Li, J.,Wang, Z.,Li, Y., Deepak, F.L., *In situ atomic-scale observation of kinetic pathways of sublimation in silver nanoparticles.* Advanced Science, **2019**. 6(8): p. 1802131.
206. Rahman, M.T.,Mccloy, J.,Ramana, C., Panat, R., *Structure, electrical characteristics, and high-temperature stability of aerosol jet printed silver nanoparticle films.* Journal of Applied Physics, **2016**. 120(7): p. 075305.

207. Prymak, O.,Grasmik, V.,Loza, K.,Heggen, M., Epple, M., *Temperature-induced stress relaxation in alloyed silver–gold nanoparticles (7–8 nm) by in situ X-ray powder diffraction.* Crystal growth & design, **2019**. 20(1): p. 107-115.
208. Schadel, H.,Birchenall, C., *The vapor pressure of silver.* JOM, **1950**. 2: p. 1134-1138.
209. Panish, M.B., *Vapor pressure of silver.* Journal of Chemical and Engineering Data, **1961**. 6(4): p. 592-594.
210. Hildenbrand, D.,Hall, W., *The vapor pressure and heat of sublimation of gold.* The Journal of Physical Chemistry, **1962**. 66(4): p. 754-755.
211. Sun, Y., *Controlled synthesis of colloidal silver nanoparticles in organic solutions: Empirical rules for nucleation engineering.* Chemical Society Reviews, **2013**. 42(7): p. 2497-2511.
212. Elechiguerra, J.L.,Reyes-Gasga, J., Yacaman, M.J., *The role of twinning in shape evolution of anisotropic noble metal nanostructures.* Journal of Materials Chemistry, **2006**. 16(40): p. 3906-3919.
213. Buffat, P., *Electron diffraction and HRTEM studies of multiply-twinned structures and dynamical events in metal nanoparticles: Facts and artefacts.* Materials chemistry and physics, **2003**. 81(2-3): p. 368-375.
214. Du, Y.,Yang, P.,Mou, Z.,Hua, N., Jiang, L., *Thermal decomposition behaviors of PVP coated on platinum nanoparticles.* Journal of Applied Polymer Science, **2006**. 99(1): p. 23-26.

9. Appendix

9.1 List of abbreviations

AAS	Atomic Absorption Spectroscopy
Ag@Au	Silver-gold core-shell
DCS	Differential Centrifugal Sedimentation
DEG	Diethylene Glycol
DLS	Dynamic Light Scattering
DLVO	Derjagin, Landau, Verwey and Overbeek theory
EDS	Energy dispersive X-ray Spectroscopy
EG	Ethylene Glycol
f.c.c.	face-centered cubic
mV	Millivolt
Pd@Pt	Palladium-platinum core-shell
PDI	Polydispersity Index
PVP_{29}	Polyvinylpyrrolidone (M_w = 29,000 g mol^{-1})
PVP_{40}	Polyvinylpyrrolidone (M_w = 40,000 g mol^{-1})
PVP_{55}	Polyvinylpyrrolidone (M_w = 55,000 g mol^{-1})
PXRD	X-ray powder Diffraction
SEM	Scanning Electron Microscopy
STEM	Scanning transmission electron microscopy
TEM	Trasmission Electron Microscopy
TGA	Thermogravimetric analysis
UV-Vis	Ultraviolet-Visible Spectroscopy

9.2 Palladium nanoparticles

9.2.1 Effect of the amount of potassium bromide

- **Differential centrifugal sedimentation**

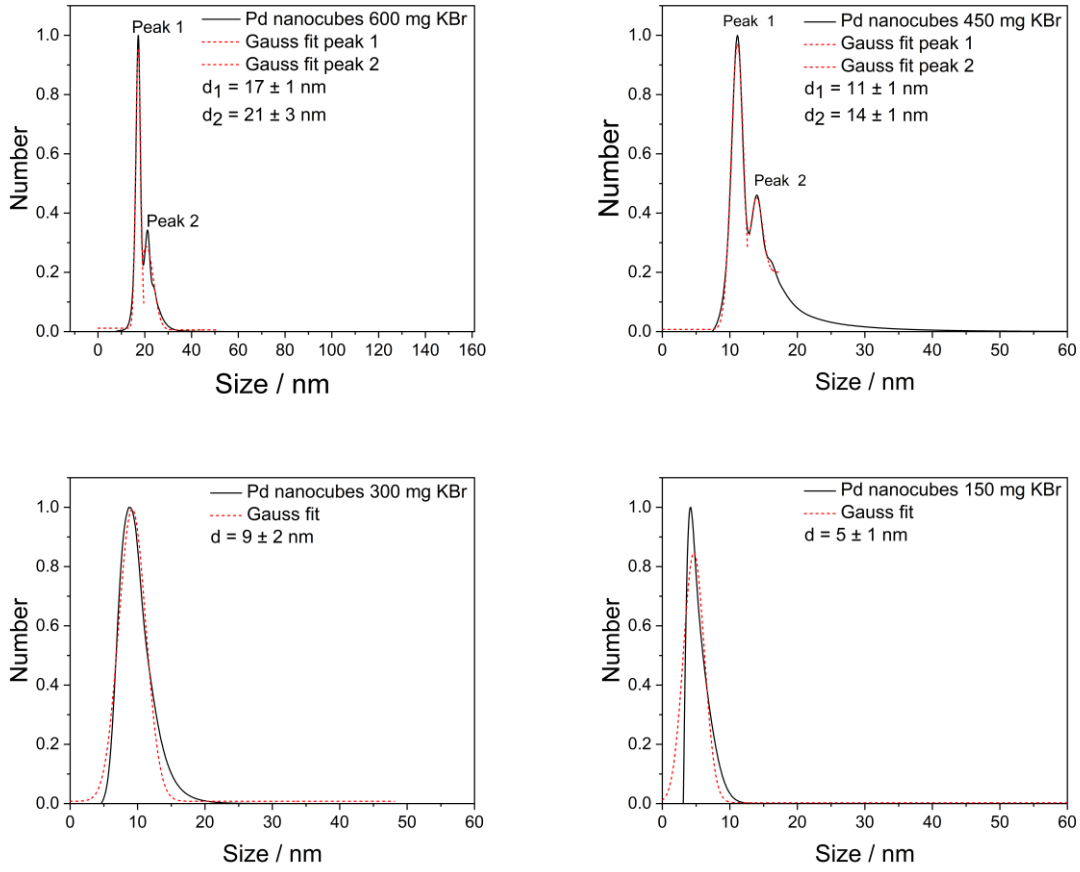

Figure 92. DCS measurements of palladium nanoparticles obtained from syntheses with different amounts of KBr.

- **Dynamic light scattering**

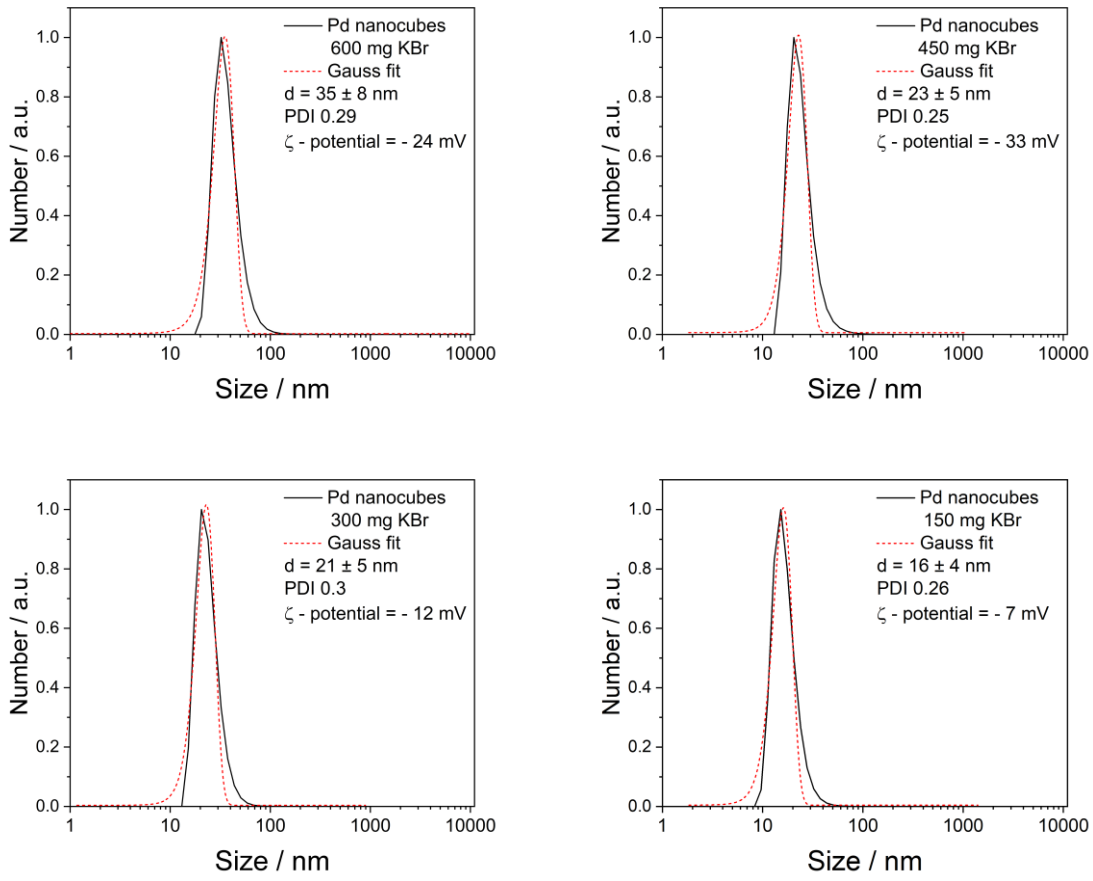

Figure 93. DLS and ζ-potential measurements of palladium nanoparticles obtained from syntheses with different amounts of KBr. Z-potential values decreased when adding a lower concentration of Br^-, indicating their influence on the stabilization of the nanoparticles.

9.2.2 Effect of the capping agent (DCS and DLS)

- **Differential centrifugal sedimentation**

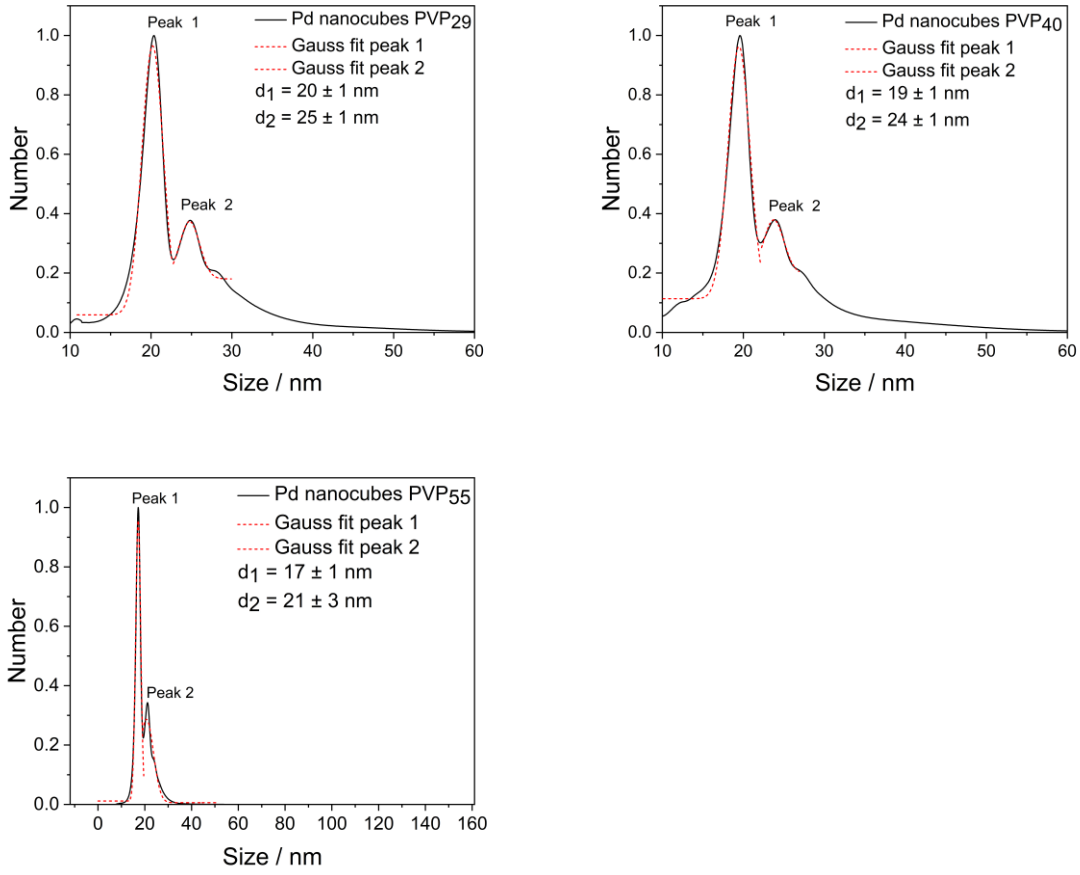

Figure 94. DCS particle size distributions obtained from palladium nanoparticle syntheses with different PVP lengths.

- **Dynamic light scattering**

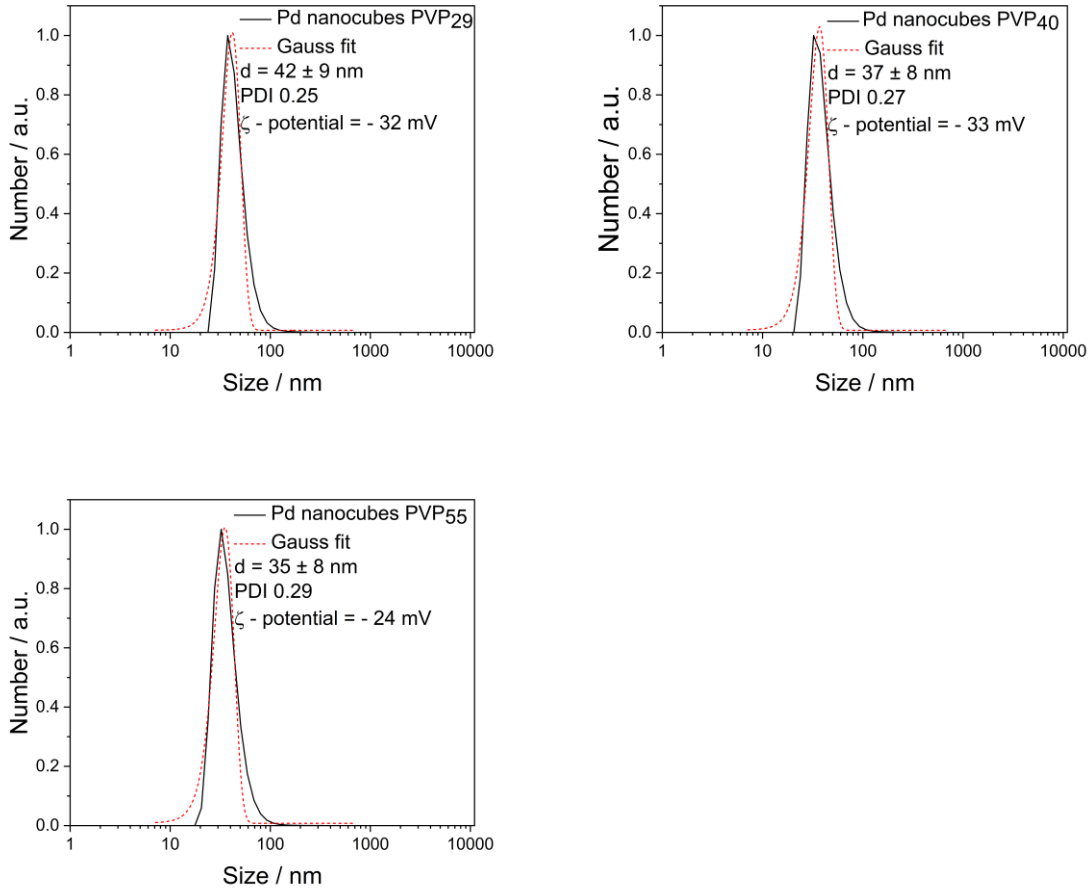

Figure 95. DLS particle size distributions (by number) show the average hydrodynamic diameter of the Pd nanoparticles obtained from syntheses with different PVP lengths.

9.2.3 Growth of Pd nanocubes

- **Differential centrifugal sedimentation**

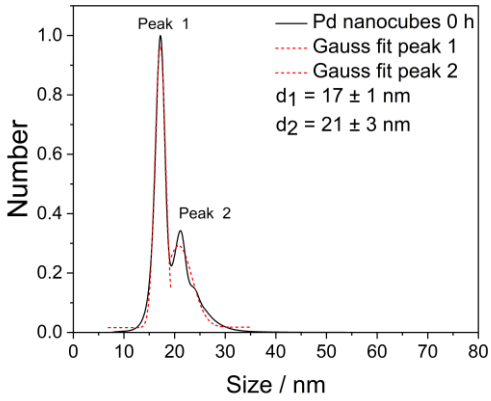

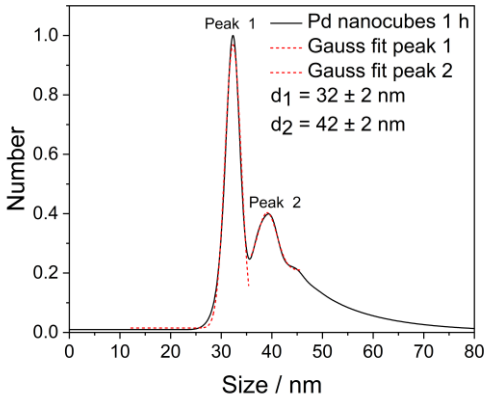

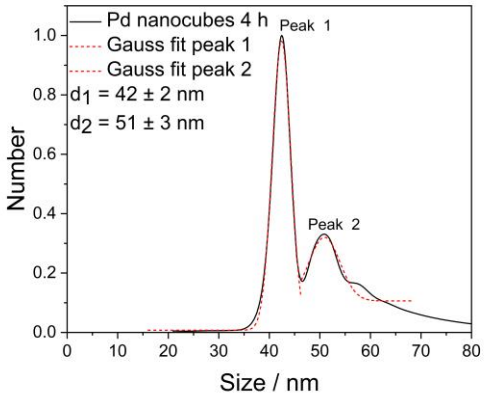

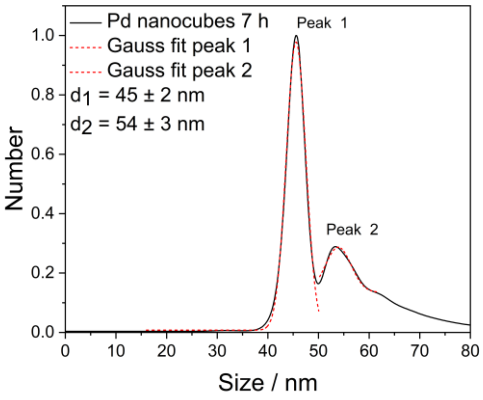

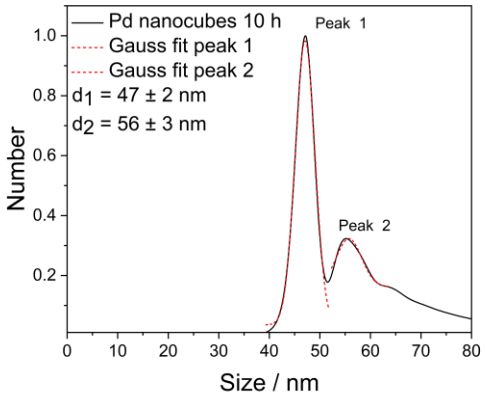

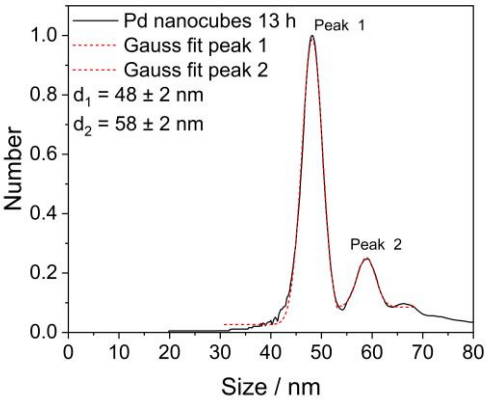

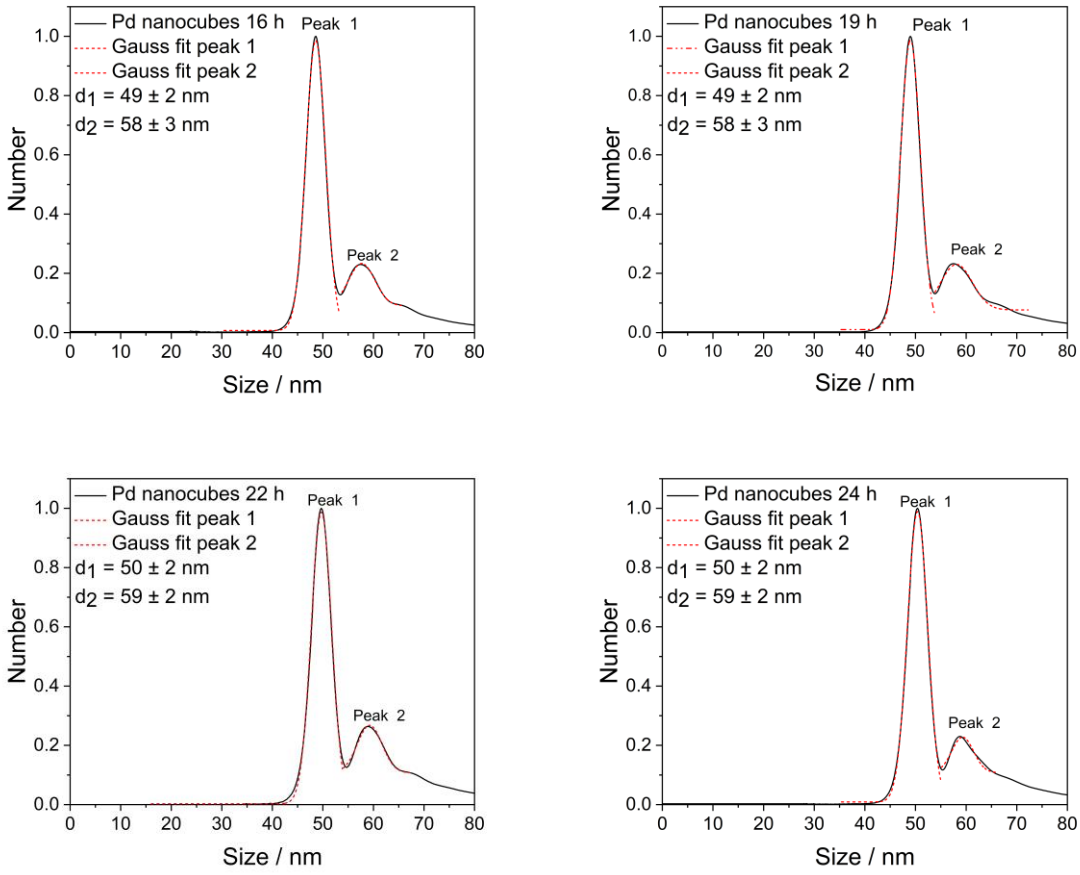

Figure 96. DCS particle size distributions obtained from the DCS measurements, which were carried out during the growth of the 45 nm nanoparticles.

9.3 *In-situ* electron microscopy videos

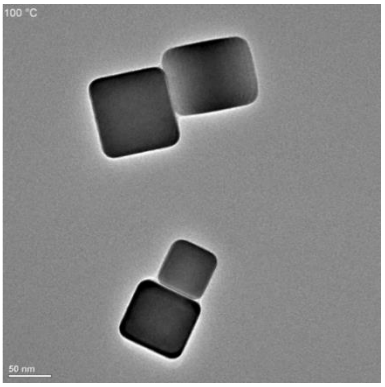

Video 1. QR code directing to the TEM *in-situ* heating experiment video of Ag nanocubes.

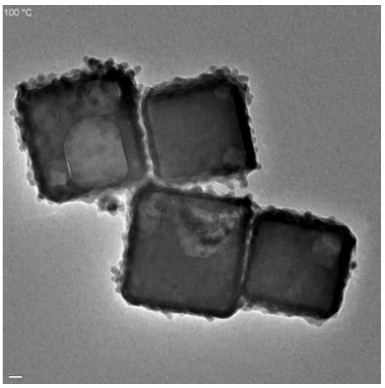

Video 2. QR code directing to the SEM *in-situ* heating experiment video of core-shell Ag@Au nanocubes.

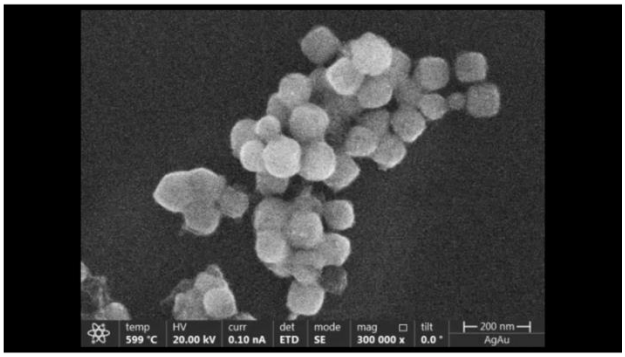

Figure 3. QR code directing to the SEM *in-situ* heating experiment video of core-shell Ag@Au nanocubes.

9.4 Publications

A. Karatzia, K. Loza, O. Prymak, M.Heggen and M. Epple, “Thermal Behavior of Silver-Gold Core-Shell: *In Situ X-ray Diffraction and in Situ Electron Microscopy (SEM and TEM)*, The Journal of Physical Chemistry C, **2023**. 127 (39): p. 19620-19628.

9.5 Posters and Presentations

16th International Conference on Materials Chemistry, RSC events, Dublin, Irland, 3-6.7.2023, A. Karatzia, K. Loza, O. Prymak, M. Heggen, M. Epple: "An *in-situ* investigation of the thermal behavior of silver nanocubes with and without a shell of gold." (**poster**)

3rd CENIDE Conference 2023, 2-5.5.23, Bergisch Gladbach, Germany, A. Karatzia, K. Loza, O. Prymak, M. Heggen, M. Epple: "Synthesis, characterization and *in-situ* heating studies of faceted bimetallic nanoparticles" (**poster**)

31st Annual Meeting of the German Crystallographic Society (DGK), 26-29.3.2023, Frankfurt, Germany, A. Karatzia, K. Loza, O. Prymak, M. Heggen, M. Epple: "Sublimation of silver and silver-gold core-shell nanocubes studied by *in-situ* powder diffraction and electron microscopy (SEM, TEM)" (**oral presentation**)

31st Annual Meeting of the German Crystallographic Society (DGK), 26-29.3.2023, Frankfurt, Germany, K. Loza, A. Karatzia, M. Heggen, M. Epple, "Thermal conversion of platinum-group metals by *in situ* transmission electron microscopy" (**poster**)

19th International Conference on Nanosciences and Nanotechnologies, Nanotexnology 2022, 5-8.7.2022, Thessaloniki, Greece, A. Karatzia, K. Loza, O. Prymak, M. Epple "Synthesis, characterization and *in-situ* studies of faceted noble metal bimetallic nanoparticles" (**oral presentation**)

30th Annual Meeting of the German Crystallographic Society (DGK), 14-17.3.2023, online. A. Karatzia, K. Loza, O. Prymak, M. Epple: "Synthesis and characterization of faceted bimetallic nanoparticles." (**oral presentation**)

9.6 Curriculum Vitae

9.7 Acknowledgments

I am expressing my sincere gratitude to Prof. Dr. Matthias Epple for trusting and providing me with the challenging and fascinating subject of my doctoral thesis. I am genuinely grateful for the opportunity to work under his supervision and guidance, which has been instrumental in shaping my research and academic development.

I am also thankful to Prof. Dr. Claudia Weidenthaler for assessing my thesis.

Special thanks go to Ms. Sabine Kiefer, Ms. Carola Fischer, and Ms. Sabine Bollmann, who played an indispensable role in assisting me with bureaucratic and organizational aspects during my time with the group. Their efficiency, professionalism, and, most importantly, their willingness to help made handling administrative issues much easier.

I extend my appreciation to Mr. Robin Meya and Ms. Beate Römer for their support in conducting hundreds of AAS measurements and to Ms. Ursula Giebel for the SEM images.

I am grateful to Dr. Oleg Prymak for introducing me to X-ray powder diffraction. His enthusiasm and availability to answer my questions and engage in discussions will never be forgotten.

A special word of thanks goes to Dr. Kateryna Loza for the countless hours we spent together in SEM and beyond. Her support, motivation, constructive feedback, and stimulating discussions have shaped my ideas and expanded my horizons both in scientific and private matters.

I would like to acknowledge my labor mate, Ms. Natalie Wolff, for all the moments, both good and bad, that we have shared throughout this journey. From the late evenings in the laboratory to scientific and private conversations, her great help and support have been invaluable.

I want to recognize Mr. David Mrosek, the ‘’third’’ member of our laboratory, for his support and the countless funny moments we shared.

I am grateful to Dr. Kateryna Loza, Ms. Natalie Wolff, and Dr. Konstantina Grigoriou for reading my Ph.D. thesis and providing fruitful feedback.

A big thank you to Mr. Rui Guo, Ms. Jana Storsberg, Dr. Kai Klein, Ms. Aileen Winter, Ms. Lisa Wagner, Dr. Sebastian Kollenda, Dr. Kathrin Kostka, Mr. Benedikt Kruse, Dr.Mateusz Olejnik, Mr. Oussama Tihouna, Ms. Ivanna Kostina, Mr. Jonas Sager, Ms. Nina Gumbiowski, Mr. Niklas Kost, Mr. Jan Schießleder, Mr. Sven Krämer and Dr. Nataniel Bialas for the good atmosphere and the enjoyable moments we shared at the university during lunch, coffee breaks, conferences, and beyond.

I would like to express my deep gratitude to my parents, who never stopped believing in me and made me the person I am today.

To my friends, thank you for your enduring support and encouragement.

Finally, a special dedication deserves my husband, my personal “positive energy source,” for his unwavering support, continuous motivation, understanding, and patience, especially over the last three years. I am truly grateful for all his love and his presence in my life.

9.8 Statutory Declaration / Eidesstaatliche Erklärung

I hereby declare that the presented thesis with the following title

“Mono- and bimetallic faceted noble metal nanoparticles: Synthesis and Characterization.”

is my own work and independently written. I further declare that I neither used the help of second individuals nor other tools and references as listed.

I also declare that the presented thesis has never been submitted in any other possible way to other faculties.

Hiermit versichere ich, die vorliegende Arbeit mit dem Titel

“Mono- and bimetallic faceted noble metal nanoparticles: Synthesis and Characterization”

selbst verfasst und unabhängig niedergeschrieben habe. Das Weiteren erkläre ich keine außer den angegebenen Hilfsmitteln und Quellen verwendet zu haben.

Zudem erkläre ich, dass ich die Arbeit in dieser oder einer ähnlichen Form bei keiner anderen Fakultät eingereicht habe.

Essen, den 31.08.2023

Aikaterini Karatzia